TACTILE TOMOGRAPHIC IMAGING USING ROBOTIC WHISKERS

BY

CAGDAS TUNA

DISSERTATION

Submitted in partial fulfillment of the requirements
for the degree of Doctor of Philosophy in Electrical and Computer Engineering
in the Graduate College of the
University of Illinois at Urbana-Champaign, 2014

Urbana, Illinois

Doctoral Committee:

Professor Douglas L. Jones, Chair,
Associate Professor Mitra Hartmann, Northwestern University
Professor Farzad Kamalabadi
Professor Emeritus William O'Brien

ABSTRACT

Animals such as rats and seals sense through movement by oscillating their whiskers back and forth to extract environmental information including nearby object features and fluid-flow characteristics. However, current array sensory systems do not fully utilize tactile sensing strategies extensively used by these animals. This dissertation focuses on developing advanced bio-inspired signal processing algorithms for the reconstruction of surroundings with arrays of vibrissal sensors. Inspired by the oscillatory motions of the rat's whiskers, we introduce a new tactile tomographic imaging model using robotic metal whiskers to extract object features including size, shape and location, and map out the cross-sectional fluid-flow characteristics via tomographic imaging.

Comparing the whisker position at the very initial object contact to a ray path in X-ray tomography, we show that the problem of object shape recognition with robotic whiskers can be expressed as a 2-D tactile tomographic imaging procedure by using only the whisker base position and the angle at the whisker base during the very initial contact recorded at different locations around the object.

At high Reynolds numbers, the drag force on a whisker segment is proportional to the relative velocity squared and hence, whether the flow is laminar or turbulent, we propose that it is possible to map out the 2-D cross-sectional mean fluid-flow velocity field using the moment measurements collected by

a robotic whisker array from different directions for tomographic reconstruction. We also present a linear state-space formulation for the tactile dynamic tomographic fluid-flow imaging for the sequential estimation of the fluid-flow characteristics in a dynamically changing environment.

The experimental results strongly demonstrate that this new tactile sensing technology developed in this dissertation may find a potential future use in various robotic applications including object feature extraction, object tracking, underwater navigation, high-resolution fluid-flow imaging, source localization and environmental mapping.

ACKNOWLEDGMENTS

I would like to express my gratitude to my advisor, Professor Douglas L. Jones, for his outstanding mentorship throughout my graduate studies, which has encouraged me to pursue an interdisciplinary academic career. I would like to thank my committee members, Professor Mitra Hartmann, Professor Farzad Kamalabadi and Professor William O'Brien for their guidance toward improving the quality of this dissertation. I also would like to acknowledge the National Science Foundation (NSF) for funding this work.

I am grateful for the time I spent at Prof. Mitra Hartmann's laboratory during the summer of 2011. I especially thank Dr. Joseph Solomon and Prof. Mitra Hartmann for sharing their expertise and knowledge, which has helped me gain extensive hands-on experience.

This dissertation has highly benefited from the insightful meetings with Prof. Farzad Kamalabadi and technical discussions with my lab mates, Dr. Dave Jun and Erik Johnson. I deeply appreciate their helpful comments and suggestions. I am also thankful to all of my colleagues in Prof. Douglas L. Jones' lab for their close friendship over the years.

Last but not the least, I would like to thank my father, Ismail, my mother, Nezahat, and my brother, Ulas for their endless support throughout my life.

TABLE OF CONTENTS

CHAPTER 1

Introduction

Many mammals with whiskers use tactile sensing as a main sensory mechanism to navigate and explore their surroundings. Rats can extract object features and discriminate texture through the oscillatory motion of their whiskers [1, 2]. Seals use their whiskers to keep track of hydrodynamic trails generated by fish [3]. Shrews can detect and target their prey in the dark with their whiskers [4]. Tactile perception is the principal sensory system particularly for animals living underground or in muddy, dark environments, where eyesight fails; in other cases, it may also serve as a supplementary information source to other sensory systems such as visual sensing [5].

Inspired by the tactile sensing capability of the whisking animals, our goal is to develop advanced signal-processing methods to extract detailed information about surroundings using robotic whisker arrays. In recent years, biomimetic artificial whisker systems have become an emerging research field for applications including distance estimation, shape recognition, texture discrimination, navigation, simultaneous localization and environmental mapping, as a result of the expanding neurobiological knowledge about vibrissal sensing of animals [6–21]. However, to our knowledge, the work on the reconstruction of surroundings with vibrissal sensor arrays is still very limited.

This dissertation focuses on developing a novel tactile imaging technology with robotic whiskers, which relates whisker movements to tomographic

reconstruction for the exploration of surroundings. Tomographic imaging is the reconstruction of an unknown physical field via the set of line-integrated observations collected by multiple sensors from different directions. Rats do not have any receptors along the length of their whiskers; and as a result, the mechanical transduction of all the tactile information collected through whisking occurs back at the pressure-sensitive receptors at the whisker base [5, 22]. Therefore, inspired by rat's whisker sensory system, our goal is to recover environmental information including object features and fluid-flow characteristics through the tactile information collected by artificial metal whiskers with strain gauges installed at the whisker base from different directions for tomographic imaging.

The first tactile tomographic imaging application addressed in this dissertation is the recovery of a shape of an object. Based on the analogy that each whisker can be regarded as a "whisker path" similar to a "ray path" in X-ray tomography, we demonstrate that the problem of object shape recognition with artificial whiskers can be formulated as a 2-D tactile imaging process, using only the angular position at the whisker base during the initial contact with the object recorded at multiple views for tomographic reconstruction [23].

Another application studied in this dissertation is the 2-D cross-sectional tactile mean fluid-flow tomographic imaging with a robotic whisker array. At high Reynolds number, the drag force on a whisker segment is proportional to relative velocity squared, whether the flow is laminar or turbulent, and acts as a distributed load along the whisker length, which is sensed at the whisker base as the line-integrated moment information [24, 25]. Therefore, we propose that incorporating tomography into tactile flow sensing can make it possible to map out the 2-D cross-sectional mean fluid-flow velocity field

with robotic whiskers by measuring the moment sensed at each whisker base from different directions, enabling a fundamentally new sensor technology for flow-field measurements.

In the case of a dynamically changing flow pattern, the 2-D static cross-sectional fluid-flow reconstructions may contain severe image artifacts, due to significant temporal variations in the physical field. However, this problem can be solved by using a dynamic tomographic approach, in which the unknown physical field may be modeled as a discrete-time hidden Markov random process, and hence it can be recursively estimated given the measurements [26, 27]. When the dynamic tomography problem can be formulated under the linear state-space model, solutions exist such as the Kalman filter [28, 29]. There are several dynamic tomography applications using the linear state-space model [30–36]. In this dissertation, the Kalman filter is used to recursively compute the linear minimum mean squared error (LMMSE) estimates for dynamic tactile fluid-flow tomographic imaging. The air and underwater flow experiments indicate that the dynamic tactile fluid-flow tomographic approach may find a potential use in many robotic applications including object tracking, navigation and obstacle avoidance.

The remainder of the dissertation is organized as follows. Chapter 2 focuses on the implementation of the whisker tomography approach for object shape recognition. We first describe that the whisker position at the very initial contact can be regarded as a ray path in X-ray tomography, and then demonstrate the tomographic reconstruction of the 2-D cross-sectional image of objects through simulations and experiments. We also present a sparse representations solution to object shape recognition using a reduced number of whisks, which can be viewed as a type of limited-data tomography problem.

Chapter 3 explains the fluid mechanics fundamentals for sensing with whiskers, and introduces the forward model for tactile fluid-flow tomography. The chapter concludes with the detailed description of the image reconstruction methods for the static and dynamic flow tomography.

Chapter 4 describes the experimental setup used for in-air and underwater experiments including the detailed information about the building and calibration process for the robotic whisker array, and presents the air and underwater flow imaging results that evaluate the performance of the static fluid-flow tomography model.

Chapter 5 demonstrates the dynamic tactile air and underwater flow tomographic imaging results under the linear state-space model for the different cases including the detection of time-varying flow patterns and moving flow sources, and the tracking of moving objects before the actual touch. Conclusions and future research directions are presented in Chapter 6.

CHAPTER 2

Tomography with Robotic Whiskers for Object Shape Recognition

Vibrissal-sensing animals such as rats, seals and shrews use their whiskers for the exploration of their surroundings. Bio-inspired by the tactile sensing strategies applied by the whisking animals, there are several recent studies for object shape recognition using robotic whiskers. The class of techniques based on rotating or translating the whisker against an object through small angles uses this tactile information to estimate the contact point location along the length of the whisker. Tsujimura and Yabuta [6] developed a six-axis force/torque sensor to determine the contact point location using an insensitive probe. Kaneko, Kanayama and Tsuji [7] built a flexible whisker to estimate the object contact point positions through the rotational compliance. Ueno, Svinin and Kaneko [8] determined the contact points using a whisker with a torque sensor to measure the oscillation frequency at the whisker base. Kim and Möller [9] installed two arrays of flexible whiskers on a rotating plate using magnetic and microphone-based sensors for object shape recognition. Clements and Rahn [10] developed a flexible whisker with a two-axis actuator and six-axis force/torque sensor based on a large-angle elastica model to estimate the contact point location. Solomon and Hartmann [15, 17] designed a whisker array model for the tactile extraction of the 3-D object shape in the presence of lateral slip and surface friction.

More advanced models exist to further extract multiple contact points beyond the initial contact as a single whisker moves along the object surface. Russel and Wijaya [13] designed a robot with an array of eight whiskers to recognize objects through surface classification by sweeping the tip of the whiskers. Scholz and Rahn [14] developed a large-angle elastic model using a six-axis force/torque load cell to rotate a flexible whisker to estimate the profile shape of objects by computing the shape of a single bending whisker during the contact with the object. Solomon and Hartmann [16] also developed a sweeping algorithm to extract the object profile shape accurately with a single whisker by estimating the contact points continuously beyond the initial contact.

In this chapter, we demonstrate our tomographic approach for 2-D object shape recognition with robotic whiskers initially presented in [23] with the preliminary results. Tomography is a widely used imaging technique in various fields from medical imaging to seismology, where the goal is to recover a multidimensional structure from its lower-dimensional measurements, called "projections", collected from different directions. Observing that the whisker position at the very initial contact is similar to a ray path in X-ray computed tomography, we show that the 2-D cross-sectional object profile can be extracted with tomographic reconstruction based on only the information about the angle at the whisker base and the whisker-base location at the very initial contact collected from various angular views. The proposed approach differs from the existing techniques as it does not require the computation of the radial distance from the whisker base to the contact point along the length of the whisker. This brings the important practical advantage of eliminating the need for the calibration of the voltage signal at the whisker base with the bending

moment. We show that it is possible to recover the shape of a convex object by computing its corresponding 2-D Radon transform based on the straight whisker paths at the very initial contact, and then applying tomographic reconstruction over the entire measurement set, rather than computing a single estimate for the contact point location at each whisk.

The chapter begins with the brief explanation of the X-ray transform and the 2-D discrete inverse Radon transform in Section 2.1. Next, we formulate object shape recognition with robotic whiskers as a tomographic reconstruction problem based on two slightly different projection assignment procedures, and introduce the tomographic reconstruction methods for shape recovery along with a sparse representations solution to the limited-angle tomography problem occurring from performing a reduced number of whisks in Section 2.2. Then, we present the experimental results that validate the tactile tomographic approach to the object shape recognition problem in Section 2.3. We conclude the chapter with a discussion about implications, limitations and possible future directions regarding the proposed tactile shape recognition model in Section 2.4.

2.1 The X-Ray Transform

The n-dimensional X-ray transform maps a function $x \in \mathscr{S}(\mathbb{R}^n)$ into its set of integrals, where $\mathscr{S}(\mathbb{R}^n)$ is the Schwartz space, the function space of functions that have rapidly decreasing derivatives of all orders. Then, the X-ray transform $\mathbf{H}x(\mathbf{t}, \boldsymbol{\theta}_i)$ [37, 38]

$$\mathbf{H}x(\mathbf{t}, \boldsymbol{\theta}_i) = \int_{-\infty}^{\infty} x(\mathbf{t} + r\boldsymbol{\theta}_i)dr \tag{2.1}$$

is the integral of x over the straight line in the direction of the unit vector $\boldsymbol{\theta}_i \in \mathsf{S}^{n-1}$, where the set $\mathsf{S}^{n-1} = \{d \in \mathbb{R}^n : ||d||_2 = 1\}$ is the unit sphere in $\mathbb{R}^n$, $d \in \mathbb{R}$, and the vector $\mathbf{t} \in \Theta^{\perp}$, the vector space orthogonal to $\boldsymbol{\theta}_i$. The X-ray transform is closely related to the Radon transform, which is defined by integrating over hyperplanes rather than lines as in the X-ray transform, but the two transforms coincide in two dimensions.

In the 2-D case, $\boldsymbol{\theta}_i \in \mathsf{S}^1$ can be defined as a unit vector in $\mathbb{R}^2$ with polar angle $\phi_i \in [0, 2\pi]$ and $\boldsymbol{\theta}_i^{\perp}$ as the unit vector $\pi/2$ units clockwise from $\boldsymbol{\theta}_i$ [38]:

$$\boldsymbol{\theta}_i = (-\sin\phi_i, \cos\phi_i) \qquad \boldsymbol{\theta}_i^{\perp} = (\cos\phi_i, \sin\phi_i). \tag{2.2}$$

Then, the 2-D Radon transform can be rewritten in terms of (t, ϕ_i) as [38, 39]

$$\begin{aligned} \mathbf{H}x(t, \phi_i) &= \int_{-\infty}^{\infty} x(t\boldsymbol{\theta}_i^{\perp} + r\boldsymbol{\theta}_i)dr & (2.3) \\ &= \int_{-\infty}^{\infty} x(t\cos\phi_i - r\sin\phi_i, t\sin\phi_i + r\cos\phi_i)dr, & (2.4) \end{aligned}$$

which is also known as the parallel-beam projection tomography [39, 40], since a straight line moves in the direction of $\boldsymbol{\theta}_i$ with signed distance t from the origin, resulting in a collection of parallel lines. Each line represents a "ray path" through which the X-rays travel at the ith angular view.

The projection-slice theorem states that the Fourier transform of the projection of x at an angle ϕ is a slice in the 2-D Fourier transform of x taken at the same angle:

$$H(f, \phi) = X(f\cos\phi, f\sin\phi), \tag{2.5}$$

where H is the 1-D Fourier transform of the 2-D Radon transform $\mathbf{H}x(t, \phi)$ at

the viewing angle ϕ, and X denotes the 2-D Fourier transform of x.

Using the projection-slice theorem, the inverse 2-D Radon transform is given by

$$x = \int_0^{\pi} \int_{-\infty}^{\infty} H(f,\phi) e^{j2\pi ft} |f| df d\phi = \int_0^{\pi} \hat{x}(t,\phi) d\phi, \tag{2.6}$$

where $\hat{x}(t,\phi)$ denotes the projection passed through the "ramp filter" whose frequency response is $|f|$. Each filtered projection $\hat{x}(t,\phi)$ is then uniformly added to x along the straight line on which the actual projection is measured. This procedure can be regarded as "backprojecting" each $\hat{x}(t,\phi)$ along the corresponding ray path, and hence is known as the "filtered-backprojection" (FBP) algorithm [38, 40].

The 2-D discrete Radon transform can be derived from its continuous formulation by representing the unknown spatial field x with a finite basis expansion and using the discrete nature of the measured data usually collected by sensor arrays in practice. Since the 2-D Radon transform is linear, using a rectangular pixel array to discretize the unknown image field, the discrete version can be expressed in the matrix equation form as

$$\boldsymbol{y}_i = \boldsymbol{H}_i \boldsymbol{x}, \tag{2.7}$$

where $\boldsymbol{x}$ is the vector representation of the unknown image of length N, $\boldsymbol{y}_i$ is the projection vector of length M, and $\boldsymbol{H}_i \in \mathbb{R}^{M \times N}$ is the linear operator that relates the unknown spatial field to the projections at the viewing angle ϕ_i. The matrix element $\boldsymbol{H}_i^{mn}$ represents the contribution of the nth pixel to the line integral $\boldsymbol{y}_i^m$ measured along the mth ray path.

Let L be the total number of angular views. Then, the entire set of projections can be written in the matrix equation form as

$$\boldsymbol{y} = \boldsymbol{H}\boldsymbol{x}, \tag{2.8}$$

where $\boldsymbol{y} = [\boldsymbol{y}_1^T, \boldsymbol{y}_2^T, \cdots, \boldsymbol{y}_L^T]^T$ is the concatenated projection vector of length $M \cdot L$, and the linear operator $\boldsymbol{H} = [\boldsymbol{H}_1^T, \boldsymbol{H}_2^T, \cdots, \boldsymbol{H}_L^T]^T \in \mathbb{R}^{M \cdot L \times N}$.

The discrete FBP solution is then given by

$$\hat{\boldsymbol{x}}_{FBP} = \boldsymbol{H}^T \boldsymbol{R} \boldsymbol{y}, \tag{2.9}$$

where $\boldsymbol{R} \in \mathbb{R}^{M \cdot L \times M \cdot L}$ denotes the filtering matrix to obtain the filtered projections and the transposed linear operator $\boldsymbol{H}^T$ corresponds to the "backprojection" of the the filtered projections in order to compute the FBP estimate $\hat{\boldsymbol{x}}_{FBP}$. If no ramp filtering is applied to the projections, then it is called the "simple backprojection" solution given by

$$\hat{\boldsymbol{x}}_{BP} = \boldsymbol{H}^T \boldsymbol{y}. \tag{2.10}$$

2.2 Tactile Tomographic Shape Recognition

We consider the 2-D imaging of fixed, rigid convex objects using an artificial whisker that is made of a thin, flexible, straight, cylindrical beam. The whisker bends only within its plane of rotation and makes contact with the convex object at a discrete point along its length, not at its tip. The whisker rotates against the object through small angles from different directions around the object for tomographic reconstruction.

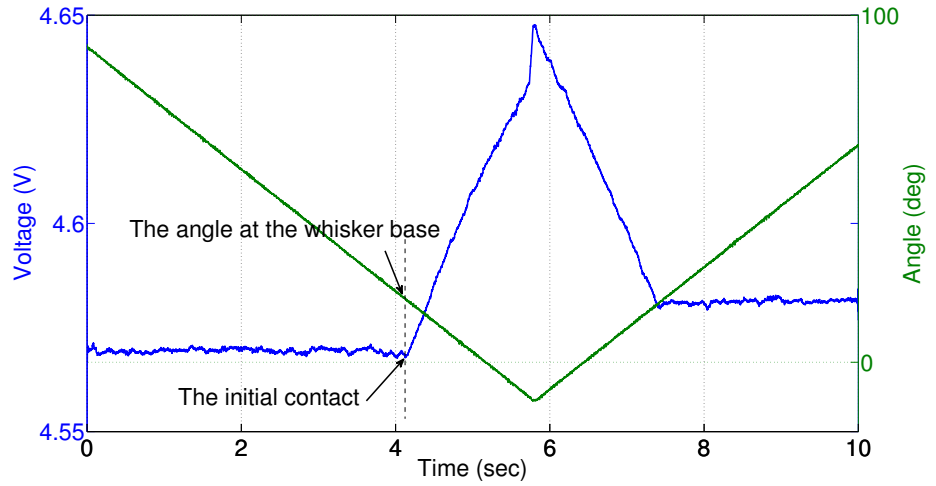

Figure 2.1: The measured voltage and the angle at the whisker base during the contact with a convex object.

The tactile tomographic shape recognition process begins with recording the whisker base angle and location at the very initial contact, right before the output voltage level starts to increase as illustrated in Figure 2.1 with the experimental data measured during the contact with a convex object.

Figure 2.2 shows the whisker position and the angle at the whisker base γ at the initial contact with a convex object for the angular view ϕ. The angle β represents the amount of whisker rotation since the initial position of the whisker at the first angular view, taking values between 0° and 360°. The projection angle ϕ at the initial contact is obtained by using geometry followed by a modulo operation to shrink the projection angles into the range between 0° and 180° for tomographic reconstruction. The projection angle ϕ and the signed distance t_c of the corresponding "whisker path" is then given by

$$\phi = \mod(\gamma + \beta + 90^\circ, 180^\circ) \tag{2.11}$$

$$t_c = x_{wb}\cos\phi + y_{wb}\sin\phi, \tag{2.12}$$

where "mod" denotes the modulo operation.

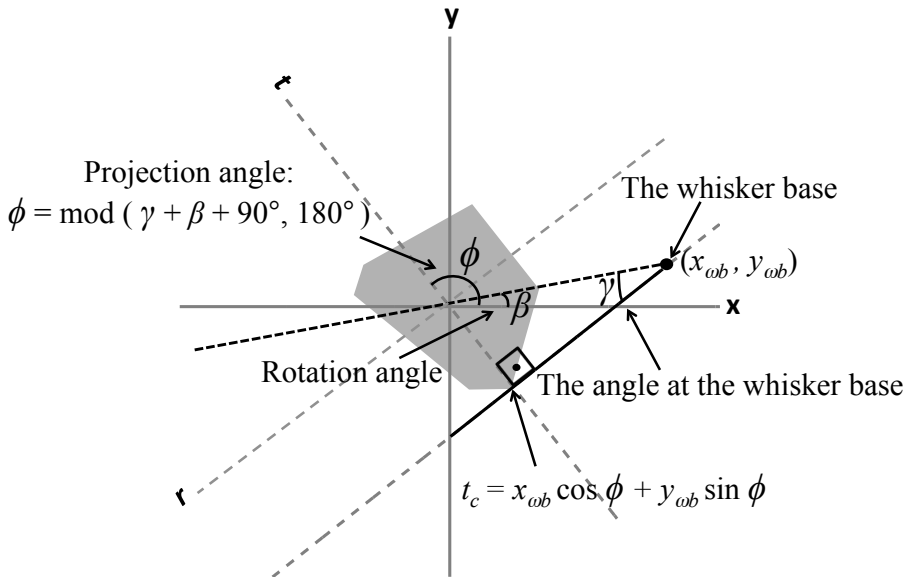

Figure 2.2: The whisker position at the initial contact with a convex object at the viewing angle ϕ: The angle at the whisker base, γ, and the whisker rotation angle, β, are recorded to obtain the projection angle, ϕ.

In X-ray tomography, X-rays pass through the interior of the object along straight lines, or "ray paths", from different directions, and the projections at a particular angular view are the set of line integrals taken over these ray paths. However, in our case, the whisker bends as the whisker continues to sweep against the object after the initial contact. As a result, contrary to X-ray tomography, there are no such "whisker paths" passing through the interior of the object. In the absence of any line-integrated information, the 2-D Radon transform is instead computed by translating the angular information at each whisk into a projection vector using pre-defined 1-D filtering functions that take values according to the straight whisker paths at the very initial contact. This also implies that the calibration with the bending moment sensed at the whisker base becomes unnecessary, since observing a rise in the voltage signal

would be sufficient to determine the initial contact angle at the whisker base.

Assuming no tip contact, the whisker comes into initial contact with a convex polygonal-shaped object at one of its corners, whereas the initial contact occurs at a different location along the object boundary for a curved-shaped object at each whisk. Therefore, our goal is to extract the 2-D convex hull of an object through its corners and/or contact points along its curved surfaces by using the angular information at the initial contact recorded from various directions around the object for tomographic reconstruction.

2.2.1 Projection Assignment Using a Gaussian Function

Using the fact that a single point of contact occurs with the convex object somewhere along the length of whisker, the first projection assignment approach involves using a 1-D Gaussian filter whose impulse response is a Gaussian function centered at the signed distance t_c corresponding to the whisker path at the very initial contact with its peak normalized to 1:

$$f(t) = e^{-(t-t_c)^2/2\sigma^2}, \tag{2.13}$$

where σ is the standard deviation of the filter. This projection assignment procedure may also be viewed as generating the point spread function of the imaging system, that is being the impulse response to a point source.

Under the convexity assumption, there are only two possible parallel whisker paths at a given angular view, since the convex-shaped object must lie between these two parallel lines. Therefore, the projection vector at a viewing angle ϕ using a Gaussian function can be written as the discrete samples of the

summation of two Gaussian functions

$$\begin{aligned} p(t,\phi) &= f(t_1,\phi) + f(t_2,\phi) \\ &= e^{-(t-t_1)^2/2\sigma^2} + e^{-(t-t_2)^2/2\sigma^2}, \end{aligned} \tag{2.14}$$

where t_1 and t_2 represent the signed distances of the corresponding whisker paths at the very initial contact, which can also be described as a mixture of two 1-D Gaussian functions. This formulation requires the value of σ to be small enough to distinguish between the two parallel whisker paths. The Gaussian projection assignment procedure is illustrated in Figure 2.3 for a hexagonal-shaped object at a given angular view with the choice of $\sigma = 0.05$.

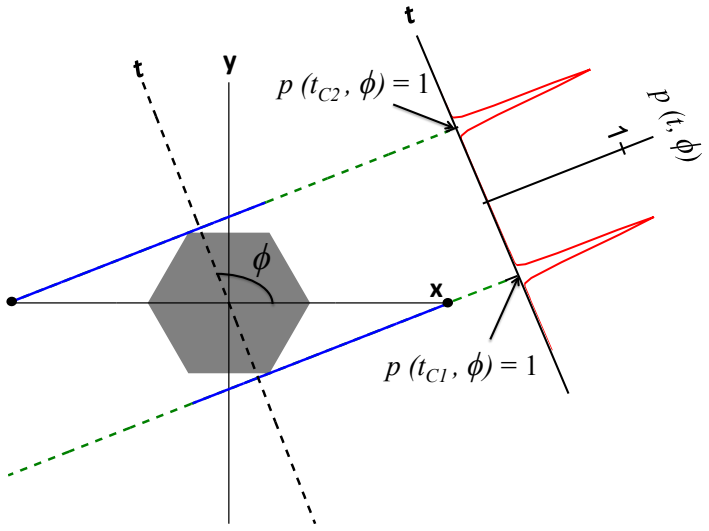

Figure 2.3: Projection assignment at a particular viewing angle ϕ using the Gaussian function with $\sigma = 0.05$: Projections are assigned with respect to the two parallel whisker paths at the very initial contact.

Figure 2.4 represents the 2-D physical positions of the convex objects with circular, hexagonal and square-shaped cross-sections tested for tactile tomographic shape recognition with a robotic whisker.

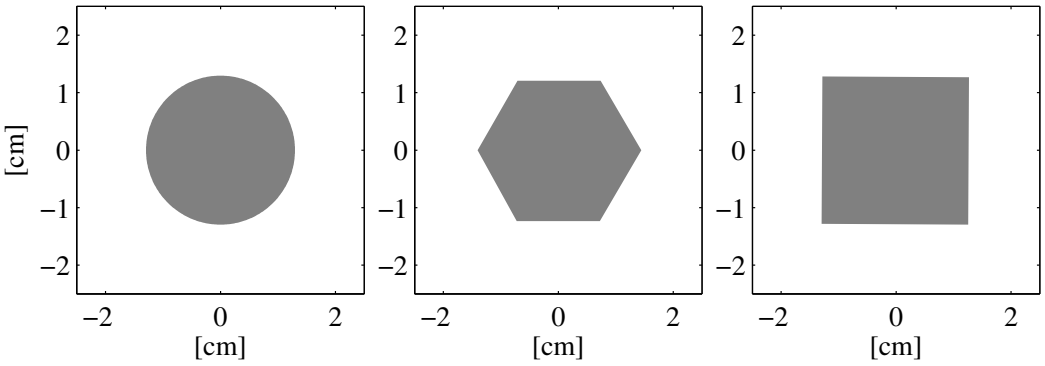

Figure 2.4: The 2-D physical positions of the convex objects including circle, hexagon and square tested for tactile tomographic shape recognition.

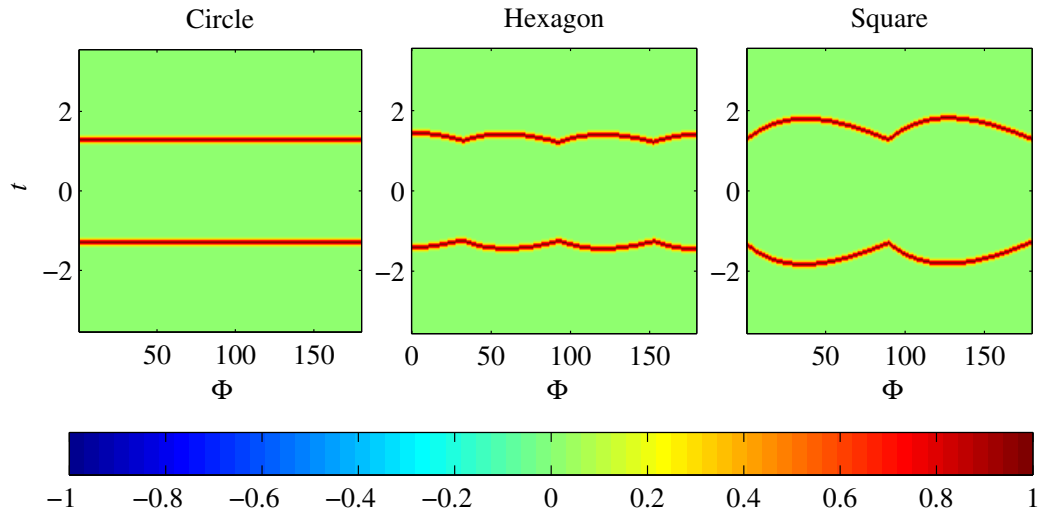

Figure 2.5: The 2-D Radon transform of the circular, hexagonal and square-shaped objects shown in Figure 2.4 using the Gaussian-function projection assignments with $\sigma = 0.05$.

Figure 2.5 shows the simulated 2-D Radon transform of the circular, hexagonal and square-shaped objects shown in Figure 2.4 using the Gaussian-function projection assignment with $\sigma = 0.05$. The number of uniformly spaced parallel whisker paths at an angular view was chosen to be $M = 183$ and a total of 360 whisks were simulated at evenly spaced (1°) intervals around the objects corresponding to 180 different angular views. Hence, each 2-D Radon trans-

form was obtained by assigning the projection vector $\boldsymbol{y}_i$ at the ith angular view into the ith column of the projection matrix of size 183×180, resulting in the concatenated projection vector $\boldsymbol{y}$ of length $183 \times 180 = 32940$.

The measurement matrix $\boldsymbol{H}_{32940\times16384}$ was generated for the image reconstruction at a spatial resolution of 128×128 pixels ($N = 128^2 = 16384$). A ramp filter combined with the third-order Butterworth low-pass filter with the normalized cut-off frequency $f_c = 0.1$ was used for FBP image reconstruction as shown in Figure 2.6 to reduce the effects of background noise resulted from very high frequency components amplified by ramp-filtering.

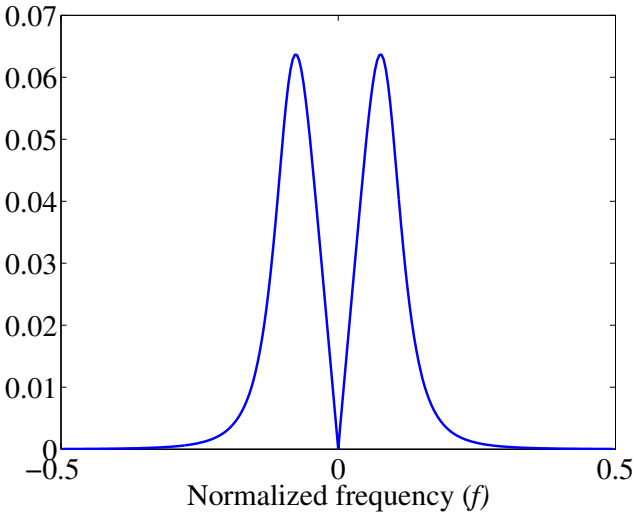

Figure 2.6: The frequency response of the filter used for FBP image reconstruction: The ramp filter is accompanied by a third-order Butterworth filter with the normalized cut-off frequency $f_c = 0.1$.

Figure 2.7 shows the resulting Gaussian-function backprojection (GF-BP) and the Gaussian-function filtered-backprojection (GF-FBP) images. The maximum pixel value of the resulting images are normalized to the value of 1 so as to make a better comparison between the two reconstruction methods.

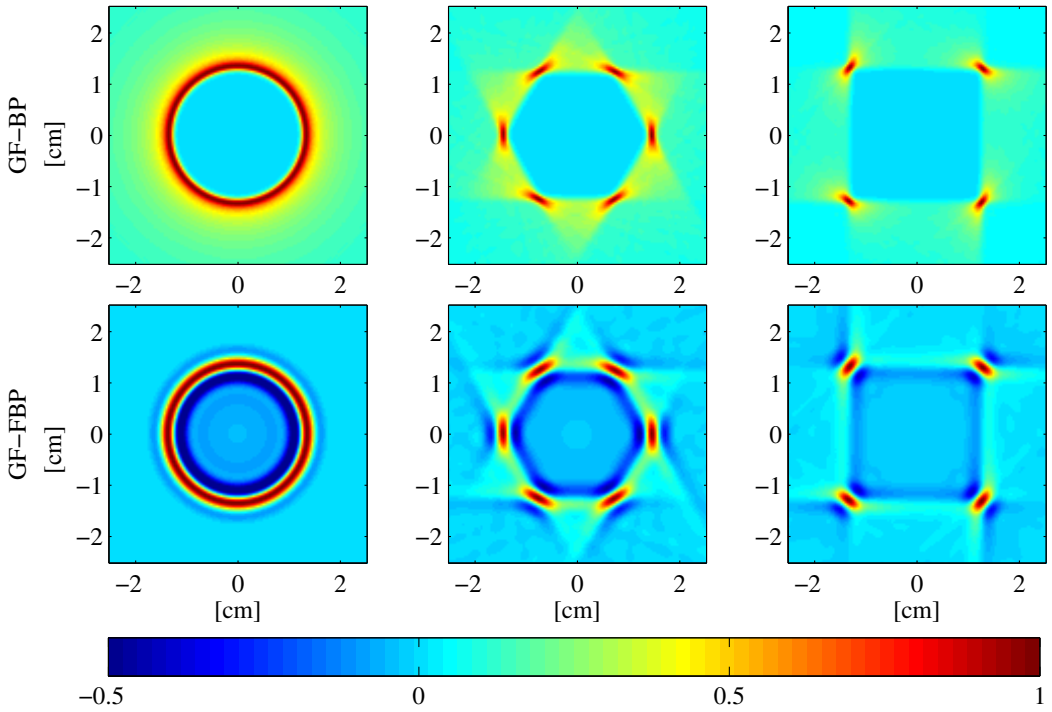

Figure 2.7: The reconstructed 128×128 images using the 2-D Radon transform in Figure 2.5: Top row: the Gaussian-function backprojection (GF-BP), bottom row: the Gaussian-function filtered-backprojection (GF-FBP).

The resulting images demonstrate that using a Gaussian filter as a point spread function, the corner points can be reliably extracted for hexagon and square, since the contact always occurs at one of the vertices at any whisk. On the other hand, the object contours for the circular-shaped object can be recovered almost completely through the contacts at distinct locations along the circular boundary. It is also clearly seen that the pixels corresponding to the convex interior region of the objects take smaller values than the outer free whisking region. In general, applying simple backprojection directly for tomographic reconstruction results in blurred images. However, using a narrow-width Gaussian function with $\sigma = 0.05$ alleviates such smearing effects caused by simple backprojection for GF-BP. As expected, filtering the projections results in enhanced boundary information for GF-FBP.

2.2.2 Projection Assignment Using the Error Function

At any viewing angle, a convex object lies between two parallel lines, which serve as the transition or boundary layers that separate the free-whisking region from where the whisker has to bend as it moves along the object. In order to compensate for the missing information about the interior region of the convex object by filling the gap between the two parallel whisker paths at a particular angular view, we alternatively propose a second projection assignment method using a sigmoid function such as the error function $\mathrm{erf}(t) = \frac{2}{\pi}\int_0^t e^{-x^2}\mathrm{d}x$:

$$g(t) = \mathrm{erf}\left(\frac{t - t_c}{\sqrt{2\sigma^2}}\right). \tag{2.15}$$

Given the signed distances t_1 and t_2 corresponding to the two parallel whisker paths at a particular view, the projection vector at a viewing angle ϕ via the error function approach is defined as the discrete samples of the function

$$\begin{aligned} p(t,\phi) &= g(t_1,\phi)g(-t_2,\phi) \\ &= \mathrm{erf}\left(\frac{t - t_1}{\sqrt{2\sigma^2}}\right)\mathrm{erf}\left(-\frac{t - t_2}{\sqrt{2\sigma^2}}\right), \end{aligned} \tag{2.16}$$

where the projection values for the second parallel whisker path are assigned using the fact that the error function is odd: $-\mathrm{erf}(x) = \mathrm{erf}(-x)$. This means that $p(t,\phi)$ is the product of the two functions corresponding to the two parallel lines, intersecting the outcomes of the two initial-contact straight whisker paths at the same angular view.

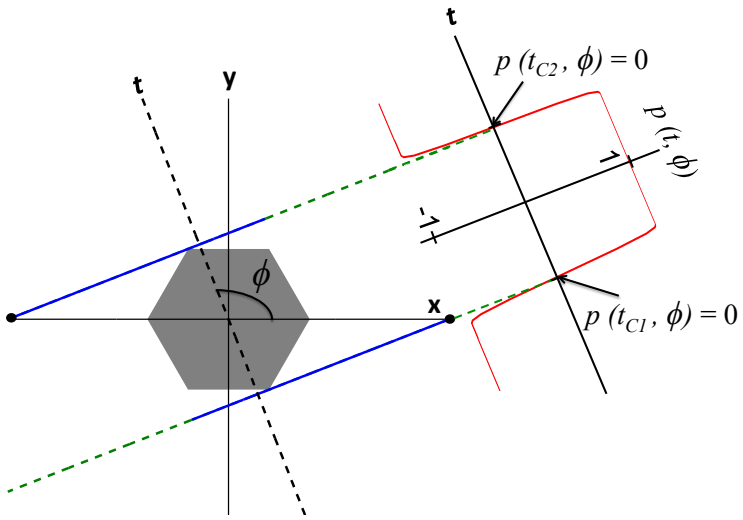

Figure 2.8: Projection assignment at a particular viewing angle ϕ using the error function with $\sigma = 0.05$. Projections are assigned with respect to the object boundaries that are in line with the two parallel whisker paths at the very initial contact.

Figure 2.8 describes the second projection assignment procedure using the error function with the choice of the standard deviation $\sigma = 0.05$. Rather than some form of a rectangular function, a differentiable function that has a smoother transition may be more preferable to prevent errors due to filtering or interpolation with the standard deviation σ determining the width of the transition region.

Figure 2.9 shows the simulated 2-D Radon transform of the circular, hexagonal and square-shaped objects shown in Figure 2.4 using the error-function projection assignment with $\sigma = 0.05$ with $M = 183$ and a total of 360 whisks.

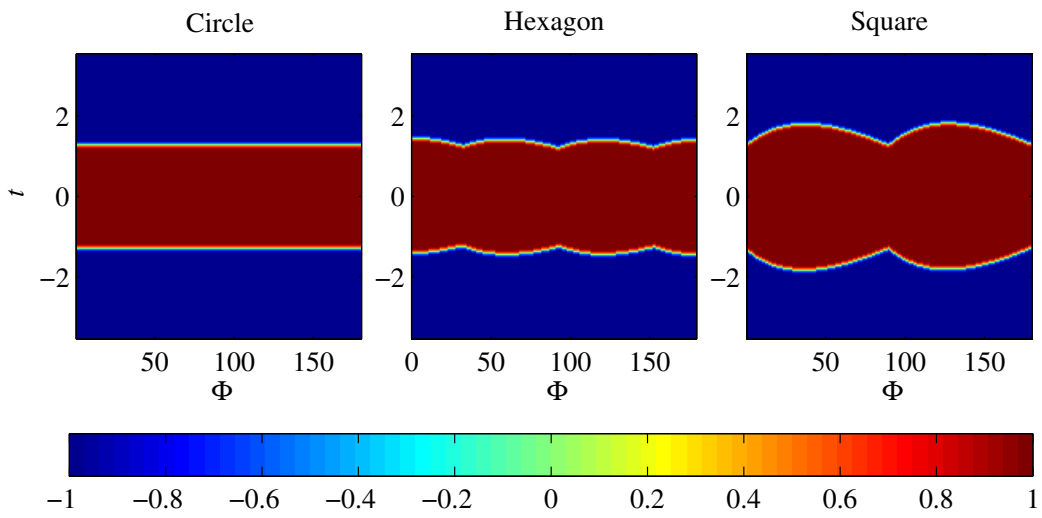

Figure 2.9: The Radon transform of the circular-, hexagonal- and square-shaped objects shown in Figure 2.4 using the error-function projection assignments with $\sigma = 0.05$.

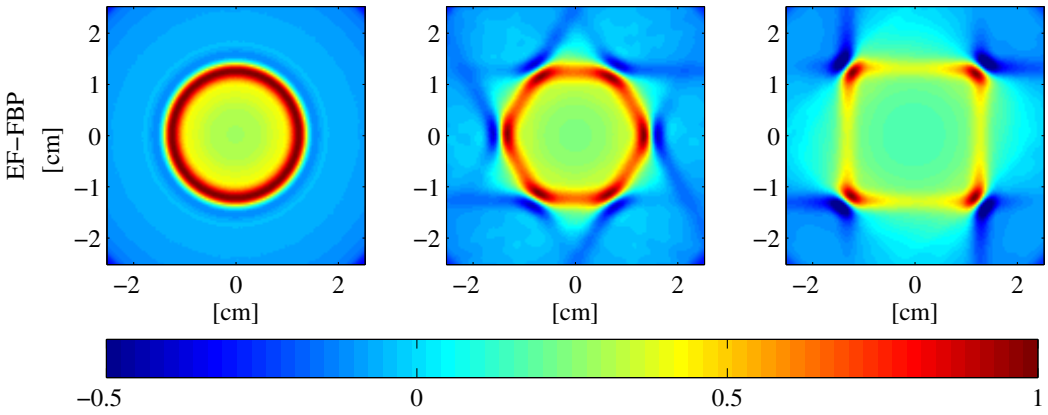

Figure 2.10: The reconstructed 128×128 error-function filtered-backprojection (EF-FBP) images using the 2-D Radon transform in Figure 2.9.

Figure 2.10 shows the resulting error-function filtered-backprojection (EF-FBP) images using the filter shown in Figure 2.6 with the maximum pixel value being normalized to 1. A visual comparison between GF-FBP shown in Figure 2.7 and EF-FBP images evidently indicates that EF-FBP is significantly better than GF-FBP at enhancing edge information for hexagon and square, as GF-FBP mostly yields information about corner points. One drawback of EF-FBP

is that the outer region near the surface of a convex polygonal object is also magnified, since the whisker always makes the contact at one of its corners and the error function may not fully make up for the missing line integrals passing through inside the object needed for tomography. Besides, the longer the length of an edge is, the harder it gets to fully recover the 2-D profile shape of a convex polygonal object via EF-FBP. This is clearly noticeable in the squared-shaped object image in Figure 2.10, despite the fact that it has nearly the same cross-sectional area with the circle and hexagon.

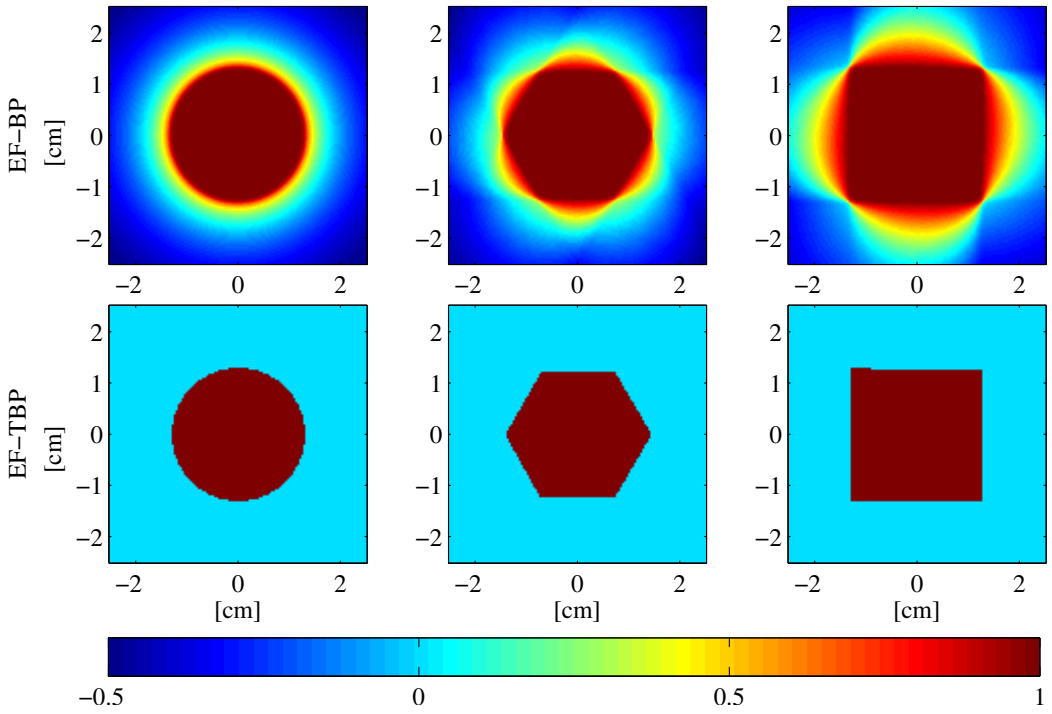

Figure 2.11: The reconstructed 128×128 images using the 2-D Radon transform in Figure 2.9: Top row: the error-function backprojection (EF-BP), bottom row: the error-function thresholded backprojection (EF-TBP).

Figure 2.11 shows the resulting error-function backprojection (EF-BP) and error-function thresholded-backprojection (EF-TBP) images with the maximum pixel value being normalized to 1. Using the error-function-based projection assignment, we demonstrate that we can unconventionally exploit the

smearing effect caused by simple backprojection to recover the enclosed areas corresponding to the convex objects. Similar to the case in EF-FBP, the exterior regions nearby the object boundaries in the resulting EF-BP images take pixel values close to 1. On the other hand, without projection filtering, the smearing effect leads to the enclosed regions represented by the dark-brown-colored pixels corresponding to the convex object shapes. As illustrated in the bottom row of Figure 2.11, we suggest that we can further apply a hard thresholding to extract the area enclosed by each convex object by assigning zeros to the pixels that have values under a pre-defined threshold T and ones to the remaining pixels:

$$\hat{\boldsymbol{x}}_{EF-TBP}[n] = \begin{cases} 0 & \text{if } \hat{\boldsymbol{x}}_{EF-BP}[n] < T, \\ 1 & \text{otherwise.} \end{cases} \tag{2.17}$$

This formulation in Eq. (2.17) can also be considered as a decision rule for Bayesian binary hypothesis testing [41], where the goal is to make a decision between two hypotheses given some observations. Let H_0 and H_1 be the two hypotheses corresponding to the object absence and presence in the given pixel with the prior probabilities π_0 and π_1, respectively. Using the random observation vector $\boldsymbol{z} \in \mathbb{R}^M$ of length M for the value of a pixel, the conditional probability density functions (pdfs) depending on the hypotheses H_0 and H_1 are given by

$$\begin{aligned} H_0 &: \boldsymbol{z} \sim p(\boldsymbol{z}|H_0) \\ H_1 &: \boldsymbol{z} \sim p(\boldsymbol{z}|H_1). \end{aligned} \tag{2.18}$$

The likelihood ratio test (LRT), which yields the optimum Bayesian decision rule is then defined as

$$L(\boldsymbol{z}) = \frac{p(\boldsymbol{z}|H_1)}{p(\boldsymbol{z}|H_0)} \underset{H_0}{\overset{H_1}{\gtrless}} \eta, \tag{2.19}$$

where $L(\boldsymbol{z})$ denotes the likelihood ratio, and η is the threshold value determined based on the priors π_0, π_1 and the cost functions regarding the cost of a decision on one hypothesis when it actually holds or not [41]. In our case, the optimum threshold value cannot be easily determined as it is dependent on the shape of the convex object, and the conditional pdfs for each pixel may differ from one another resulting from the correlations between the pixels, making the problem of finding the optimum threshold value much more complicated. Therefore, the threshold value for EF-TBP has been selected manually, but the ongoing research efforts include the design of a generalized test to compute a near-optimal threshold value.

2.2.3 Limited-Angle Tomography and Sparse Representations

Performing a reduced number of whisks for practical reasons including machinery restrictions and cost savings to recover the shape of a convex object with tomographic reconstruction results in notorious image artifacts due to the incomplete set of measurements collected over a sparsely sampled angular range. Figure 2.12 displays the simulated GF-BP, GF-FBP and EF-FBP image reconstruction results for the circular, hexagonal and square-shaped objects using only a total number of 24 whisks, or equivalently 12 angular views. The artifacts appear as line strips in the resulting images, since the incomplete 2-D Radon transforms have been obtained via a narrow-width Gaussian filter

or the error-function with a narrow-width transition.

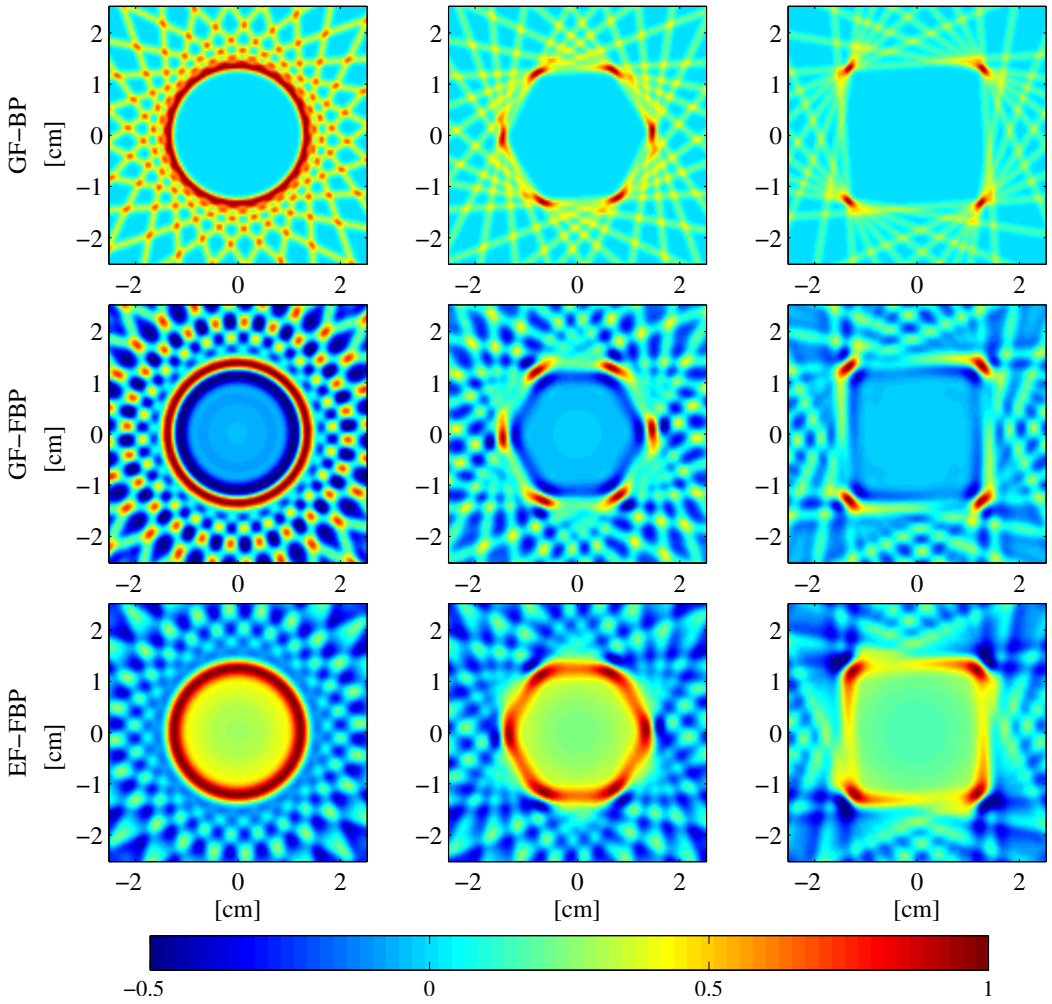

Figure 2.12: The simulated image reconstruction results for GF-BP, GF-FBP and EF-FBP using a total of 24 whisks.

Alternatively, sparse representation models suggest that if a signal is sufficiently sparse in some given representation, then the signal can be nearly recovered from a limited number of linear measurements under noisy conditions by using convex programming [42–45]. Candès, Romberg and Tao [44] showed that a 2-D image can be nearly recovered from its incomplete Fourier samples based on the total-variation norm minimization (TV-min) [46] if the image gradient is sufficiently sparse. The total variation norm of a 2-D signal

$\boldsymbol{X}$ is

$$||\boldsymbol{X}||_{TV} = \sum_{i,j} \sqrt{|\boldsymbol{X}_{i+1,j} - \boldsymbol{X}_{i,j}|^2 + |\boldsymbol{X}_{i,j+1} - \boldsymbol{X}_{i,j}|^2}, \tag{2.20}$$

where $(\boldsymbol{X}_{i+1,j} - \boldsymbol{X}_{i,j})$ and $(\boldsymbol{X}_{i,j+1} - \boldsymbol{X}_{i,j})$ denote the horizontal and vertical image gradients, respectively.

Consider the incomplete and inaccurate set of measurements in the form of a matrix equation

$$\boldsymbol{b} = \boldsymbol{A}\boldsymbol{x} + \boldsymbol{w}, \tag{2.21}$$

where $\boldsymbol{w}$ denotes the additive error term that accounts for measurement noise and other discrepancies including discretization errors, and $\boldsymbol{x} \in \mathbb{R}^N$ is the vector representation of the 2-D signal $\boldsymbol{X}$. The matrix $\boldsymbol{A} \in \mathbb{R}^{M \times N}$ represents the linear operation that yields the real and imaginary parts of the partial 2-D Fourier samples $\hat{X}(f)$ on a star-shaped sampling pattern $f \in \Omega$ consisting of radial lines through the origin [47]. Hence, the length of the resulting measurement vector $\boldsymbol{b} \in \mathbb{R}^M$ becomes much smaller than the length of $\boldsymbol{x}$ ($M << N$). Then, the solution $\hat{\boldsymbol{x}}$ to the convex optimization problem

$$\min ||\boldsymbol{X}||_{TV} \quad \text{subject to} \quad ||\boldsymbol{A}\boldsymbol{x} - \boldsymbol{b}||_2 \leq \epsilon, \tag{2.22}$$

will be close to $\boldsymbol{x}$ for a small amount of error $||\boldsymbol{w}||_2 < \epsilon$, where $||.||_2$ denotes the l_2-norm, and ϵ is a pre-defined parameter provided that the image gradient of $\boldsymbol{X}$ is sufficiently sparse [44, 48].

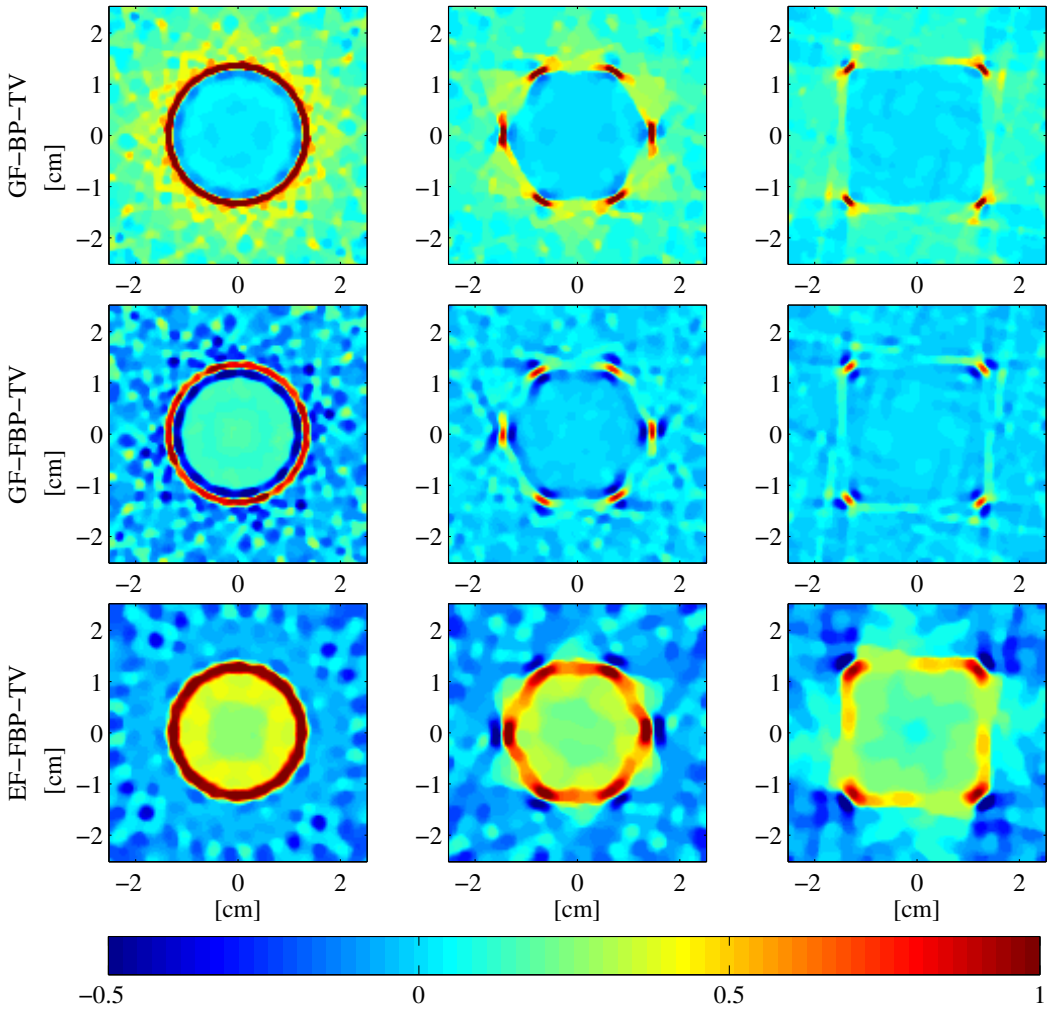

Figure 2.13: The simulation results with a total of 24 whisks after applying the total variation norm minimization (TV-min) over the GF-BP, GF-FBP and EF-FBP images shown in Figure 2.12.

It can be easily shown that the gradients of the GF-BP, GF-FBP and EF-BP images shown in Figures 2.7 and 2.10 produced with the complete data set are sufficiently sparse to apply TV-min to recover accurately with a limited number of whisks, since the resulting images only contain information about vertices and object boundaries. Figure 2.13 displays the simulated 24-whisk GF-BP, GF-FBP and EF-FBP reconstruction results after applying TV-min over the images shown in Figure 2.12. The popular and publicly available

$l1$-magic software package was used to solve Eq. (2.22), which includes a MATLAB code that solves the convex optimization problem by converting the TV-based formulation into a second-order cone programming (SOCP) problem using a generic log-barrier method [48]. As a consequence of the projection-slice theorem, there are the same number of radial lines in the 2-D Fourier domain as the total number of angular views. Therefore, these radial lines were regarded as the sampling pattern to apply TV-min for the limited-angle GF-BP, GF-FBP and EF-FBP. The partial 2-D Fourier transform samples do not exactly match between the images reconstructed through a limited number of whisks and the complete data due to spatial discretization and frequency sampling. Thus, a small positive value of $\epsilon > 0$ was manually chosen to obtain the best possible estimate. The imaging results demonstrate that the image backgrounds were smoothed out by applying TV-min while the object contours were preserved.

A quantitative comparison between the images reconstructed with a limited number of whisks and the images shown in Figures 2.7 and 2.10 using the complete 2-D Radon transforms are presented in Table 2.1 in terms of the relative error, which is defined as

$$r = \frac{||\boldsymbol{x} - \hat{\boldsymbol{x}}||_2}{||\boldsymbol{x}||_2}, \tag{2.23}$$

where the vectors $\hat{\boldsymbol{x}}$ and $\boldsymbol{x}$ correspond to the images reconstructed with a limited number of whisks and using the complete data set, respectively. The relative error results also indicate the improvement on the images after applying TV-min, quantitatively.

Table 2.1: The relative error results for the simulations with a total of 24 whisks for GF-BP, GF-FBP and EF-FBP before and after TV-min.

24 Whisks	**Circle**	**Hexagon**	**Square**
GF-BP	0.4652	0.4574	0.4805
GF-BP-TV	0.3427	0.4014	0.3736
GF-FBP	0.9595	0.8700	0.9184
GF-FBP-TV	0.7111	0.5727	0.6305
EF-FBP	0.4001	0.4004	0.3706
EF-FBP-TV	0.3036	0.3047	0.3106

2.3 Experimental Results

All the experiments were performed at Northwestern University, Evanston, Illinois during July and August 2011, with the same setup built for the previous experiments performed by Solomon and Hartmann [15, 16]. The robotic whisker was made up of a superelastic Nitinol ($E \approx 8 \times 10^4$ MPa) wire, which was 0.5 mm in diameter and 5 cm in length. The whisker was attached to a small aluminum block ($4 \times 4 \times 8$ mm) with a strain gage superglued to each of its four faces although only two of these strain gages were used as only the 2-D cross-sectional imaging of the objects was considered, restricting the bending of the whisker into its axis of rotation. The aluminum block was attached to an aluminum bar with a set screw, and the whole setup was mounted on an AC servomotor with a quadrature encoder with 2048 counts/revolution for actuation. No calibration trials were performed, as the moment measured at the whisker base was not needed to apply the tomographic shape recognition approach. All the measured data was low-pass filtered at 160 Hz, sampled at 1 kHz, and passed through a zero-phase digital filter with a cut-off frequency of 50 Hz.

The proposed method was tested for the 2-D imaging of the objects that were made of aluminum bars with three different cross-sections including circle, hexagon and square. The real objects were positioned the same as the virtual objects illustrated in Figure 2.4.

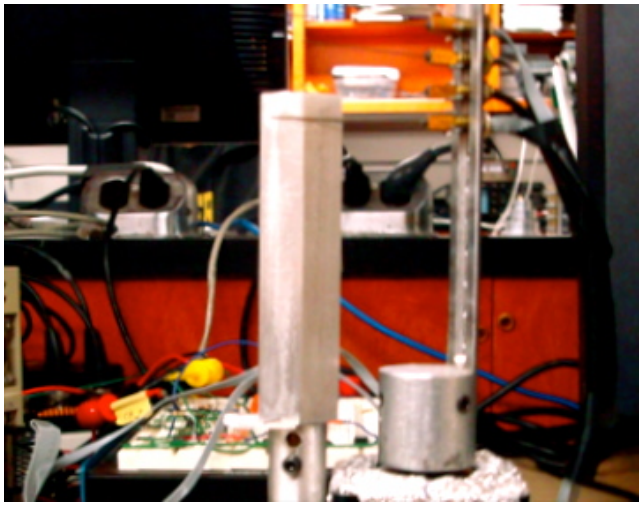

Figure 2.14: The experimental setup for object shape recogition: The whisker was rotated against the objects that were made of aluminum bars with three different cross-sections including circle, hexagon and square.

As shown in Figure 2.14, the whisker base was positioned to the right of the test object centers at a distance of 4 cm for circle and hexagon and 4.2 cm for square. The pulses were sent to the AC servomotor at 100 Hz and the whisker was rotated against the object until a small amount of bending was attained, immediately retracting back to its initial position at rest. For experimental purposes, rather than moving the whisker around the stationary object for the next angular view, each object was rotated about its center while keeping the whisker base fixed in space. This is simply the same as having the whisker base move around the object circularly. The whisker was rotated by 5° between two consecutive whisks, completely scanning the region

surrounding the object through $360^\circ/5^\circ = 72$ whisks.

2.3.1 Practical Considerations

In practice, it is not quite possible to find the exact second parallel whisker path due to measurement errors. Therefore, for the Gaussian-function-based approach, the projection values are assigned using only a single Gaussian function at each whisk, since the second whisker path is missing due to the angular error. However, this error will be compensated by the neighboring angular views as they will add up together during the image reconstruction if the angular error is small. Therefore, in practice, the projections are assigned as two separate projection vectors with a small angular difference of $\Delta\phi$:

$$p(t,\phi) = f(t_1,\phi) \quad \text{and} \quad p(t,\phi+\Delta\phi) = f(t_2,\phi+\Delta\phi). \tag{2.24}$$

For the error-function-based projection assignment approach, we make use of the fact that the whisker paths do not shift significantly between the two consecutive views provided that the amount of rotation to the succeeding view is relatively small. This suggests that we can treat one of the whisker paths from the preceding view as a second whisker path for the current view to be able to apply the error-function projection assignment procedure with a small amount of error. Therefore, we slightly modify the projection assignment procedure for the two whisker paths lying at the opposite sides:

Case I: $t_1 < 0$ **and** $t_2' \geq 0$

$$p(t,\phi) = \begin{cases} g(t_1,\phi) & \text{if } t \leq t_2', \\ g(t_1,\phi)g(t_2',\phi') = -1 & \text{otherwise.} \end{cases} \tag{2.25}$$

Case II: $t_2 \geq 0$ **and** $t_1' < 0$

$$p(t,\phi) = \begin{cases} g(t_1',\phi')g(t_2,\phi) = -1 & \text{if } t < t_1', \\ g(t_2,\phi) & \text{otherwise,} \end{cases} \tag{2.26}$$

where t_1' and t_2' correspond to the signed distances at the very initial contact from the preceding view for the two cases, respectively.

2.3.2 Image Reconstruction

The 2-D Radon transforms regarding the circular, hexagonal and square-shaped objects generated by physically performing a total number of 72 whisks at equally spaced (5°) intervals around each object are shown in Figure 2.15 for the Gaussian-function and the error-function projection assignments with $\sigma = 0.05$ and $M = 183$. As it was not feasible to find an exact second parallel whisker path at a particular angular view due to the angular measurement errors, the projection assignment procedures summarized in Eqs. (2.24)-(2.26) were applied to compute the 2-D Radon transform for each object, totaling a number of generated projections $M \cdot L = 183 \cdot 72 = 13176$. The angular measurement error at each whisk was defined as the absolute difference between the angular values computed in the simulations and measured in the experiments at the very initial contact for the same whisker-base location. The resulting experimental angular error averaged over 72 whisks for each object

is presented in Table 2.2.

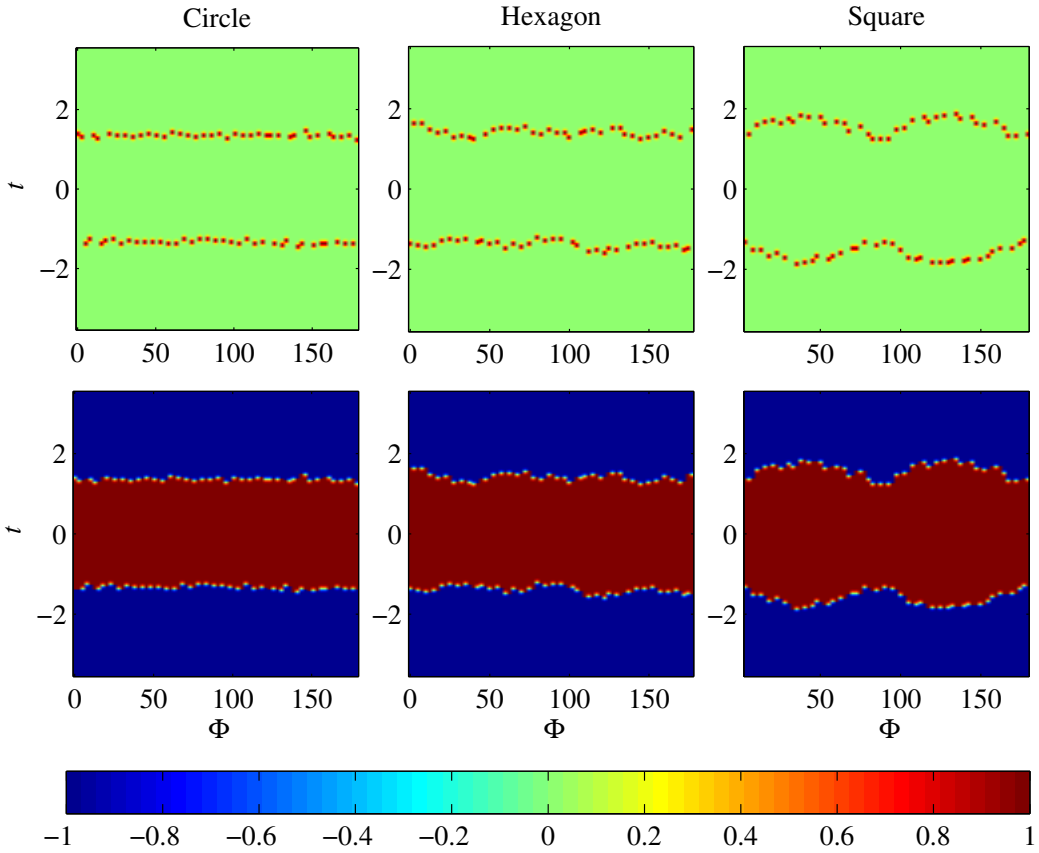

Figure 2.15: The Radon transforms generated for the experiments using the Gaussian-function (top) and the error-function (bottom) projection assignments with $\sigma = 0.05$.

Table 2.2: The experimental average angular measurement error for the circular, hexagonal and square-shaped objects.

Circle	**Hexagon**	**Square**
0.8708°	1.0030°	0.7901°

Figures 2.16 and 2.17 present the experimental results using the 2-D Radon transforms shown in Figure 2.15 obtained through Gaussian and error-function projection assignments for the circular, hexagonal and square-shaped objects, respectively. The corresponding relative error results are also given in Table

2.3. The resulting 128×128 images were reconstructed via the measurement matrix $\boldsymbol{H}_{13176\times16384}$ generated using the initial contact angles recorded at the whisker base. The green contours drawn in the EF-BP and EF-TBP images correspond to the actual object boundaries, and the threshold for EF-TBP was manually chosen to be as close to 1 (the maximum pixel value) as possible ($T = 0.96$) to obtain the best possible estimates.

The experimental results demonstrate that the tomographic approach produces accurate image representations of all three object shapes. As expected, the contact points recovered for the hexagonal-shaped object via GF-BP and GF-FBP were slightly more dispersed than for the square, increasing the relative error for the hexagon, since the average angular measurement error for the hexagon was the largest among the three objects tested for the tomographic approach.

Edge enhancement was achieved by GF-FBP, at the cost of significantly increasing error because the line strips were also intensified due to the projection filter that boosts the high frequency information. This problem has been mitigated in EF-FBP by compensating for the missing line integrals passing through inside the object, where using the error function provides a clear distinction between the area inside which the object lies and the free-whisking region in generating the 2-D Radon transform, further enhancing object boundaries while reducing the effects of line strips observed in the image background. The results for EF-BP and EF-TBP suggest that the region occupied by an object can be easily recovered with a small amount of error. Therefore, simple backprojection tomography with hard-thresholding may be essentially feasible to find a rough estimate of some of the object features including size, shape and location.

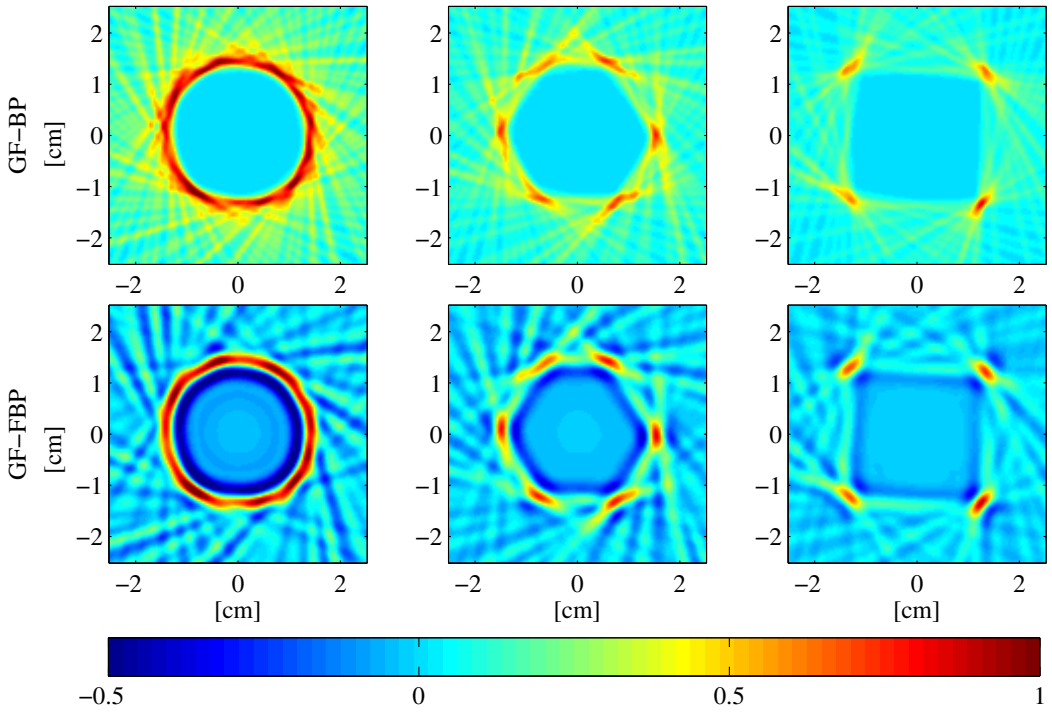

Figure 2.16: The reconstructed 128×128 GF-BP and GF-FBP images using the 2-D Radon transform shown in the top row of Figure 2.15 computed by performing 72 whisks at evenly spaced (5°) intervals around the object.

The experimental errors are mainly caused by the imprecise measurements of the angle at the whisker base during the very initial contact, which implies that the estimated whisker paths become slightly tilted from their actual positions due to angular errors. This may particularly be a problem for the recovery of the corners of a convex polygonal object via the Gaussian-function projection assignment, since the estimated straight whisker paths from different angular directions may not intersect at the same point for a given corner. However, as the tomographic image is obtained through uniformly adding the projection values to the pixels lying along the straight lines, using the standard deviation σ as a control parameter to adjust the width of the Gaussian filter provides some confidence interval in estimating these corner points, instead of computing the radial distance to obtain single estimates of the same contact

point with some error at different whisks. This is also useful for the recovery of edges and curved object contours via EF-FBP as the value of σ also determines the width of the transition region that separates the area inside of the object from the outer free-whisking area in the reconstructed images.

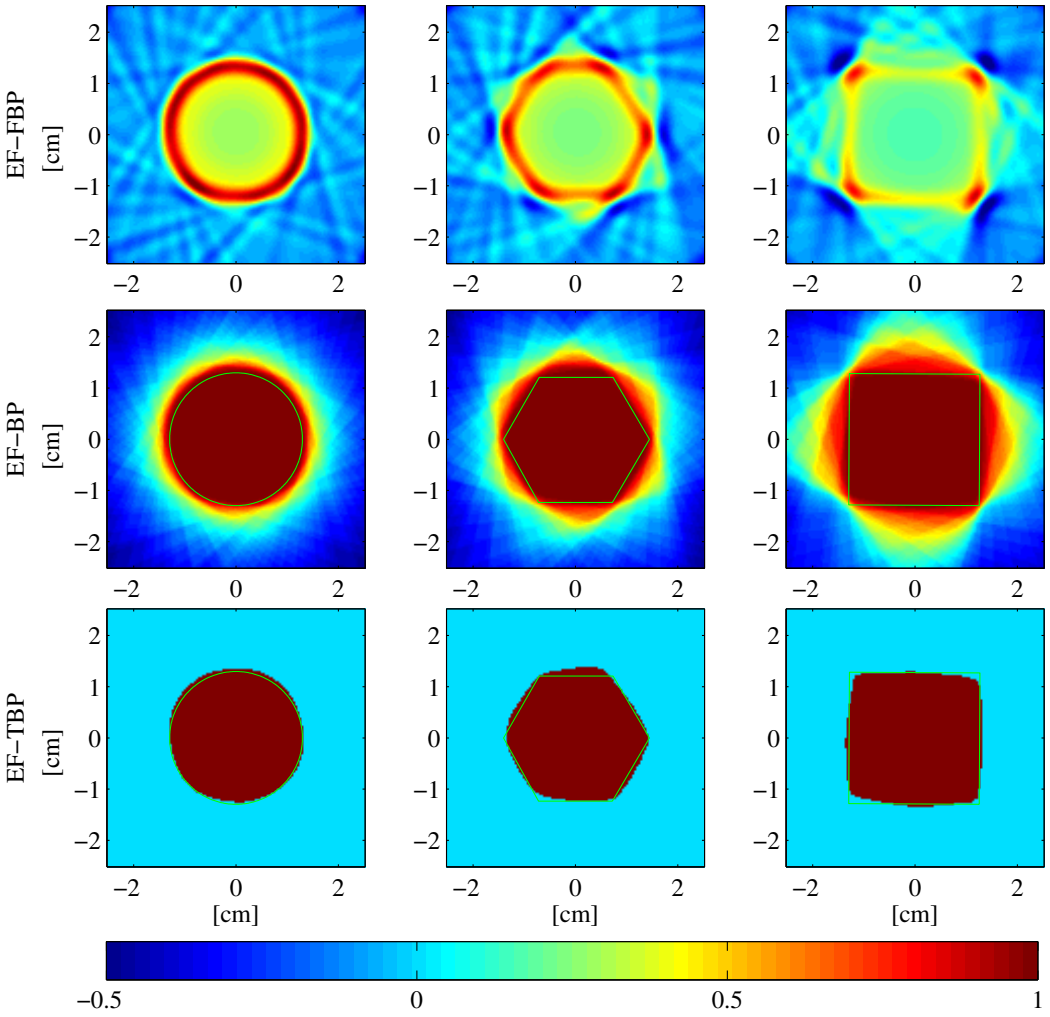

Figure 2.17: The reconstructed 128×128 EF-FBP, EF-BP and EF-TBP images using the 2-D Radon transform shown in the bottom row of Figure 2.15 computed by performing 72 whisks at evenly spaced (5°) intervals around the object with the threshold $T = 0.96$ for EF-TBP.

Table 2.3: The relative error results for the experiments with a total of 72 whisks at evenly spaced (5°) intervals for GF-BP, GF-FBP, EF-FBP, EF-BP and EF-FBP.

72 Whisks	**GF-BP**	**GF-FBP**	**EF-FBP**	**EF-BP**	**EF-TBP**
Circle	0.3831	0.7094	0.3343	0.1312	0.2335
Hexagon	0.3869	0.7303	0.3512	0.1169	0.2811
Square	0.3481	0.6150	0.2797	0.0695	0.2430

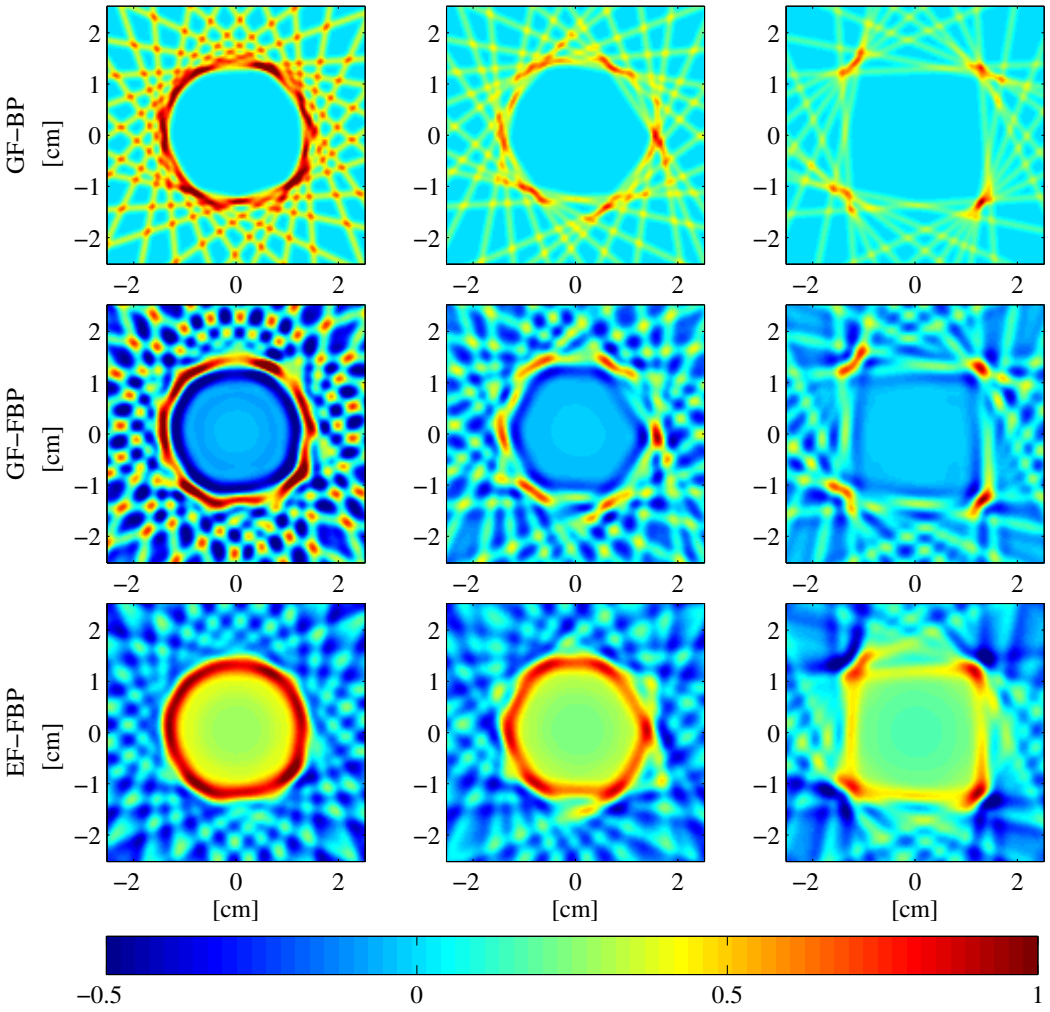

Figure 2.18: The experimental image reconstruction results for GF-BP, GF-FBP and EF-FBP using a total of 24 whisks at evenly spaced (15°) intervals.

We also evaluated the performance of the sparse representations model based on the total-variation-norm minimization under noisy conditions. The imaging results produced with a total number of 24 whisks at evenly spaced (15°) intervals for GF-BP, GF-FBP and EF-FBP before and after applying TV-min are shown in Figures 2.18 and 2.19, respectively. The corresponding relative errors are given Table 2.4. Using a set of noisy measurements collected by performing only 24 whisks around each object has produced images with severe artifacts and increased inaccuracy as clearly seen in Figure 2.18. The object shapes were recovered with more uncertainty, particularly for GF-BP and GF-FBP as the dispersion along the circular boundary and near the corner points for hexagon and square are disturbingly noticeable due to angular measurement errors.

Table 2.4: The relative error results for the experiments with a total of 24 whisks at evenly spaced (15°) intervals for GF-BP, GF-FBP and EF-FBP before and after TV-min.

24 Whisks	**Circle**	**Hexagon**	**Square**
GF-BP	0.5828	0.6062	0.6250
GF-BP-TV	0.5425	0.5648	0.5063
GF-FBP	1.1628	1.1527	1.2095
GF-FBP-TV	0.9176	0.9535	0.9098
EF-FBP	0.5173	0.5159	0.4923
EF-FBP-TV	0.4830	0.4812	0.4378

Applying TV-min over the images generated with a limited number of whisks has reduced the image artifacts in the background significantly as seen in Figure 2.19. In the case of GF-FBP, which results in the largest relative error, the TV-min performance has been degraded by the reduced sparsity level due to the dispersion of the curved boundaries and corner points, giving

rise to the corresponding pixel values also being suppressed while eliminating the line strips in all of three object shapes.

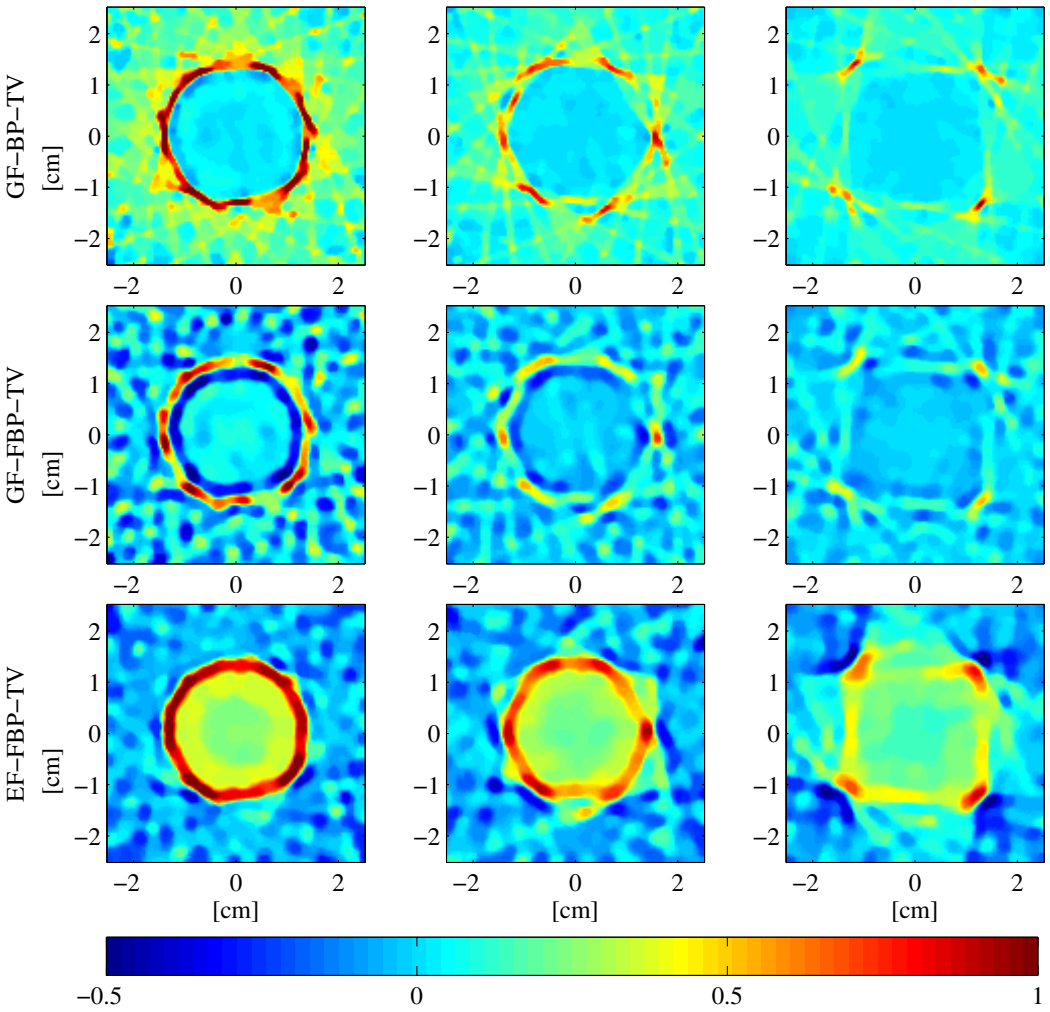

Figure 2.19: The experimental results with a total of 24 whisks at evenly spaced (15°) intervals after applying TV-min over the GF-BP, GF-FBP and EF-FBP images shown in Figure 2.18.

Figure 2.20 shows the relative error comparison between the five different image reconstruction methods averaged over the simulation and experimental results for the circular-, hexagonal- and square-shaped objects before applying TV-min with a total number of whisks ranging from 8 to 72. The comparison of simulation and experimental relative error results before and after applying

TV-min for GF-BP, GF-FBP and EF-FBP are presented in Figure 2.21.

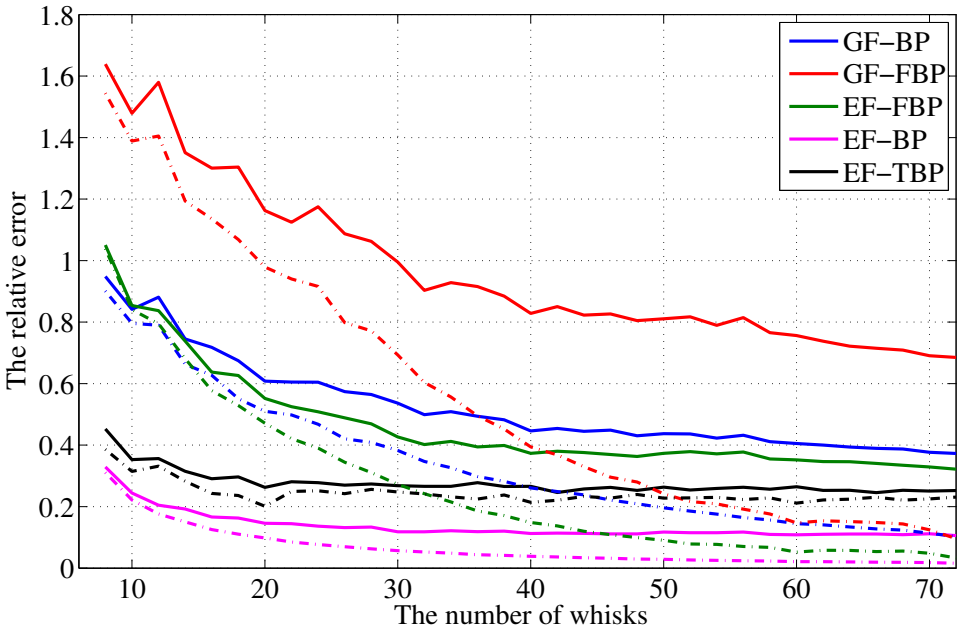

Figure 2.20: The relative error results of the simulations (dash-dotted lines) and experiments (solid lines) for GF-BP, GF-FBP, EF-FBP, EF-BP and EF-TBP with a total number of between 8 and 72 whisks.

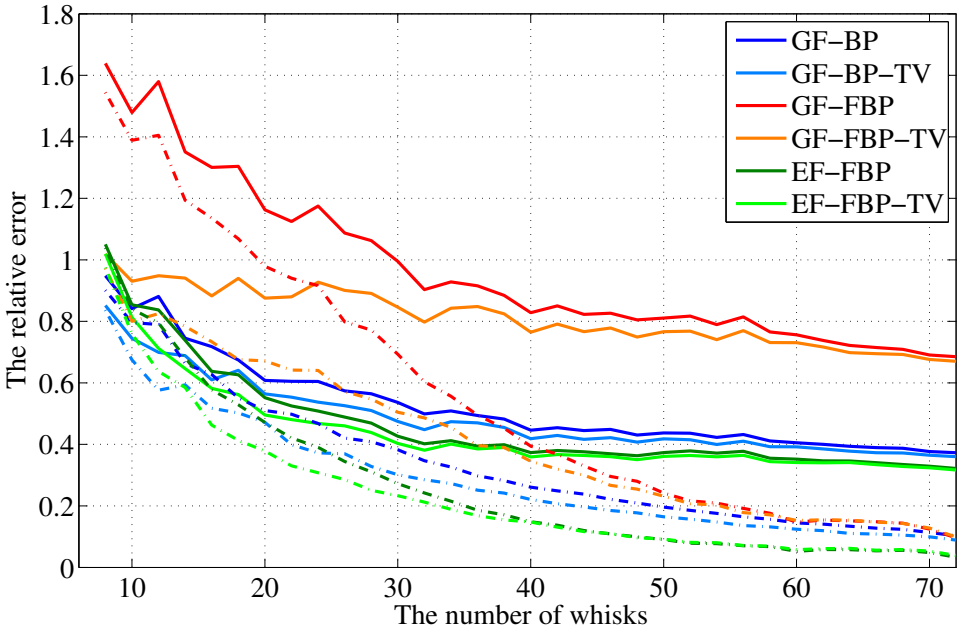

Figure 2.21: The relative error results of the simulations (dash-dotted lines) and experiments (solid lines) for GF-BP, GF-BP-TV, GF-FBP, GF-FBP-TV, EF-FBP and EF-FBP-TV with a total number of between 8 and 72 whisks.

The overall relative error results indicate that GF-FBP is more prone to incomplete and inaccurate measurements compared to the other reconstruction methods. As clearly seen in Figure 2.20, the gap between the simulations and experiments is the largest for GF-FBP, which is solely due to the boost in high-frequency components while the edge information is not sufficiently enhanced to suppress the background noise as opposed to the case in EF-FBP. On the other hand, the TV-min results illustrated in Figure 2.21 also show that the largest error reduction is achieved for GF-FBP, while the error gap between the simulations and experiments is relatively small for GF-BP and EF-FBP. As expected, the error reduction achieved via TV-min decreases with increasing the total number of whisks, since TV-min becomes less effective for a higher number of whisks as the 2-D Fourier space becomes less sparse. The relative error results for EF-BP and EF-TBP suggest that a relatively small number of whisks could be sufficient to recover the enclosed areas corresponding to the convex objects as the rate of error stays almost constant above nearly 25 whisks for both cases as seen in Figure 2.20.

2.4 Discussion

The tomographic approach presented in this dissertation for the tactile shape recovery with a robotic whisker has demonstrated that the cross-sectional image representations of the profile shapes have been extracted highly accurately for three distinct objects. The 2-D Radon transform computed for each object based on straight initial-contact whisker paths provides some valuable characteristic information about object boundaries using the two related but slightly different projection assignment methods for tomographic reconstruc-

tion. Hence, using the same angular measurements, it has been shown that it is possible to obtain several different cross-sectional image reconstructions regarding the same object with small errors. Since the technique proposed here only uses the angle at the whisker base measured at the very initial contact, it is very sensitive to angular errors, which were observed to be as large as $\sim 3^{\circ}$ per single whisk. However, the effects of such large errors were alleviated by the nature of tomography, in which some form of confidence interval was generated to reliably extract corner points and curved or flat surfaces, using the projection assignment based on a Gaussian filter rather than a Kronecker-delta function, and the error function with a transition region much smoother than a rectangular function to compute the 2-D Radon transform.

The key advantage of integrating tomography into tactile shape recovery is that it enables the extraction of object features without using torque information measured at the whisker base, which might introduce additional errors if the calibration is made improperly. On the other hand, the proposed technique requires a full rotation around the object of interest with the angular space between the two consecutive whisks to be as small as possible for an accurate estimation of the 2-D shape. As expected, increasing the number of whisks results in better estimates of the object profile shapes. However, even with a small number of whisks, some valuable information can be achieved particularly through EF-FBP and EF-TBP such as a rough estimate of the object size, shape and location. Furthermore, the image reconstruction results for GF-BP, GF-FBP and EF-FBP with a limited number of whisks have demonstrated that the image artifacts observed as line strips were solely due to applying BP/FBP directly and eliminated using a sparse representation model based on TV-minimization. Therefore, the corner points and object

contours were recovered reliably with a smaller number of whisks at the cost of increased amount of computation. Another possibility would be to develop an alternative sparse reconstruction model that formulates the estimation of vertices of convex polygonal-shaped objects with a limited number of whisks as a "vertex localization" problem, rather than applying TV-min, because using the Gaussian filter as a point-spread function makes the actual problem inherently sparse.

There are several implicit assumptions made in the tomographic 2-D object shape recovery method regarding surface roughness, compliance, convexity and movement. The tomographic approach was only tested for objects with smooth surfaces, and hence the effect of friction on the estimation of contact points and object boundaries was not taken into account. As discussed above, tomography should mitigate the effects of additional angular errors resulting from surface roughness, but more empirical evidence is needed to evaluate how badly the surface friction would reduce accuracy in the estimation of object contours. Moreover, the proposed method fails to extract any concavity in the object contours as it can only recover the 2-D cross-sectional convex hull of an object, connecting the concave regions of an object via straight whisker paths in the reconstructed images. Therefore, whisker tip contact, which was also not tested, may be adapted for the algorithm as it would provide a better way to extract concave object features using straight robotic whiskers due to the geometrical constraints.

The contact of the robotic whisker with a nonrigid object may result in some level of inaccuracy in the angular measurements at the whisker base as a result of object compliance unless the robotic whisker itself is thin and flexible enough not to cause any deformation along the object boundary. However, this

may also become a serious problem as it would be much harder to observe a sudden voltage rise sensed by the strain gages positioned at the whisker base to determine the angle at the very initial contact, giving rise to additional angular errors. Furthermore, the static assumption fails when the object of interest is in motion or loosely fixed, and hence changing its position due to factors such as high-speed whisking. In such cases, tomographic reconstruction would result in significant errors and image artifacts. There are techniques that use curve-evolution methods to jointly estimate the time-varying object boundaries from sparsely sampled tomographic data with spatial-temporal regularization [49, 50]. Further research is needed to adapt some of these dynamic, tomography ideas to develop a model for nonstationary shape recognition of compliant and moving objects with robotic whiskers.

The tomographic approach for tactile shape recovery may be included in the class of whisker-tapping techniques [6–10, 15, 17] as it only uses the information based on moving the whisker against an object through small angles, although the radial distance extraction of the contact point along the length of the whisker was not considered. Therefore, the technique presented here has some limitations in comparison with the more advanced sweeping methods developed in [13, 14, 16]. As discussed in [16], a more natural way of imitating the rat's whisker movement should be to use the bending moment measured at the whisker base to extract multiple contact point locations beyond the initial contact. On the other hand, the whisker tomography method can be regarded as a "convex hull" estimator, where the object contours are recovered through only a few contact points along the object contours, and hence any information obtained by sweeping along the object surface beyond the initial contact is disregarded. This means that the proposed algorithm is incapable of

estimating the contact point locations when the whisker makes contact along a continuous segment of a convex object, and hence may not be preferable if it is desired to extract more detailed information about the object profile shape over a single whisk using an artificial whisker.

In this dissertation, the main objective is to develop an "object localization" algorithm to roughly estimate object features including size, shape and location, which would serve as a supplementary information for the tactile fluid-flow tomography model introduced in the next chapter with the ultimate goal of tactile imaging of surroundings using robotic whiskers. Further research may yet enable the use of whisker-tip contact or non-straight whisker paths by integrating torque information measured beyond the initial contact, which can also expand the tomographic approach to 3-D object feature extraction using a robotic whisker array. This would, however, require a more sophisticated model as the modified algorithm should also account for lateral slip, which occurs when the robotic whisker comes into contact with an object boundary in a sloping position compared to the plane of rotation [7, 10, 15]. Such a future extension of the new simple tomographic shape recovery model presented here would be especially useful in determining the location of an object in 3-D space under noisy conditions as a part of an advanced robotic whisker system to do tasks including navigation, simultaneous localization and environmental mapping.

CHAPTER 3

Tactile Fluid-Flow Imaging with Robotic Whiskers

The use of an array of facial whiskers is very crucial to many mammals including rats, seals and shrews to implement complicated tasks such as navigation, object localization and obstacle avoidance. Therefore, this advanced sensing mechanism has drawn growing attention from robotics engineers. Lungarella et al. [11] and Fend et al. [12] developed artificial whisker systems based on the power spectral density analysis of the signal measured from whisker sensors for texture discrimination, inspired by the rat somatosensory system. Pearson et al. [18, 19] and Fox et al. [20] have constructed advanced active touch robotic whisker array systems for shape recognition, texture discrimination and navigation, motivated by the neural-processing of the rat's whisker control.

Another important task performed by vibrissal-sensing animals such as seals is that they can extract fluid-flow characteristics including local currents and wake disturbances with their array of whiskers [3], which has not been fully exploited by the robotics community. Solomon and Hartmann [17] demonstrated that using two opposing whisker arrays, it is possible to determine the velocity profile of a stream of air moving toward the center of the whisker array, generating single estimates of the air-flow velocity at a given height. However, the high-resolution recovery of the 2-D cross-section of the fluid-flow velocity-field using tactile sensing still remains an important unsolved problem, which would offer an essentially novel sensing mechanism for

flow-field measurements.

In this dissertation, we develop a novel tactile imaging technique for fluid-flow sensing, where we model "whisking" as a tomographic imaging process to extract the 2-D characteristics of the fluid-flow. We further generalize the tomographic approach with artificial whiskers introduced in Chapter 2 for object shape recovery by developing a more advanced physical model for the imaging of surroundings with a robotic whisker array. We treat the moment measurements at the whisker base on a whisker array as the projections collected at each angular view for the tomographic reconstruction of the 2-D cross-sectional mean fluid-flow velocity-field. We also present a dynamic tomographic solution under the linear state-space model for the 2-D imaging of the time-varying flow patterns, in which the linear minimum mean squared error (LMMSE) estimates are recursively computed using the Kalman filter [26–29]. This dynamic tactile imaging approach to fluid-flow sensing may make it possible to perform sophisticated tasks such as the detection of a nearby surface as it alters the flow before the actual whisker contact or the tracking of a moving object by its wake, presenting a strong alternative to vision systems particularly in dark or muddy environments, where visibility is near zero.

This chapter presents the image reconstruction methods for the cross-sectional tomographic imaging of the 2-D fluid-flow velocity field with a robotic whisker array. First, the fluid-mechanics fundamentals for sensing with whiskers are explained in Section 3.1. Then, the forward model for the tactile fluid-flow tomographic imaging is described in Section 3.2. The chapter concludes with the inverse problem formulation for the cases of static and dynamic imaging with a whisker array in Section 3.3 and Section 3.4, respectively.

3.1 The Moment at the Whisker Base and the Drag Force

The drag is the force applied by the fluid on a solid object in the direction of fluid-flow, and at high Reynolds number, it is proportional to the relative velocity squared, whether the flow is laminar or turbulent. The Reynolds number is defined as the ratio between the viscous and inertial forces in a fluid, and hence is a dimensionless parameter given by

$$Re = \frac{\rho V L}{\mu}, \tag{3.1}$$

where ρ is the fluid density, and V is the relative velocity. The dynamic fluid viscosity is represented by μ, whereas the characteristic length is denoted by L [24]. The cross-sectional area for a circular cylinder of length l and diameter d is defined to be $A = ld$ with its axis normal to the flow direction. Therefore, the characteristic length for a cylinder becomes $L = d$ [51].

Assuming the artificial whisker to be a straight cylindrical beam with substantial stiffness, the equation for the *drag force per unit length*, f_D, on a circular cylinder is given by

$$f_D = \frac{1}{2}\rho C_D V^2 d, \tag{3.2}$$

where the drag coefficient C_D is a dimensionless number that depends on the Reynolds number. It has been shown experimentally that the drag coefficient is nearly fixed ($C_D \approx 1.2$) in the range of $100 < Re < 3 \times 10^5$ for the circular cylinder, and hence the drag force on a whisker segment becomes proportional to the square of the relative fluid-flow velocity normal to the whisker segment

[24, 51].

The drag force on a whisker segment acts as a distributed load along the whisker length as illustrated in Figure 3.1. The distributed load $p(s)$ on a straight beam may also be characterized in terms of the *force per unit length*, such that the load applied by the distributed load $p(s)$ to a small segment of the beam length ds is $p(s)ds$ [25]. If the whisker base at the location $s_0 = 0$, then the incremental moment of $p(s)$ around the whisker base becomes $sp(s)ds$, yielding the moment at the whisker base

$$M_{base} = \int_0^L sp(s)ds, \tag{3.3}$$

which can be described as the weighted integral of the distributed load along the whisker of length L.

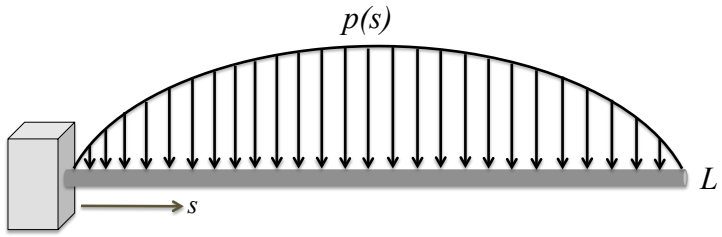

Figure 3.1: The distributed load along the whisker length: The moment sensed at the whisker base is the weighted integral of the drag force which acts as a distributed load along the whisker length.

If the whisker is divided into R equally spaced segments along its length with the grid spacing $\Delta s = L/R$, then the moment integral given in Eq. (3.3)

can be approximated by

$$M_{base} = \int_0^L p(s)sds \approx \sum_{r=1}^{R} p(s_r + \Delta s/2)(s_r + \Delta s/2)\Delta s$$
$$= \frac{1}{2}\rho C_D d \sum_{r=1}^{R} V_r^2 \mathrm{sgn}(V_r)(s_r + \Delta s/2)\Delta s, \quad (3.4)$$

where the position $(s_r + \Delta s/2)$ corresponds to the center of the rth whisker segment, V_r is the fluid-flow velocity normal to the flow direction at $(s_r + \Delta s/2)$ with $\mathrm{sgn}(V_r)$ describing the forward/backward direction via the sign function sgn.

3.2 The Forward Model

In tomography, the unknown physical field is characterized by the set of line-integrated observations collected by multiple sensors from different directions. Hence, the relation between the observations and the unknown field tomography can be given by the Fredholm equation of the first kind [52]

$$y_i(\boldsymbol{l}) = \int_{\mathcal{L}} h_i(\boldsymbol{l}; \boldsymbol{l}') x_i(\boldsymbol{l}') d\boldsymbol{l}', \quad (3.5)$$

where $x_i(\boldsymbol{l})$ and $y_i(\boldsymbol{l})$ represent the unknown physical field and the measurements at time $t = t_i$ given by the time index i, respectively. Besides, $h_i(\boldsymbol{l}; \boldsymbol{l}')$ denotes the observation kernel function and $\mathcal{L} \subset \mathbb{R}^2$ is the region of support. For the 2-D cross-sectional tactile flow-imaging case, $\boldsymbol{l}$ represents the 2-D position vector, and $y_i(\boldsymbol{l})$ corresponds to the moment values measured at the whisker base on a whisker array. Therefore, if we collect these moment measurements from different directions, it becomes possible to map out the 2-D

fluid-flow velocity field $x_i(\boldsymbol{l})$ through the tomographic reconstruction of the 2-D cross-sectional drag-force distribution.

Figure 3.2 illustrates an example of the 2-D imaging geometry of tactile fluid-flow tomography using the moment values measured by an array of whiskers. The whisker array configuration allows rotations only around the whisker base. Also, when the fluid flows inside a pipe or an open channel, the whisker rotation is restricted by the wall boundaries, which leads to a sparser sampling near the walls, whereas the regions near the flow surface are relatively densely sampled. Thus, it is not possible to collect measurements for the entire angular range. Similar to the other tomographic techniques such as ionospheric and seismic tomography [53–55], the geometrical constraints on the whisker rotation in tactile fluid-flow tomography lead to a nonuniform sampling of the region of support with only a small number of angular views, which could be regarded as a type of a limited-angle tomography problem.

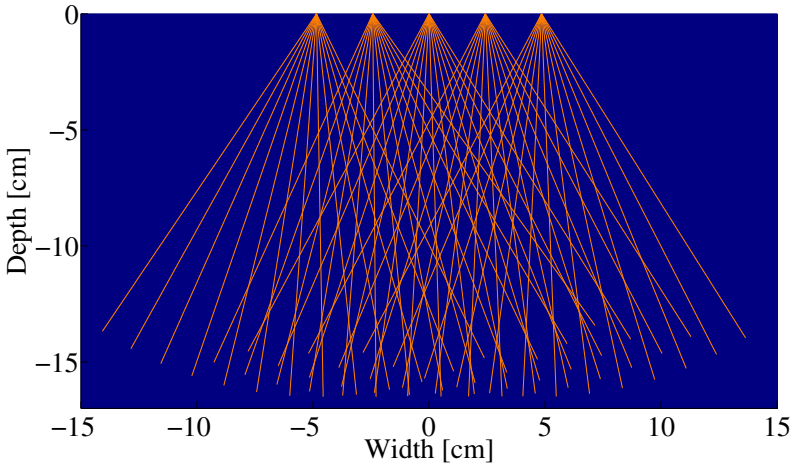

Figure 3.2: The 2-D imaging geometry of tactile fluid-flow tomography based on the moment values measured at the whisker base: The geometrical constraints on the whisker rotation in tactile flow tomography leads to a nonuniform sampling of the region of interest.

The restrictions on the data acquisition geometry thus prohibit the use of classical tomography methods such as the Radon transform or the projection-slice theorem, as opposed to the medical tomography applications. Therefore, in order to obtain an approximate solution to this particular inverse problem using numerical techniques, the unknown field $x_i(\boldsymbol{l})$ needs to be discretized. This can be achieved by using a finite basis expansion such as a rectangular pixel array as follows:

$$x_i(\boldsymbol{l}) = \sum_{k=1}^{N} \boldsymbol{x}_i[k]\beta_k(\boldsymbol{l}), \tag{3.6}$$

where $\beta_k(\boldsymbol{l})$ is the kth basis function, N is the total number of basis functions, and $\boldsymbol{x}_i[k]$ is the kth element of the set of coefficients $\boldsymbol{x}_i$ of length N. Using a rectangular pixel array of size $a \times b$, the unknown field $x_i(\boldsymbol{l})$ can be represented by the image coefficient vector $\boldsymbol{x}_i$, where $N = a \cdot b$ and $\boldsymbol{x}_i[k]$ corresponds to the kth pixel value.

In practice, we have to cope with noisy and inaccurate measurements. Self-noise from resistive sensors is known to be approximately Gaussian, since the tomographic measurement is an integral of flow-noise distribution along each whisker. The central limit theorem suggests that the cumulative measurement noise should be approximately Gaussian. Therefore, considering a linear additive-Gaussian-noise signal model, we can write the linear observation model in the matrix form at time index i as

$$\boldsymbol{y}_i = \boldsymbol{H_i}\boldsymbol{x_i} + \boldsymbol{w_i}, \tag{3.7}$$

where $\boldsymbol{x}_i$ is the vector representation of the unknown image of length N and $\boldsymbol{y_i}$ is the measurement vector of length M. The linear matrix operator $\boldsymbol{H}_i \in \mathbb{R}^{M \times N}$ relates the measurements $\boldsymbol{y}_i$ to the unknown image coefficients $\boldsymbol{x}_i$ with

the additive noise vector $\boldsymbol{w}_i$ of length M, which accounts for sensor noise as well as model uncertainties including the discretization of the image field and other approximations.

Each element of the linear matrix operator $\boldsymbol{H}_i$ is given by

$$[\boldsymbol{H}_i]_{(j,k)} = \int_{\mathcal{L}} h_i(\boldsymbol{l}_j; \boldsymbol{l}')\beta_k(\boldsymbol{l}')d\boldsymbol{l}', \tag{3.8}$$

where $h_i(\boldsymbol{l}_j; \boldsymbol{l}')$ is the observation kernel function for the jth moment measurement. Hence, in the image plane, $[\boldsymbol{H}_i]_{(j,k)}$ represents the contribution of the kth pixel to the line integral along the jth whisker path.

Using Eq. (3.4), the jth moment measurement $\boldsymbol{y}_i[j]$ can be approximated by

$$\boldsymbol{y}_i[j] \approx \frac{1}{2}\rho C_D d \sum_{k\in K} V_k^2 \mathrm{sgn}(V_k) \sum_{r\in R_k} w_{kr} \cdot (s_r + \Delta s/2)\Delta s + \boldsymbol{w}_i[j], \tag{3.9}$$

where K is the set of pixels on which the jth whisker lies within a distance of T from the pixel center, which is defined as

$$K = \{k \in \mathbb{N} : 1 \leq k \leq N, ||\boldsymbol{l}_k - \boldsymbol{l}_{kj}||_2 < T\},$$

where $\boldsymbol{l}_k$ and $\boldsymbol{l}_{kj}$ are the position vectors of the center of the kth pixel and its vector projection onto the jth whisker path, respectively. The value of the pixel $k \in K$ is then given by $V_k^2\mathrm{sgn}(V_k)$, and the set of whisker segments in its close proximity is defined as

$$R_k = \{r \in \mathbb{N} : 1 \leq r \leq R, ||\boldsymbol{l}_k - \boldsymbol{l}_r||_2 < T\},$$

where $\boldsymbol{l}_r$ is the position vector of the center of the rth whisker segment. The weighting factor w_{kr} is inversely proportional to the Euclidean distance between the center of the pixel $k \in K$ and the whisker segment $r \in R_k$.

The matrix element $[\boldsymbol{H}_i]_{(j,k)}$ can then be rewritten as

$$[\boldsymbol{H}_i]_{(j,k)} = \frac{1}{2}\rho C_D d \sum_{r \in R_k} w_{kr} \cdot (s_r + \Delta s/2)\Delta s. \tag{3.10}$$

3.3 Static Tactile Fluid-Flow Tomography

The resulting inverse problem is the reconstruction of the 2-D cross-sectional fluid-flow characteristics from the 1-D moment measurements. If the unknown flow field is sufficiently static during the measurement interval or it is desired to map out the cross-sectional mean fluid-flow characteristics over a short period of time, the 2-D image can be reconstructed using the measurement set

$$\begin{bmatrix} \boldsymbol{y}_1 \\ \boldsymbol{y}_2 \\ \vdots \\ \boldsymbol{y}_L \end{bmatrix} = \begin{bmatrix} \boldsymbol{H}_1 \\ \boldsymbol{H}_2 \\ \vdots \\ \boldsymbol{H}_L \end{bmatrix} \boldsymbol{x} + \begin{bmatrix} \boldsymbol{w}_1 \\ \boldsymbol{w}_2 \\ \vdots \\ \boldsymbol{w}_L \end{bmatrix}, \tag{3.11}$$

where the stationary unknown field $\boldsymbol{x}$ has no temporal variation, and L is the number of time instants considered for static reconstruction. Then, the estimate for $\boldsymbol{x}$ is found by the measurement vector $\boldsymbol{y} = [\boldsymbol{y}_1^T, \boldsymbol{y}_2^T, \cdots, \boldsymbol{y}_L^T]^T$ of length $M \cdot L$ and the forward model matrix $\boldsymbol{H} = [\boldsymbol{H}_1^T, \boldsymbol{H}_2^T, \cdots, \boldsymbol{H}_L^T]^T \in \mathbb{R}^{M \cdot L \times N}$ along with the known measurement noise vector $\boldsymbol{w} = [\boldsymbol{w}_1^T, \boldsymbol{w}_2^T, \cdots, \boldsymbol{w}_L^T]^T$ of length $M \cdot L$.

The direct inversion of the linear model in Eq. (3.11) is generally not fea-

sible, since the resulting inverse problem is ill-conditioned and ill-posed, due to the whisker array consisting of only several whiskers and the moment being measured at only a limited number of views [52]. In the Bayesian stochastic framework, if both the unknown image $\boldsymbol{x} \sim \mathcal{N}(\boldsymbol{\mu}, \boldsymbol{\Pi})$ and the measurement noise $\boldsymbol{w} \sim \mathcal{N}(\boldsymbol{0}, \boldsymbol{R})$ are Gaussian, where $\mathcal{N}(\boldsymbol{m}, \boldsymbol{\Sigma})$ denotes the Gaussian distribution with mean $\boldsymbol{m}$ and covariance $\boldsymbol{\Sigma}$, then the MAP estimate $\hat{\boldsymbol{x}}_{MAP}$ is

$$\begin{aligned} \hat{\boldsymbol{x}}_{MAP} &= \arg\max_{\boldsymbol{x}} \ \log p(\boldsymbol{y}|\boldsymbol{x}) + \log p(\boldsymbol{x}) \\ &= \arg\min_{\boldsymbol{x}} \ ||\boldsymbol{y} - \boldsymbol{H}\boldsymbol{x}||^2_{\boldsymbol{R}^{-1}} + ||\boldsymbol{x} - \boldsymbol{\mu}||^2_{\boldsymbol{\Pi}^{-1}}, \end{aligned} \tag{3.12}$$

where $||\boldsymbol{z}||^2_{\boldsymbol{W}} = \boldsymbol{z}^T\boldsymbol{W}\boldsymbol{z}$ is the weighted residual norm with $\boldsymbol{W}$ positive definite. If the unknown image and the measurement noise have non-Gaussian distributions, then the estimate in Eq. (3.12) becomes the linear minimum mean square error (LMMSE) estimate, which minimizes $\mathbb{E}[||\boldsymbol{x} - \hat{\boldsymbol{x}}||_2^2]$, where $\mathbb{E}[.]$ is the statistical expectation operator [56]. Taking $\boldsymbol{\mu} = \boldsymbol{0}$, the all-zero vector, $\boldsymbol{R} = \lambda\boldsymbol{I}$, the λ-scaled identity matrix, and $\Pi = (\boldsymbol{D}^T\boldsymbol{D})^{-1}$ with $\boldsymbol{D}$ full column rank, the Eq. (3.12) yields the Tikhonov-regularized estimate

$$\hat{\boldsymbol{x}} = \arg\min_{\boldsymbol{x}} ||\boldsymbol{y} - \boldsymbol{H}\boldsymbol{x}||_2^2 + \lambda||\boldsymbol{D}\boldsymbol{x}||_2^2, \tag{3.13}$$

where the quadratic penalty term refers to the prior knowledge about the unknown fluid-flow field $\boldsymbol{x}$ [57, 58]. Using the fact that the fluid-flow velocity field should be fairly smooth except for the cases such as vortex boundaries, the regularization matrix is selected as $\boldsymbol{D} = (\boldsymbol{D}_x^T, \boldsymbol{D}_y^T)^T$ with $\boldsymbol{D}_x$ and $\boldsymbol{D}_y$ being the first-order difference approximations to the spatial derivative operators in the horizontal and vertical directions to impose a specified degree of spatial

smoothness, and the regularization parameter λ is used to control the tradeoff between the data fidelity and the amount of smoothness. On the other hand, the Tikhonov-regularized solutions are globally smooth, meaning that the detailed information such as sharp edges are also penalized while suppressing the background noise. Alternatively, other techniques such as the total variation [59] or the maximum entropy regularization [60] may be used to preserve the large gradients in the reconstructed images.

3.4 Dynamic Tactile Fluid-Flow Tomography

The stationary image formation model assumes that the unknown physical field is static during data acquisition. However, this assumption fails when reconstructing an image field in a dynamically changing environment, where significant changes occur over the data acquisition period, causing severe image artifacts in static reconstructions. In such a more general dynamic tomography problem, the unknown physical field may be modeled as a discrete-time hidden Markov random process based on the recursive estimation of the unknown random field through the measurements [26, 27].

In general, the state sequence $\{\boldsymbol{x}_i, i \in \mathbb{N}\}$ characterized by the state evolution function $\boldsymbol{f}_i : \mathbb{R}^{N\times K} \to \mathbb{R}^N$ is given by

$$\boldsymbol{x}_{i+1} = \boldsymbol{f}_i(\boldsymbol{x}_i, \boldsymbol{u}_i) \tag{3.14}$$

$$\boldsymbol{y}_i = \boldsymbol{h}_i(\boldsymbol{x}_i, \boldsymbol{w}_i), \tag{3.15}$$

where the random process $(\boldsymbol{u}_i, i \in \mathbb{N})$ accounts for the state noise, and N and K denote the dimensions of the state and process noise vectors, respectively.

The forward model function $\boldsymbol{h}_i : \mathbb{R}^{N\times I} \to \mathbb{R}^M$ relates the measurements $(\boldsymbol{y}_i, i \in \mathbb{N})$ to the unknown state $\boldsymbol{x}_i$, the random process $(\boldsymbol{w}_i, i \in \mathbb{N})$ is the measurement noise sequence, and I and M denote the dimensions of the measurement and measurement noise vectors, respectively.

If the state transition function $\boldsymbol{f}_i(\boldsymbol{x}_i, \boldsymbol{u}_i)$ and the forward model function $\boldsymbol{h}_i(\boldsymbol{x}_i, \boldsymbol{w}_i)$ are linear functions of $(\boldsymbol{x}_i, \boldsymbol{u}_i)$ and $(\boldsymbol{x}_i, \boldsymbol{w}_i)$, respectively, then Eqs. (3.14) and (3.15) can be reformulated under the linear state-space model as

$$\boldsymbol{x}_{i+1} = \boldsymbol{F}_i \boldsymbol{x}_i + \boldsymbol{u}_i \tag{3.16}$$

$$\boldsymbol{y}_i = \boldsymbol{H}_i \boldsymbol{x}_i + \boldsymbol{w}_i, \tag{3.17}$$

where $\boldsymbol{F}_i$ is the known state-transition matrix that characterizes the linear state evolution and the known matrix $\boldsymbol{H}_i$ is the linear measurement operator.

The state and measurement noise processes $\boldsymbol{u}_i$ and $\boldsymbol{w}_i$ are assumed to be zero-mean, mutually uncorrelated with possibly time-varying, known covariances $\boldsymbol{Q}_i$ and $\boldsymbol{R}_i$, respectively:

$$\mathbb{E}\begin{bmatrix}\boldsymbol{u}_i \\ \boldsymbol{w}_i\end{bmatrix}\begin{bmatrix}\boldsymbol{u}_i^T & \boldsymbol{w}_i^T & 1\end{bmatrix} = \begin{bmatrix}\boldsymbol{Q}_i\delta_{ij} & 0 & 0 \\ 0 & \boldsymbol{R}_i\delta_{ij} & 0\end{bmatrix}, \tag{3.18}$$

where δ_{ij} is the Kronecker delta function [61].

The Kalman filter is the linear minimum mean squared error (LMMSE) estimation procedure, in which the LMMSE estimates $\hat{\boldsymbol{x}}_{i|j}$ at time index i given the measurements $\boldsymbol{y}_{1:j}$ are computed under the linear state-space model. The KF error covariance is denoted

$$\boldsymbol{P}_{i|j} = \mathbb{E}[(\boldsymbol{x}_i - \hat{\boldsymbol{x}}_{i|j})(\boldsymbol{x}_i - \hat{\boldsymbol{x}}_{i|j})^T]. \tag{3.19}$$

The prior knowledge of the initial state $\boldsymbol{\mu}_1 = \mathbb{E}[\boldsymbol{x}_1]$ and the error covariance $\boldsymbol{\Pi}_1 = \mathbb{E}[(\boldsymbol{x}_1 - \boldsymbol{\mu}_1)(\boldsymbol{x}_1 - \boldsymbol{\mu}_1)^T]$, which is uncorrelated with the state and measurement noise is required for the KF procedure. Given the initial priors $\boldsymbol{P}_{1|0} = \boldsymbol{\Pi}_1$ and $\hat{\boldsymbol{x}}_{1|0} = \boldsymbol{\mu}_1$, the two recursive steps for the KF procedure are as follows:

Measurement update: The filtered estimate, $\hat{\boldsymbol{x}}_{i|i}$ $(j = i)$ at the time index i is computed by correcting the one-step prediction of the state, $\hat{\boldsymbol{x}}_{i|i-1}$ $(j = i-1)$ to incorporate information from the measurement $\boldsymbol{y}_i$ in the Bayesian sense:

$$\boldsymbol{K}_i = \boldsymbol{P}_{i|i-1}\boldsymbol{H}_i^T(\boldsymbol{H}_i\boldsymbol{P}_{i|i-1}\boldsymbol{H}_i^T + \boldsymbol{R}_i)^{-1} \tag{3.20}$$

$$\hat{\boldsymbol{x}}_{i|i} = \hat{\boldsymbol{x}}_{i|i-1} + \boldsymbol{K}_i(\boldsymbol{y}_i - \boldsymbol{H}_i\hat{\boldsymbol{x}}_{i|i-1}) \tag{3.21}$$

$$\boldsymbol{P}_{i|i} = \boldsymbol{P}_{i|i-1} - \boldsymbol{K}_i\boldsymbol{H}_i\boldsymbol{P}_{i|i-1}, \tag{3.22}$$

where $\boldsymbol{K}_i$ is the Kalman gain.

The LMMSE estimate $\hat{\boldsymbol{x}}_{i|i}$ can also be expressed as the solution to the quadratic optimization problem [56, 61]

$$\hat{\boldsymbol{x}}_{i|i} = \arg\min_{\boldsymbol{x}_i} ||\boldsymbol{y}_i - \boldsymbol{H}_i\boldsymbol{x}_i||^2_{\boldsymbol{R}_i^{-1}} + ||\boldsymbol{x}_i - \hat{\boldsymbol{x}}_{i|i-1}||^2_{\boldsymbol{P}^{-1}_{i|i-1}}, \tag{3.23}$$

where the first term represents the match with the measurements weighted by the measurement uncertainty $\boldsymbol{R}_i$ and the second term is the prior estimate weighted by the prior uncertainty $\boldsymbol{P}_{i|i-1}$. Therefore, The LMMSE estimate $\hat{\boldsymbol{x}}_{i|i}$ shows a tradeoff between the two terms.

Time update: The one-step prediction $\hat{\boldsymbol{x}}_{i+1|i}$ is computed from the state transition model and the LMMSE estimate $\hat{\boldsymbol{x}}_{i|i}$ to obtain the prior information

needed for the next measurement update at the time index $i+1$:

$$\hat{\boldsymbol{x}}_{i+1|i} = \boldsymbol{F}_i \hat{\boldsymbol{x}}_{i|i} \tag{3.24}$$

$$\boldsymbol{P}_{i+1|i} = \boldsymbol{F}_i \boldsymbol{P}_{i|i} \boldsymbol{F}_i^T + \boldsymbol{Q}_i. \tag{3.25}$$

CHAPTER 4

Static Tactile Fluid-Flow Tomography with a Robotic Whisker Array

In-air and underwater flow experiments were performed to validate the proposed model for the static tactile fluid-flow tomographic imaging with a whisker array. The chapter begins with investigating the assumption of proportionality between the fluid-flow velocity-squared and the drag force on a whisker segment for in-air and underwater flow experiments in Section 4.1. Next, the detailed information about the whisker array construction is given in Section 4.2. The experimental setup and the calibration process for air-flow imaging are then explained in Section 4.3. The air-flow imaging results for different flow shapes generated using a hair dryer are presented in Section 4.4. The chapter concludes with the description of the underwater experimental setup, and the static tactile fluid-flow tomographic imaging results for the underwater experiments in Section 4.5.

4.1 The Validity of the $f_D \propto V^2$ Assumption

All the experiments were performed at the temperature of 25 °C for both in-air and underwater flow imaging. The density and dynamic viscosity values for

air and water at 25 °C are [24]

$$\rho_{air} = 1.184\,\mathrm{kg/m^3}, \qquad \mu_{air} = 18.6 \times 10^{-6}\,\mathrm{Pa.s}$$
$$\rho_{water} = 997.05\,\mathrm{kg/m^3}, \qquad \mu_{water} = 8.9 \times 10^{-4}\,\mathrm{Pa.s}.$$

The diameter of each whisker used in the experiments was $d = 3$ mm, which also yields the characteristic length of a whisker ($L = d$), as explained in Section 3.1. As a result, the Reynolds numbers for air and water at 25 °C are calculated to be

$$Re_{air} \approx 191V \quad \text{and} \quad Re_{water} \approx 3361V. \tag{4.1}$$

This implies that the assumption of proportionality between the drag force and the square of fluid-flow velocity is valid ($Re > 100$), when

$$V_{air} > 0.52 \text{ m/s} \quad \text{and} \quad V_{water} > 0.03 \text{ m/s}. \tag{4.2}$$

It can also be deduced that the air-flow velocity should be much larger than the water-flow velocity in order to achieve the same amount of drag force on a whisker segment in air and underwater at the given temperature:

$$V_{water}^2 \approx 1.2 \times 10^{-3} V_{air}^2 \quad \text{at } 25\,^{\circ}\mathrm{C}. \tag{4.3}$$

4.2 The Whisker Array

The whisker array used for the 2-D cross-sectional tactile imaging of the in-air and underwater flow patterns is shown in Figure 4.1. Each whisker is made

up of a superelastic Nitinol ($E \approx 8 \times 10^4$ MPa) wire covered with a plastic straw to increase the surface area exposed to the flow. The two strain gauges (7×4 mm) facing each other are superglued to the whisker at the whisker base installed 1.5 cm away from the center of rotation. The Nitinol wire is 0.5 mm in diameter and 15.2 cm in length and the plastic straw with 3 mm in diameter and 11 cm in length is superglued onto the Nitinol wire from the tip to the strain gauges, making the whisker more sensitive to small deflections including very small vibrations.

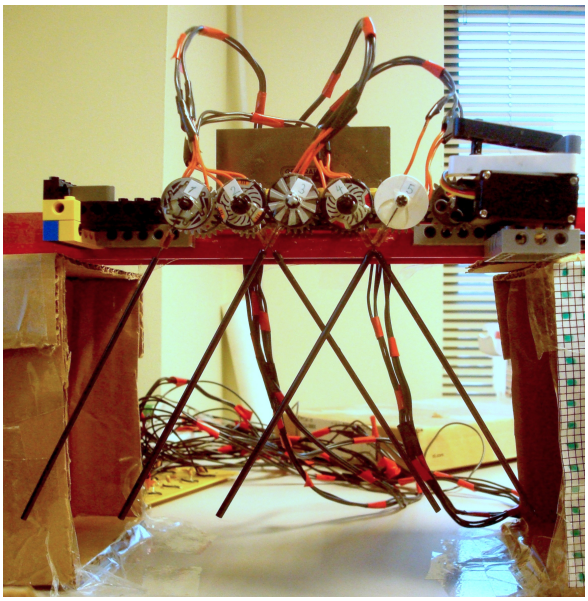

Figure 4.1: The array of five whiskers used for the 2-D cross-sectional tomographic imaging of the in-air and underwater flow: Each robotic whisker is made up of a superelastic Nitinol wire and covered with a plastic straw to increase the exposure to the flow.

The whiskers are attached onto the setup made up of LEGO parts superglued to a carpenter's level of length 24 inches (≈ 61 cm). The whiskers were separated by 2.42 cm from each other with three of them (the middle and the two outer whiskers) rotating in one direction and the other two in the opposite

direction. A protractor is affixed to the carpenter's level to read the viewing angle during measurements. A servomotor is also installed for uninterrupted data acquisition using LabVIEW.

4.3 The Calibration Process for Air-Flow Experiments

The calibration of a physical system is one of the most crucial steps in order to obtain accurate results from the physical measurements. In our case, each whisker in the whisker array needs to be calibrated individually, since the responses of each whisker to the exerted force differ from one another due to the factors during manufacturing and installation, such as the misalignment between the two facing strain gauges and the attachment of the plastic straws or strain gauges at slightly different distances from the whisker base.

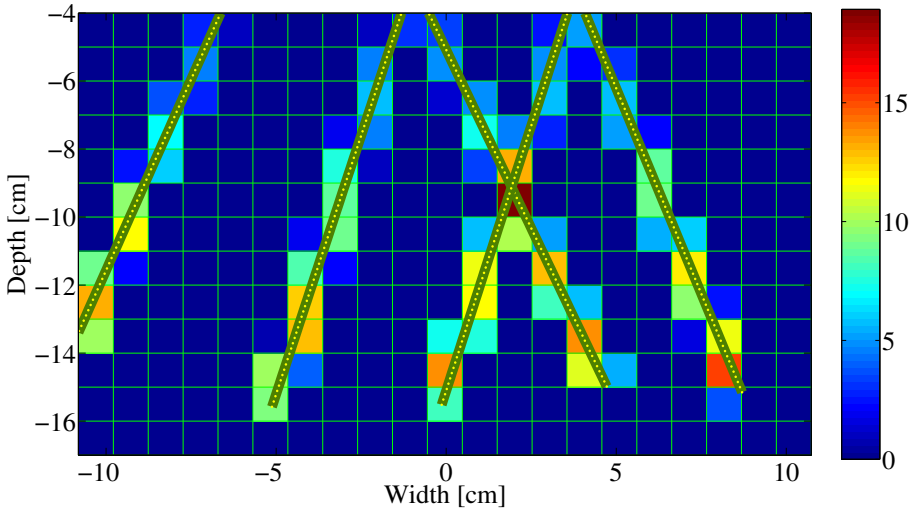

Figure 4.2: The field discretization: The pixel values correspond to the total contribution to the moment values measured at the base of whiskers in the whisker array.

The calibration process for the air-flow experiments begins with the dis-

cretization of the physical field to be reconstructed. Figure 4.2 illustrates the field discretization with a 13×21 pixel array for a given angular view. Each whisker was divided into 100 equally spaced segments along its length, and at most two pixels were assumed to contribute to the moment measured at the whisker at a particular whisker segment. The blocking loss due to the whiskers in the front line was also adjusted for the two whiskers in the back row, empirically. In Figure 4.2, each pixel displays the total contribution to the moment values measured at the whisker bases in the whisker array.

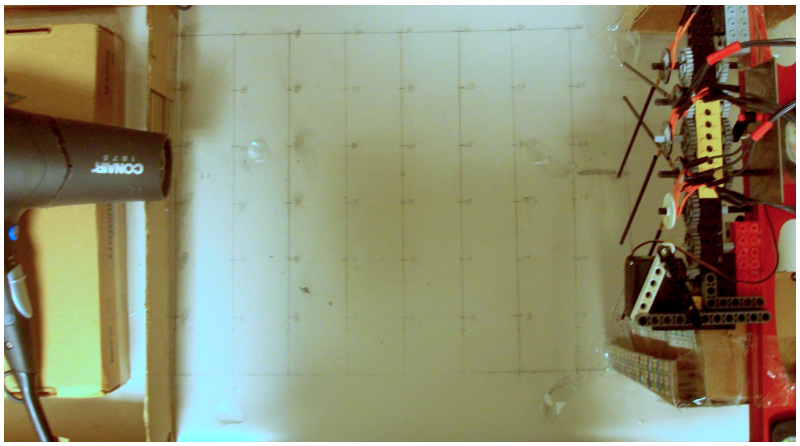

Figure 4.3: The setup for the air-flow imaging experiments.

Figure 4.4: The positioning of the the hair dryer to generate different air-flow patterns.

The experimental setup for the air-flow experiments is shown in Figure 4.3. A hair dryer that has cooling and two different speed options was used as an air-flow source. Different flow patterns were also generated by means of a hair dryer concentrator as shown in Figure 4.4.

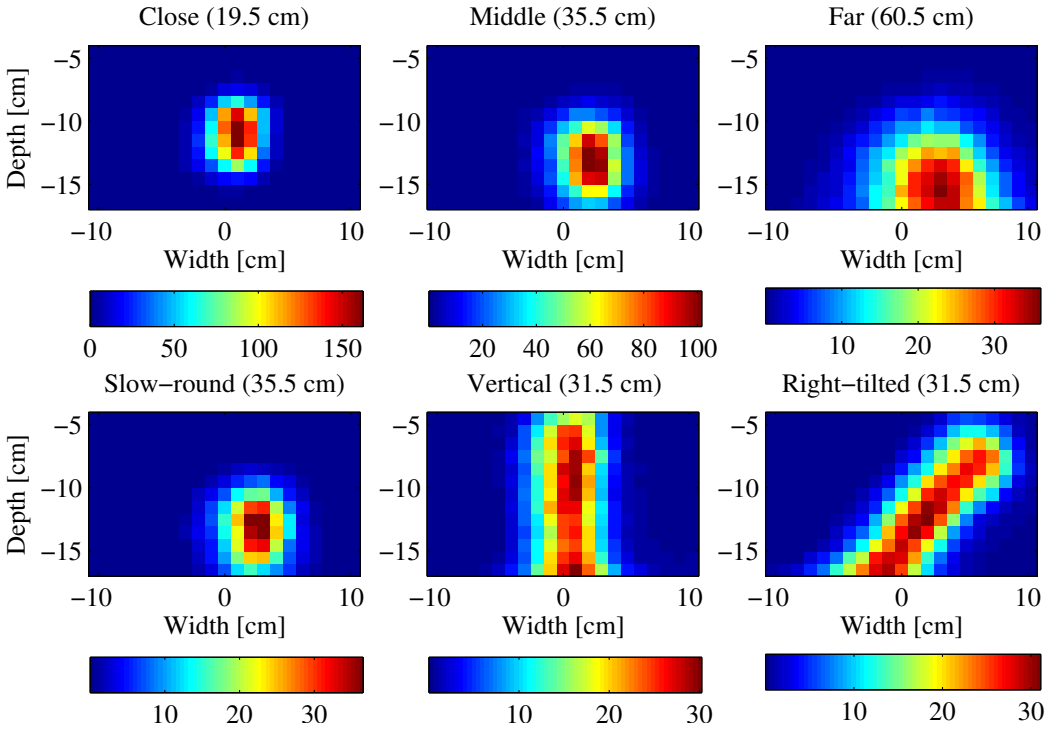

Figure 4.5: The six different air-flow patterns generated by using a hair dryer: The ground-truth images display the velocity squared distribution in the image field measured by means of a hot-wire anemometer.

The ground truth for the air velocity field was determined by moving a hot-wire anemometer along the same 13×21 grid used for discretization of the image field, in order to measure the air velocity right in front of the whisker array at $13 \times 21 = 273$ locations. Three trials were taken with the hot-wire anemometer for six different-shaped flow patterns generated by the hair dryer, and the average over these trials for each flow pattern was used as the ground-truth images shown in Figure 4.5.

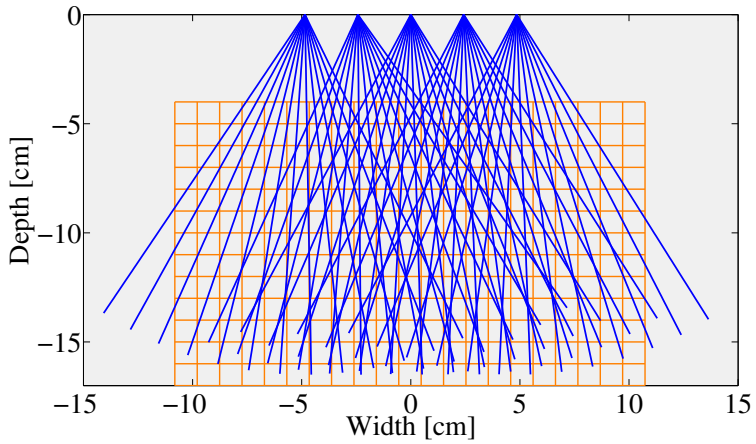

Figure 4.6: The imaging geometry for the air-flow imaging experiments: The 13×21 orange grid in the background corresponds to the discretized unknown image field to be reconstructed.

The imaging geometry for the air-flow experiments with the whisker array is illustrated in Figure 4.6. For each flow pattern, the whisker array was rotated by 5° normal to the direction of flow between the two successive views using the servomotor and the measurements were collected at 13 different angular views, which results in a total number of measurements, $M = 13 \times 5 = 65$, at each trial. All of the measured data was low-pass filtered at 160 Hz, sampled at 500 Hz and averaged over 10 seconds. The measurements were repeated five times for the same flow pattern, totaling $13 \times 5 \times 6 = 390$ measurements for each whisker in the whisker array.

In order to calibrate the physical measurements to the moment, the ground-truth images for the six different flow patterns were used to obtain the "simulated" moment measurements, $\boldsymbol{y}_{GT} = \boldsymbol{H}\boldsymbol{x}_{GT}$, for every single flow shape, where the measurement matrix $\boldsymbol{H}_{65\times 273}$ was generated using the same angular views from the experiments, and $\boldsymbol{x}_{GT}$ denotes the vector representation of the ground truth image for the corresponding flow pattern. Then, to account for any nonlinearity in the measurements, a polynomial fit was applied

to find the quadratic equation $y_M = \beta_1 y_V^2 + \beta_2 y_V + \beta_3$ for each individual whisker, which maps the measured voltage, y_V, to the normalized moment value, $y_M = M/(\frac{1}{2}\rho C_D d) = \int_0^L V^2(s)ds$.

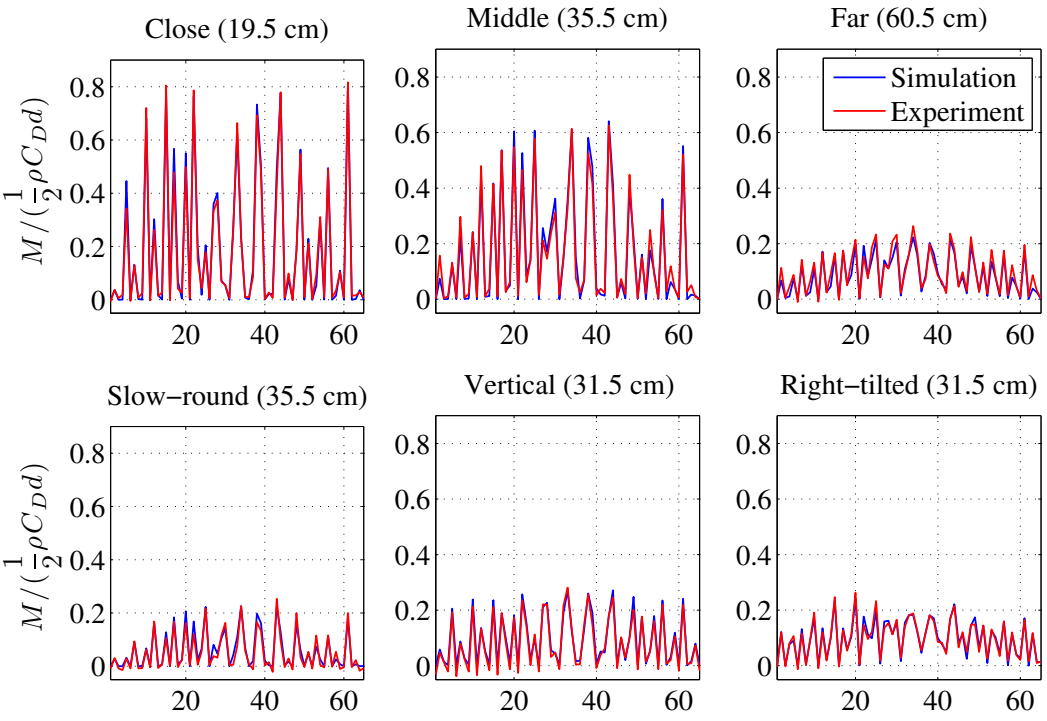

Figure 4.7: The agreement between the "simulated" and the actual measurements for the six different flow patterns generated by the hair dryer.

Figure 4.7 shows the agreement between the actual measurements averaged over five trials and the simulated moments for each flow pattern. In addition,Table 4.1 presents a quantitative comparison between the flow patterns in terms of the relative residual error, which is defined as $r = ||\boldsymbol{y}_{GT} - \boldsymbol{y}||_2 / ||\boldsymbol{y}_{GT}||_2$ with $\boldsymbol{y}$ denoting the physical measurements. The overall relative residual over the entire data set is calculated to be $r = 0.0794$, and the negative-valued physical measurements after the calibration process are within the noise level.

Table 4.1: A comparison of the relative residual between the six different flow patterns after calibration.

Flow pattern	$r = \frac{\|\|\boldsymbol{y}_{GT} - \boldsymbol{y}\|\|_2}{\|\|\boldsymbol{y}_{GT}\|\|_2}$
Close-round (19.5 cm)	0.0853
Mid-round (35.5 cm)	0.1208
Far-round (60.5 cm)	0.1984
Slow-round (35.5 cm)	0.2138
Vertical (31.5 cm)	0.1420
Right-tilted (31.5 cm)	0.1054

4.4 The Experimental Results for Tactile Air-Flow Imaging

Figures 4.8 and 4.9 show the results for the static tactile air-flow tomographic imaging using a whisker array for six different flow patterns. The first rows display the ground truth images for each air-flow shape, whereas the Tikhonov-regularized solutions using the simulated moments and the calibrated physical measurements are provided in the middle and bottom rows, respectively. Tables 4.2 and 4.3 show the relative error between the ground truth and the two reconstructed images.

The Tikhonov-regularized solution is given by

$$\hat{\boldsymbol{x}} = (\boldsymbol{H}^T\boldsymbol{H} + \lambda\boldsymbol{D}^T\boldsymbol{D})^{-1}\boldsymbol{H}^T\boldsymbol{y}, \tag{4.4}$$

where the regularization parameter, λ, for the reconstructions was chosen by trial and error to obtain the best possible estimate. There exist, however, techniques such as cross-validation to specify λ based on the available measurements [62, 63].

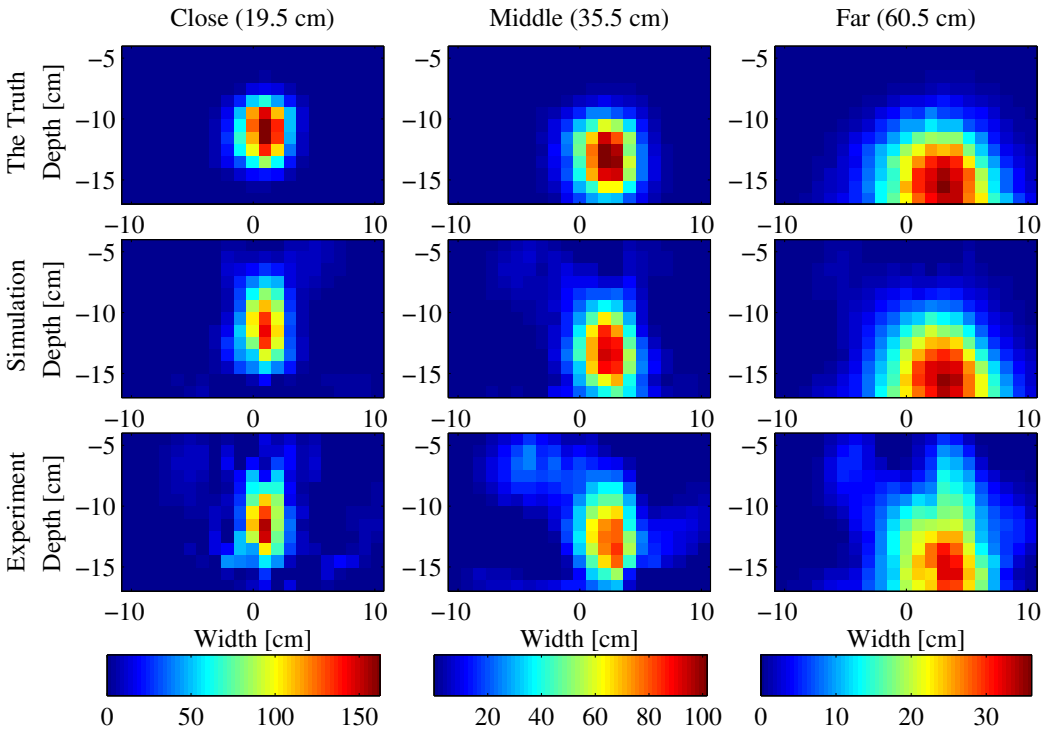

Figure 4.8: The 13×21 velocity-squared static images of the round-shaped air-flow generated by the hair dryer positioned at three different distances from the whisker array: Top row: The ground truth images measured via a hot-wire anemometer, middle row: the Tikhonov-regularized images using the simulated moment data, bottom row: the Tikhonov-regularized images using the calibrated physical measurements.

Table 4.2: The relative error results for the round-shaped air-flow generated by the hair dryer positioned at three different distances from the whisker array shown in Figure 4.8.

Description	Close-round	Mid-round	Far-round
Simulation vs. Truth	0.2905	0.1912	0.0758
Experiment vs. Truth	0.3726	0.4423	0.3237
Experiment vs. Simulation	0.2825	0.3739	0.2929

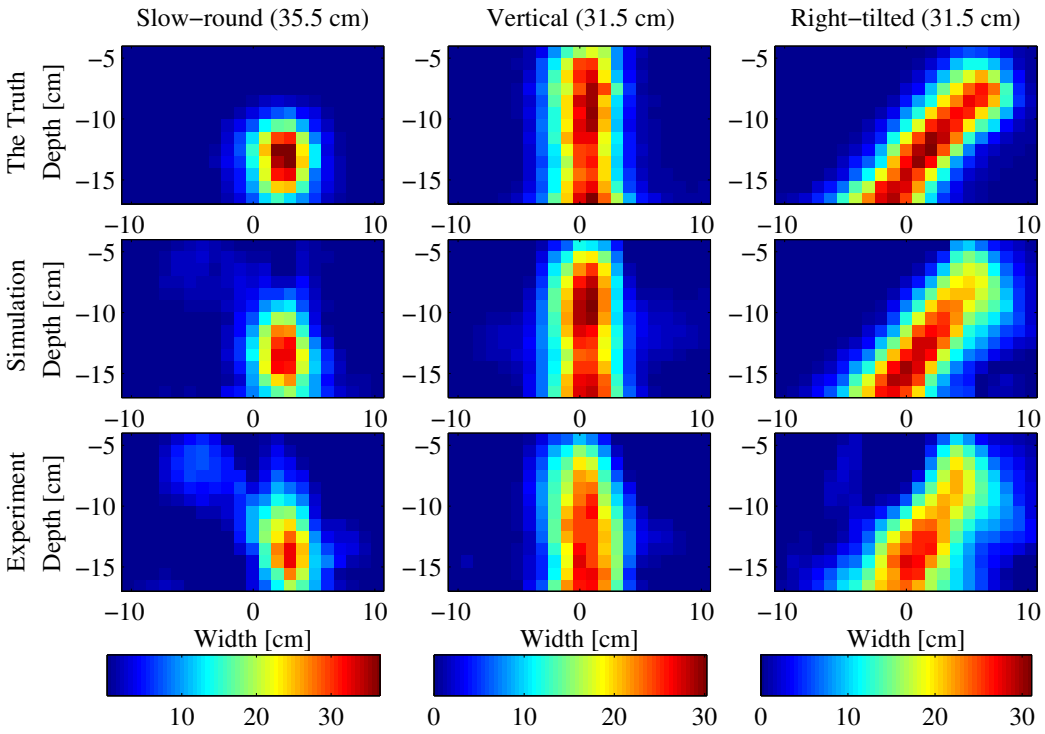

Figure 4.9: The 13×21 velocity-squared static images of the three different air-flow patterns generated by the hair dryer: Top row: The ground truth images measured via a hot-wire anemometer, middle row: the Tikhonov-regularized images using the simulated moment data, bottom row: the Tikhonov-regularized images using the calibrated physical measurements.

Table 4.3: The relative error results for the three different air-flow patterns generated by the hair dryer shown in Figure 4.9.

Description	Slow-round	Vertical	Right-tilted
Simulation vs. Truth	0.2078	0.1515	0.1725
Experiment vs. Truth	0.4260	0.3179	0.3174
Experiment vs. Simulation	0.3302	0.2637	0.2232

The regularization parameter was set to be $\lambda_{sim} = 1 \times 10^{-16}$ for the simulations, whereas $\lambda_{close} = 4 \times 10^{-12}$ and $\lambda_{mid} = 4 \times 10^{-11}$ were chosen for the close-round and mid-round flow patterns, respectively, and $\lambda = 2 \times 10^{-10}$ for the image reconstruction of the remaining flow shapes with the experimental

data. Knowing the fact that the ground truth images do not have any negative velocity components, the negative-valued pixels produced by the Tikhonov regularization were simply zeroed after reconstructions for the air-flow imaging case.

The resulting images show that the Tikhonov regularization produces stable minimum-norm least-squares solutions for the undetermined system as there are fewer measurements than the number of pixels ($M < N$). The effect of global smoothness can be clearly seen in the images reconstructed using both the simulated and experimental data. However, it is more evident in the experimental case as the background noise is suppressed at the cost of losing more edge information, further increasing the relative error when compared with the simulations.

There are several complications in reconstructing the unknown image field as a result of using a sparse and non-uniform sampling scheme with geometrical constraints. For instance, the stretching effect on the reconstructed round-shaped flow patterns in the vertical direction is clearly noticeable, resulted from the difference between the horizontal and vertical resolution. In addition, sparse sampling near image boundaries causes a smearing effect as observed in the reconstructed images for the right-tilted flow pattern close to the top-right corner. Therefore, a careful analysis of the spatial resolution of the Tikhonov-regularized solution given by Eq. (4.4) is required to investigate such implications originating from sparse and nonuniform sampling.

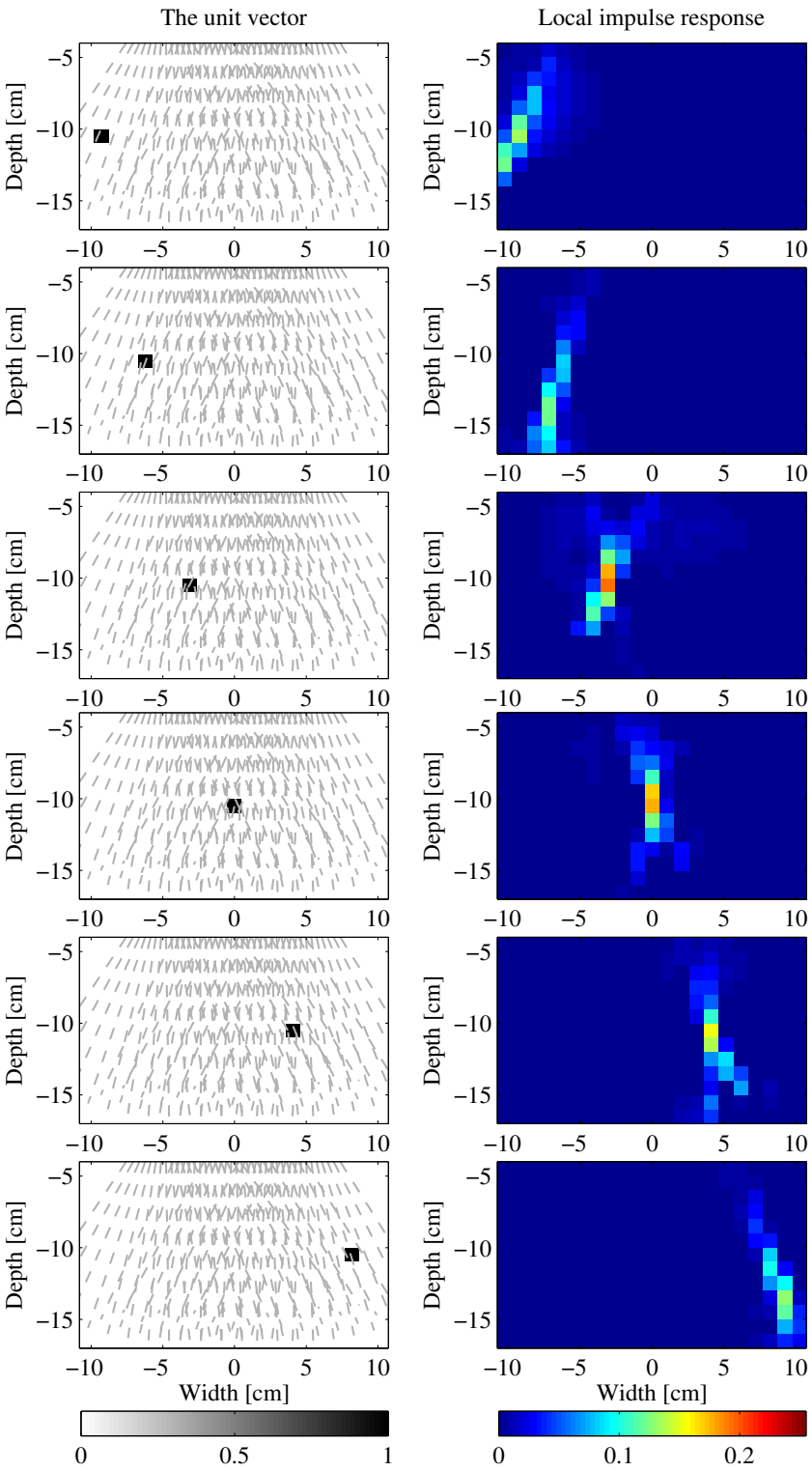

Figure 4.10: The local impulse responses for the pixel locations along the 7th row of the pixel array with the choice of $\lambda = 2 \times 10^{-10}$: The dashed lines in the unit vector images correspond to the whisker paths used for the static reconstruction.

An effective way to examine the spatial resolution is to analyze the local impulse response of a particular pixel, which is given by [31, 64]

$$\boldsymbol{l}^j = (\boldsymbol{H}^T\boldsymbol{H} + \lambda\boldsymbol{D}^T\boldsymbol{D})^{-1}\boldsymbol{H}^T\boldsymbol{e}^j, \tag{4.5}$$

where $\boldsymbol{l}^j$ is the local impulse response for the jth parameter of the Tikhonov-regularized estimate in Eq. (4.4) computed using the unit vector $\boldsymbol{e}^j$ of length N with $\boldsymbol{e}^j[n] = 1$ if $j = n$ and 0 otherwise. The local impulse response provides a quantification of the alteration on the Tikhonov-regularized estimate caused by a perturbation at a given pixel location [64].

Figure 4.10 shows the local impulse responses for the six distinct pixel locations along the 7th row of the pixel array with the choice of $\lambda = 2 \times 10^{-10}$ after zeroing all the negative-valued pixels. The spatial resolution in the horizontal direction gets better toward the image center with the increasing number of whisker paths passing through a pixel. Furthermore, as a result of the pixels near the left and right ends of the pixel array being swept by a whisker only once or twice, a smearing effect occurs along the corresponding whisker paths, lowering the spatial resolution considerably, which can also be seen in the case of the reconstructed right-tilted flow pattern images near the top-right end.

The three local impulses for the pixels located along the mid-column of the pixel array are shown in Figure 4.11 to examine the change in the spatial resolution along the vertical direction. It is noticeable that the spatial resolution is slightly better for the pixels farther from the whisker base, which is solely a consequence of the weighting of the line integrals with respect to the distance from the whisker base, relatively attenuating the local impulse responses of

the pixels located near the whisker base.

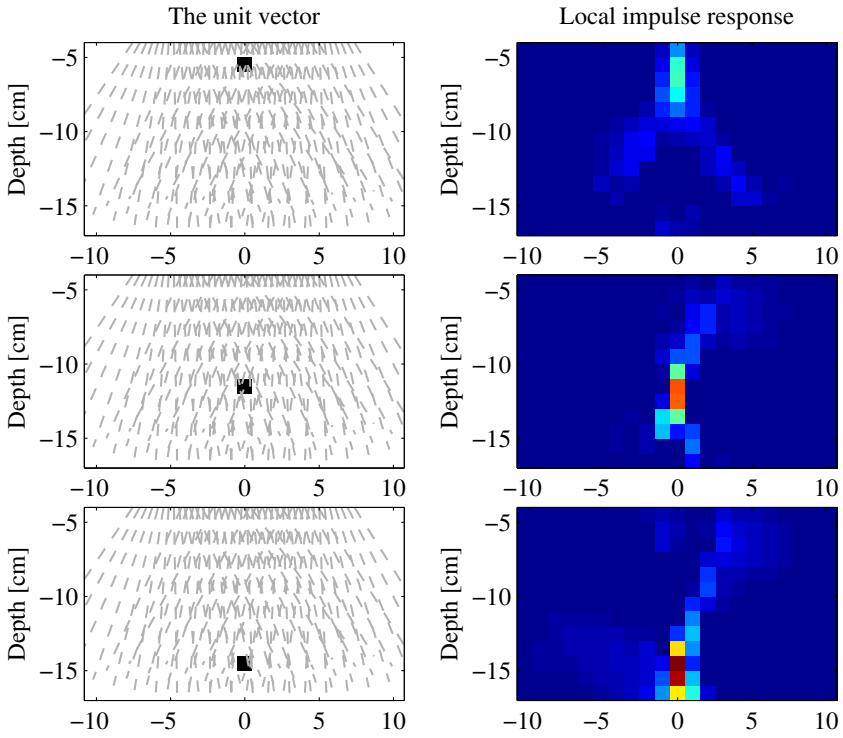

Figure 4.11: The local impulse responses for the pixel locations along the 11th column of the pixel array with the choice of $\lambda = 2 \times 10^{-10}$: The dashed lines in the unit-vector images correspond to the whisker paths used for the static reconstruction.

The geometrical constraints on the whisker array-configuration give rise to different spatial resolution properties in the vertical and horizontal directions. The whisker array is attached to a horizontally fixed carpenter's level, which restricts the rotation of each whisker to only around its base, resulting in the whisker paths being positioned over a limited angular range. This produces local impulse responses stretching over the vertical direction, since there are no such whisker paths originating from the left or right ends in the opposite direction in contrast with conventional tomography. This vertical-stretching effect is also evidently apparent in the resulting images for the round-shaped

flow patterns positioned at several distances from the whisker array, as they can also be viewed as point-like flow sources.

There are also several physical factors affecting the performance of the tomographic fluid-flow imaging algorithm presented here. In building the artificial whiskers, the use of thinner and more flexible materials such as plastic strips was not preferred because this design would allow very large-angle deflections, generating extreme departures for the whiskers from their initial straight paths, which would become an undesirable situation for the proposed method. Instead, metal whiskers covered with plastic straws with relatively larger diameters were used to somewhat limit the amount of bending while increasing the surface area normal to the flow. On the other hand, this may also introduce some heterogeneity and nonuniformity in the whisker composition due to each plastic straw being superglued to the Nitinol wire at a distance from the whisker base, resulting in variable stiffness characteristics along the length of the whisker. Nevertheless, no significant effect was observed on the tomographic image reconstructions. Moreover, any angular deviation from the presumed positions of the whiskers at an angular view due to practical reasons such as loose fixation at the whisker base or imprecise rotation of the whisker array would introduce additional inaccuracies as there may not be enough whisker paths to compensate for such angular errors. However, the imaging results indicate that the angular spacing of 5° between two consecutive views was a reasonable choice for static reconstructions to mitigate such issues related to using a sparse sampling scheme.

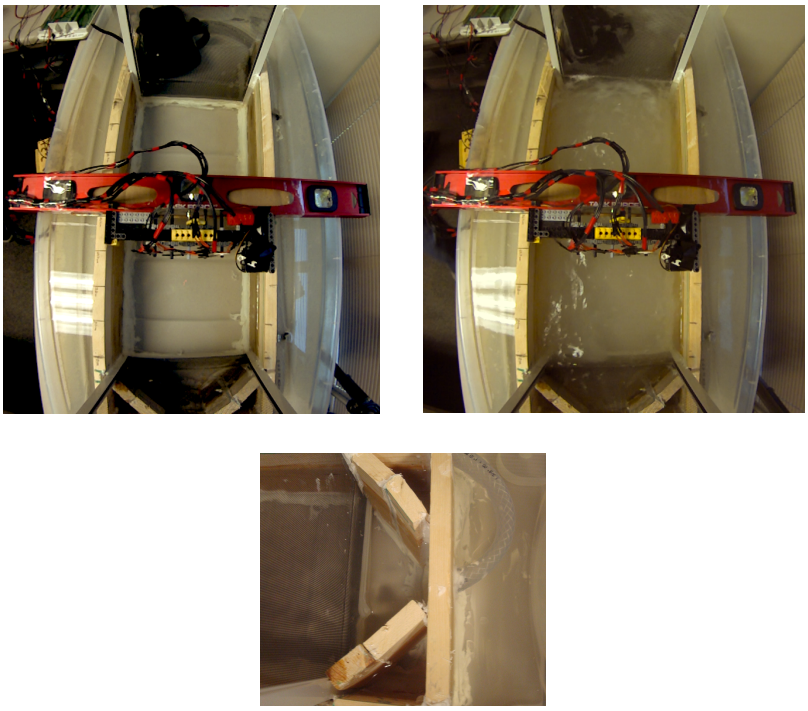

Figure 4.12: The setup for the underwater flow-imaging experiments: An adjustable water pump with a flow rate up to 1300 gallons/hour was used to generate a flow at different speeds inside the container restricted by the wooden walls installed for a narrow open channel. The two screens on both ends help create a circulating flow pattern. The water pump connects with the channel through a hose with its exit on the opposite site to make it easier for the water pump to suck up the incoming flow and pump it back immediately.

4.5 The Experimental Results for Tactile Underwater Flow Imaging

The setup for the underwater experiments was shown in Figure 4.12. A water pump with an adjustable flow rate up to 1300 gallons/hour was used to generate a water-flow in a storage container ($113.5 \times 50.5 \times 16$ cm). The open channel was bounded by wooden walls of length 75 cm and partially blocked by the two screens of width 24.5 cm. The water pump and the channel were connected through a hose with a diameter of 1 inch on the opposite end of

the container to in order to facilitate the sucking of the incoming flow back by the pump. The flow exiting from the hose was directed toward the left of the water pump to generate a continuous flow circulation along the channel with the help of the two screens located at both ends.

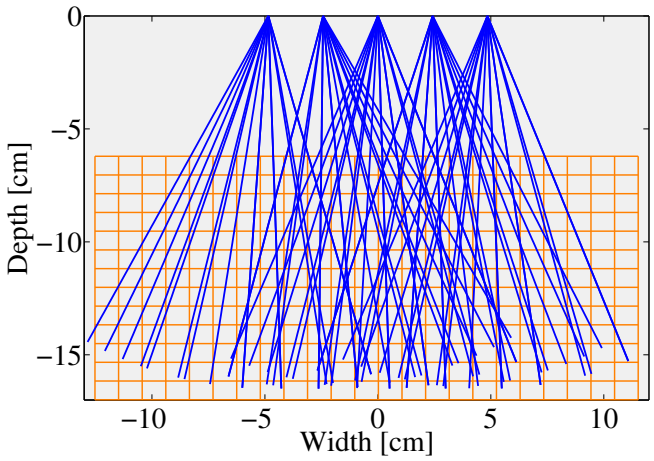

Figure 4.13: The imaging geometry for the underwater flow imaging experiments: The 11×23 orange grid in the background corresponds to the discretized unknown image field to be reconstructed.

The imaging geometry for the underwater flow experiments was shown in Figure 4.13. Due to the restriction from the boundary walls, the whisker array was able to rotate in an angular range smaller than in air-flow-imaging experiments, which was compensated by collecting the data twice for eight views slightly differing between the two data sets, as the flow strength complicates the servomotor rotation. Therefore, the measured data was averaged over 0.5 seconds at each angular view, resulting in a total number of $N = 5 \times 16 = 80$ measurements collected to reconstruct the Tikhonov-regularized 11×23 images using the measurement matrix $\boldsymbol{H}_{80\times 253}$ for each cross-sectional flow section.

Figures 4.14 - 4.16 show the static tactile flow imaging results at eight different locations as the whisker array moves further away from the hose exit

and gets closer to the water pump along the channel length. Each resulting Tikhonov-regularized image represents the 2-D cross-sectional mean velocity-squared distribution at a particular location corresponding to the flow pattern generated by the water pump at a given flow rate. The regularization parameters were manually chosen as $\lambda_1 = 4 \times 10^{-9}$, $\lambda_2 = 2 \times 10^{-9}$ and $\lambda_3 = 1 \times 10^{-9}$ for the three different flows changing from laminar to turbulent, respectively.

In all three cases, the circulating flow can be described as a positive flow starting with just about the shape of the hose distorted by the screen between the whisker array and the hose exit along with the additional incoming circulating flow from the right side of the channel, and then directing toward the left wooden wall with its strength gradually decreasing after hitting the wall as the whisker array moves closer to the water pump, and a negative flow in the reverse direction, being reflected back from the screen near the water pump, hitting the right wall and diminishing as it begins to circulate toward the screen located before the hose exit, resulting in a near-zero net fluid-flow velocity along the mid-channel and around the hose exit. In the first two cases when the flow can be considered to be laminar, the negative flow is much weaker than the positive flow as the water pump is able to suck the incoming flow almost entirely, since the flow velocity is very low. In comparison, the negative flow in Figure 4.16 is as strong as the positive flow until the mid-length of the channel for the circulating turbulent flow generated by the water pump at a flow rate of 1300 gallons/hour, as most of the turbulent flow gets reflected from the screen due to its high flow-velocity.

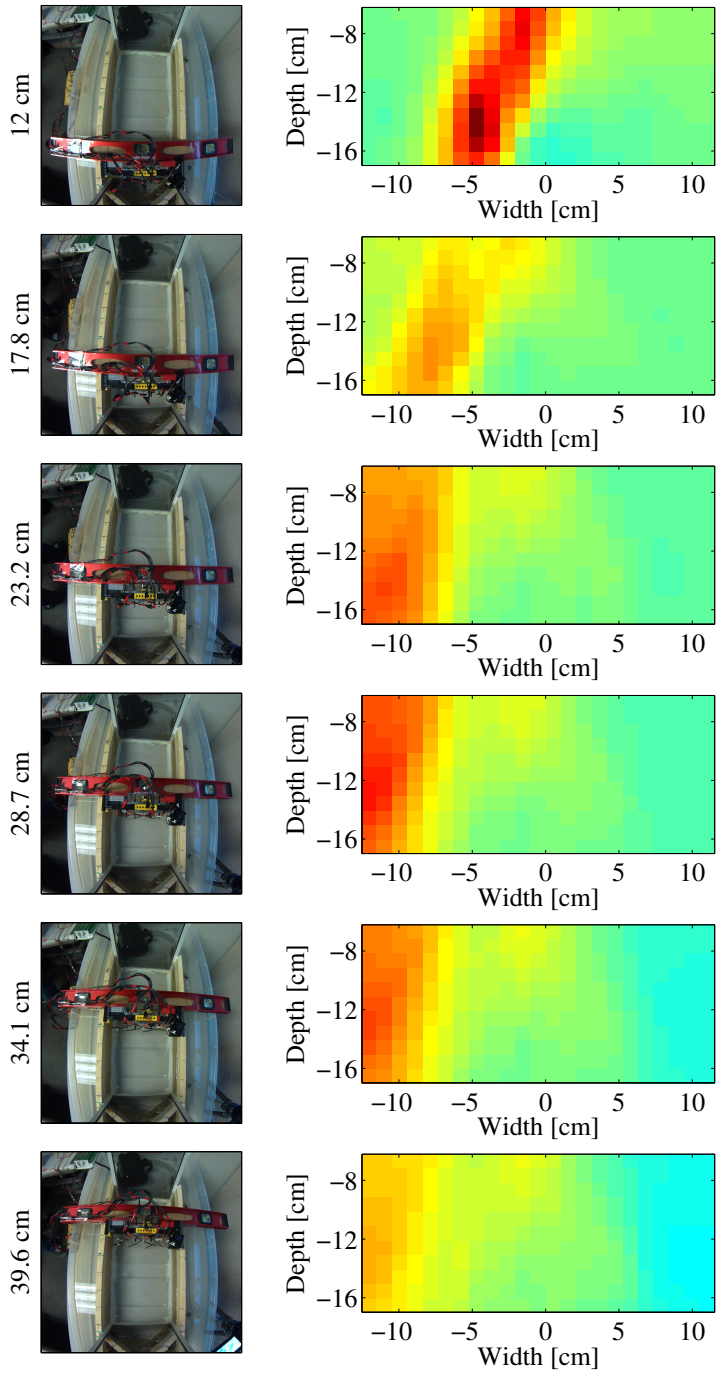

Figure 4.14: The 11×23 static velocity-squared images of the cross-sectional laminar circulating water-flow pattern: As the whisker array moves further away from the hose exit, the positive flow directs toward the left wooden wall weakening near the other end, and it gets sucked up back almost entirely by the water pump resulting in a very weak negative flow reflected from the screen on the other end.

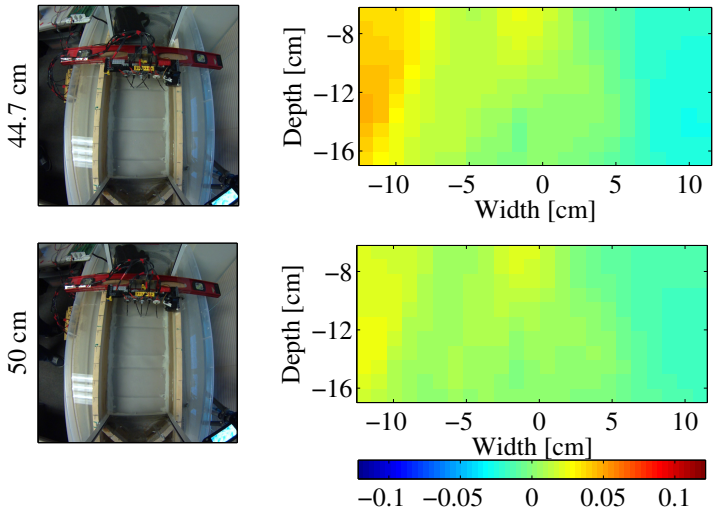

Figure 4.14 (cont.).

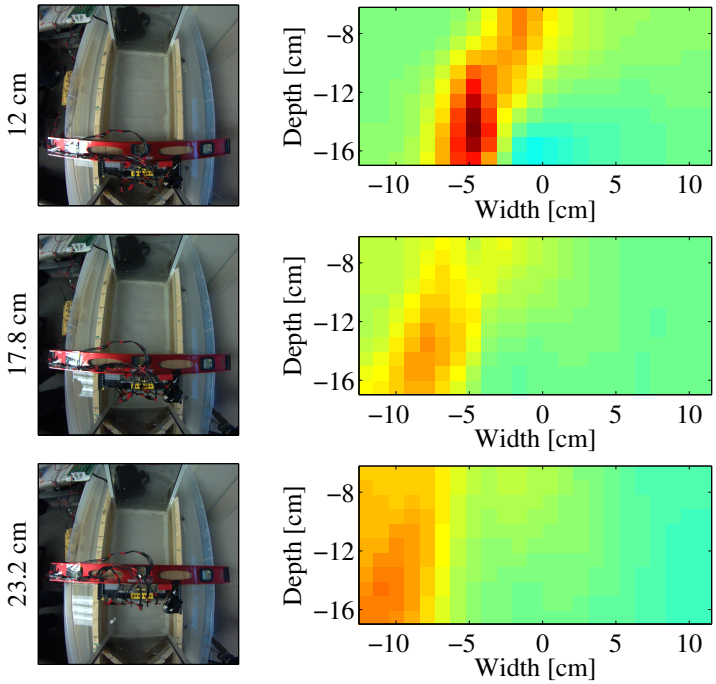

Figure 4.15: The 11×23 static velocity-squared images of the cross-sectional near-laminar circulating water-flow pattern relatively stronger than the laminar water-flow displayed in Figure 4.14: As the whisker array moves further away from the hose exit, the positive flow directs toward the left wooden wall and gets weakened near the other end, whereas the negative flow reflected from the screen on the other end is slightly more visible when compared with the laminar flow shown in Figure 4.14, since the positive flow does not get fully sucked up by the water pump.

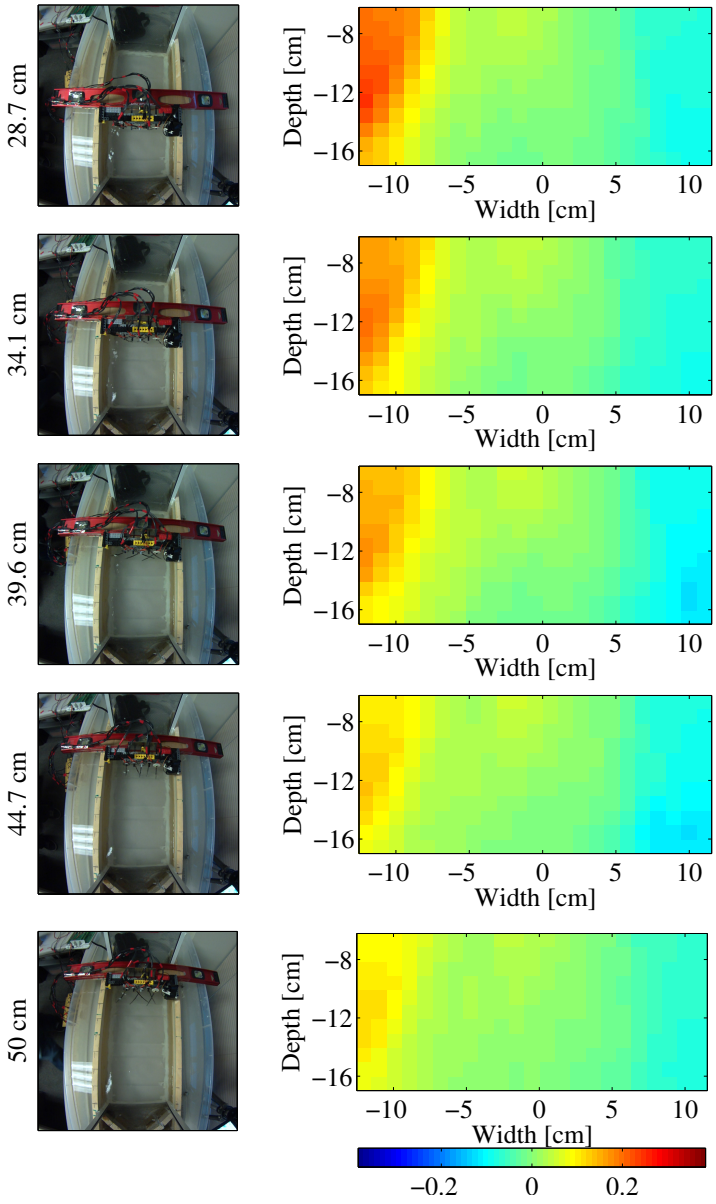

Figure 4.15 (cont.).

In order to make a quantitative analysis, the relative residual error results are given in Table 4.4, since there was no ground truth available. The relative residual error is defined as the agreement between the physical moment

measurements and the resulting moment estimates given by the formulation

$$\boldsymbol{r} = \frac{||\boldsymbol{y} - \boldsymbol{H}\hat{\boldsymbol{x}}||_2}{||\boldsymbol{y}||_2}. \tag{4.6}$$

Table 4.4: The relative residuals for the cross-sectional static water-flow velocity generated by the water pump at different velocities shown in Figure 4.17.

Distance	Flow 1	Flow 2	Flow 3
12 cm	0.5589	0.4495	0.4816
17.8 cm	0.5226	0.4070	0.2659
23.2 cm	0.3979	0.2678	0.2265
28.7 cm	0.3716	0.2489	0.2591
34.1 cm	0.3746	0.2814	0.2944
39.6 cm	0.4309	0.2882	0.3537
44.7 cm	0.5154	0.3517	0.3169
50 cm	0.6501	0.3617	0.3069

The relative residual error increases with the larger amount of smoothness. One should expect a larger mismatch between the measured data and the reconstructed images, since the physical field may not be sufficiently static, violating the stationarity assumption, due to the data being collected over a long period of time. This can be observed in the reconstructions at the first measurement position, which is 12 cm away from the hose exit and located right after the screen.

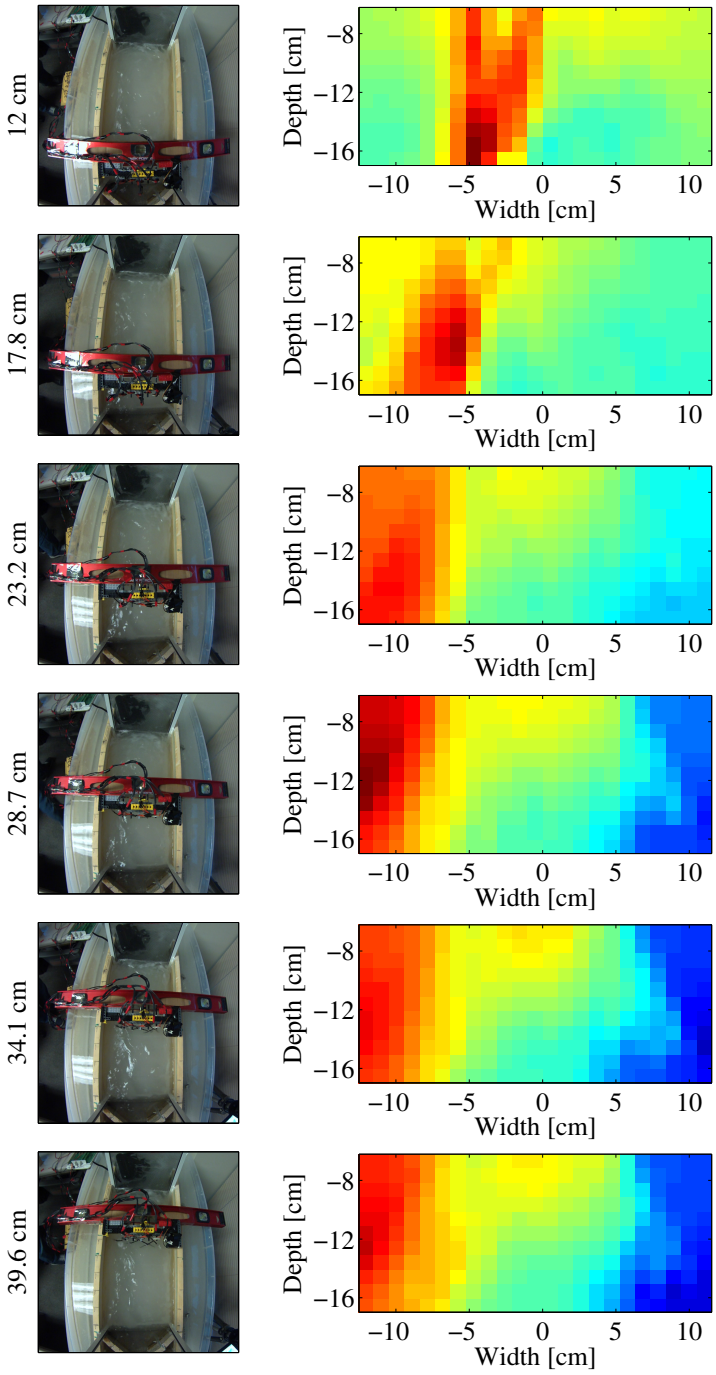

Figure 4.16: The 11×23 static velocity-squared images of the cross-sectional turbulent circulating water-flow pattern: As the whisker array moves further away from the hose exit, the positive flow directs toward the left wooden wall, but does not gets weakened significantly, since the flow rate is much higher than the first two circulating flow-patterns shown in Figures 4.15 and 4.16, resulting in the water pump not being able to suck up most of the incoming flow, which leads to a negative flow almost as strong as the positive flow except for the region near the hose exit.

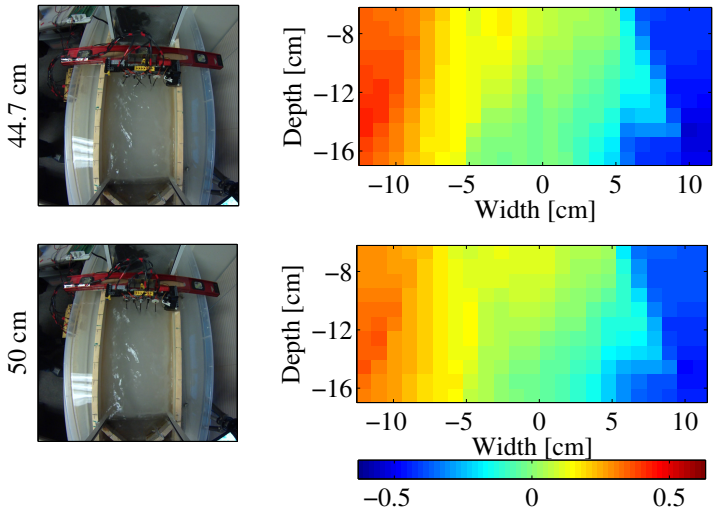

Figure 4.16 (cont.).

There was no additional calibration considered for underwater experiments. Instead, using the relation given in Eq. (4.3), the pixel values in the reconstructed images are multiplied by 1.2×10^{-3}. For the turbulent flow results shown in Figure 4.16 generated at the flow rate of 1300 gallons/hour ($\approx 1.367 \times 10^{-3}\,\mathrm{m}^3/\mathrm{s}$), the average flow rate along the channel was found to be roughly $1.2 \times 10^{-3}\,\mathrm{m}^3/\mathrm{s}$, indicating a close match between the actual values and the reconstructed images. Being swept by only a single whisker due to restriction by the channel walls, the spatial resolution was relatively lower near the left and right ends of the image field, causing smearing effects in the reconstructed images as discussed above. The pixel locations near the top left and right corners that were not whisked at all were estimated purely based on the smoothness constraint on the water-flow. Therefore, using a different configuration rather than a parallel whisker array would extract more detailed information about the water-flow near the channel walls, but the Tikhonov-regularization has still produced reliable results, as the reconstructed cross-sectional images are mostly in agreement with the visual observation of the

circulating flow pattern along the open channel.

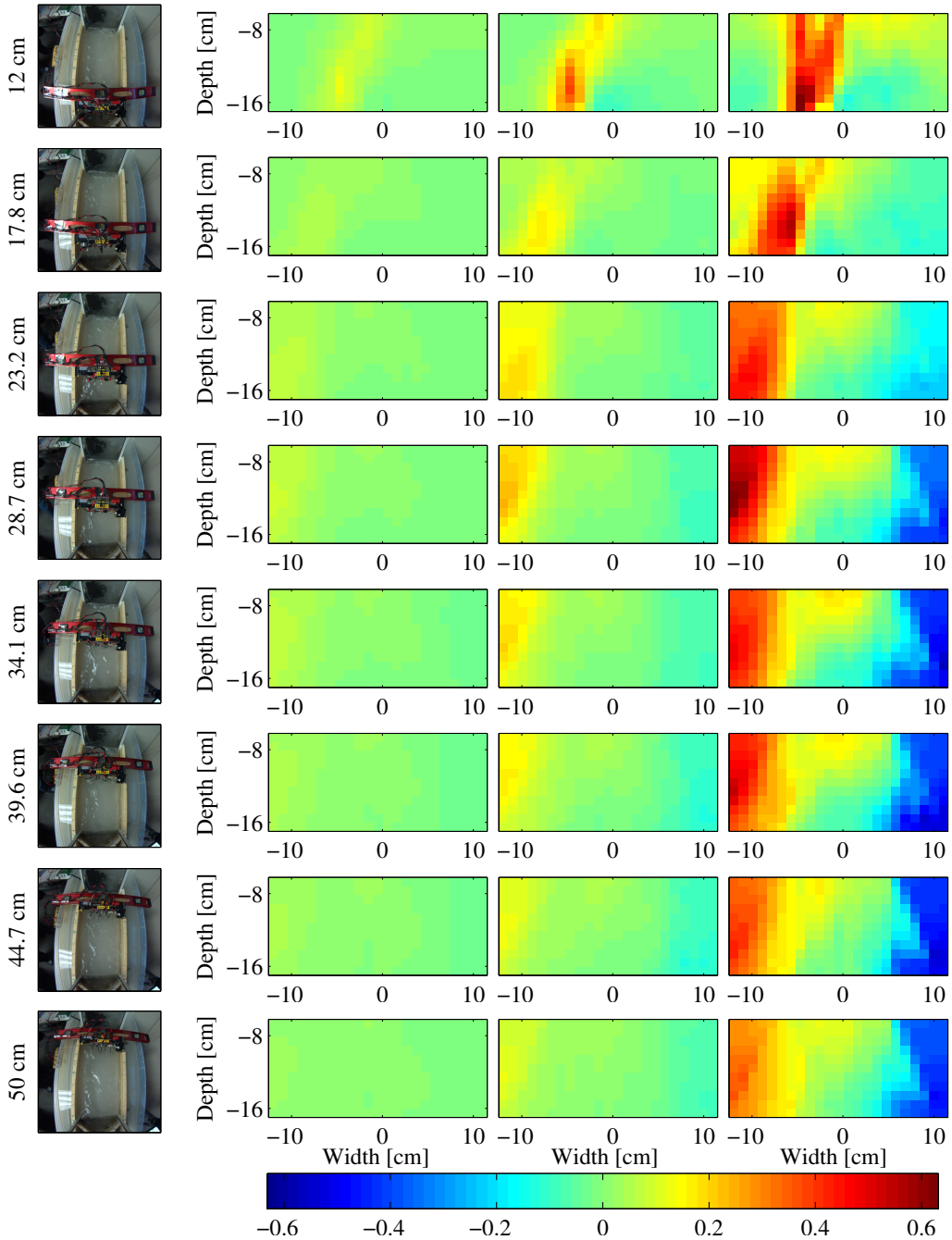

Figure 4.17: The 11×23 static velocity-squared images of the cross-sectional circulating water-flow patterns shown in Figures 4.14 (left), 4.15 (middle) and 4.16 (right) using the same color-mapping for the flow-fields: The flow rates for the two flow patterns shown in the left and middle columns are much lower than the turbulent flow shown in the right column such that the circulating flow pattern is barely noticeable under the same colormap.

All the imaging results are summarized in Figure 4.17 using the same colormap to demonstrate the variation in the flow strength between the circulating flow patterns generated at three different flow rates for a given location from left to right, and along the channel length from top to bottom.

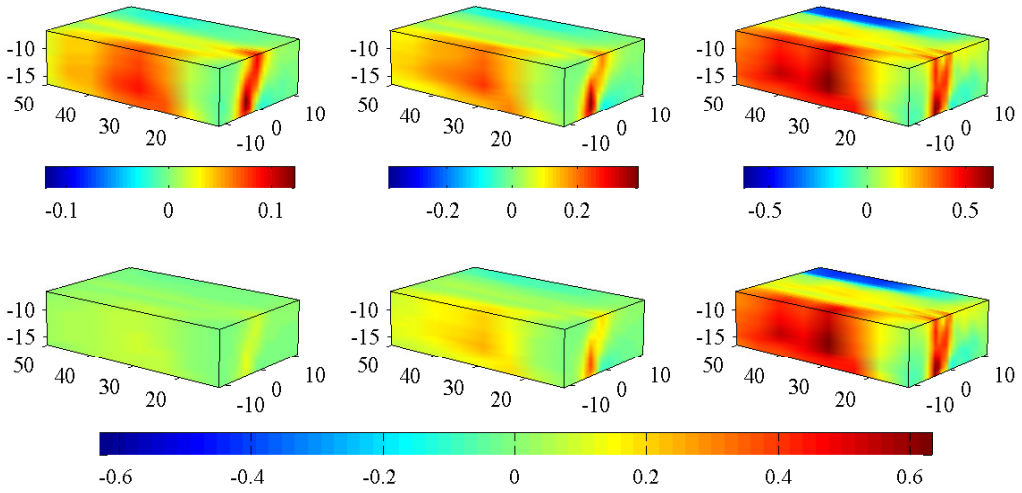

Figure 4.18: The 3-D volumetric rendering of the cross-sectional static waterflow velocity fields generated by the water pump at three different velocities (Top row: individual color-mapping for each flow-field, bottom row: common color-mapping for the flow-fields).

The 3-D volumetric rendering based on the reconstructions along the channel length are illustrated in Figures 4.18 and 4.19 from the opposite views. The results demonstrate that a 3-D flow profile of an open channel can be extracted by collecting the moment measurements at several distances from the flow source in a cross-sectional manner.

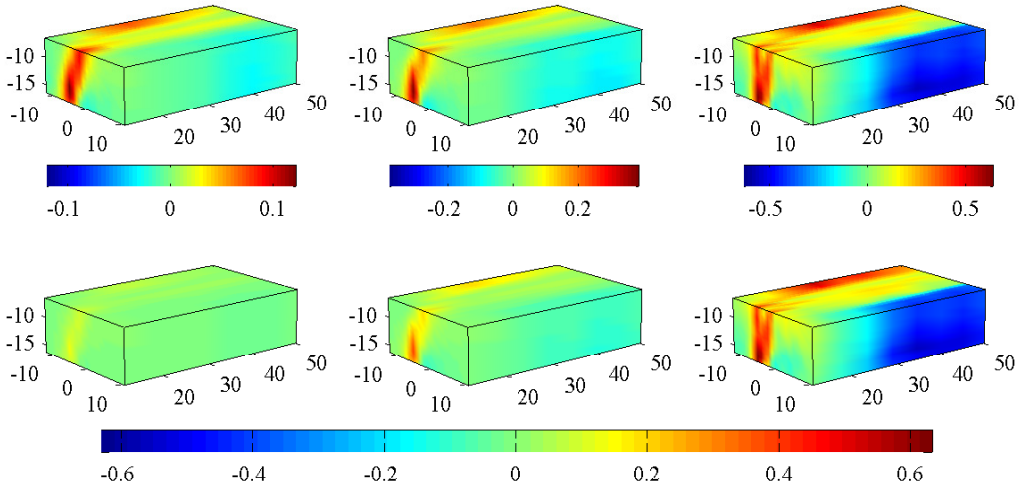

Figure 4.19: Another view of the 3-D volumetric rendering of the cross-sectional static water-flow velocity fields generated by the water pump at three different velocities (Top row: individual color-mapping for each flow-field, bottom row: common color-mapping for the flow-fields).

CHAPTER 5

Dynamic Tactile Fluid-Flow Imaging with a Robotic Whisker Array

In a dynamically changing environment, significant variations may occur in a very short time interval such that the stationarity assumption may not be valid any longer. This chapter presents the dynamic tactile fluid-flow tomographic imaging results when the flow patterns change dramatically both in air and underwater. Under the dynamic linear state-space model, the state estimates are obtained through the recursive Kalman filter procedure based on the measurements.

The chapter begins with the parameter selection for the tactile dynamic tomography model in Section 5.1. Next, the methods used for enforcing the smoothness constraint in the Kalman filter is explained in Section 5.2. Then, the dynamic air imaging results are given in Section 5.3 for several different situations including detecting time-varying flow patterns, moving flow sources, and tracking moving objects before the actual touch. Section 5.4 demonstrates the underwater imaging results for detecting moving objects, tracking fixed flow sources operating at time-varying flow rates and flow patterns directionally changing over time.

5.1 Parameter Selection

The Kalman filter recursion using the linear state-space model requires the prior knowledge of the initial state $\hat{\boldsymbol{x}}_{1|0} = \boldsymbol{\mu}_1$ and the initial state error covariance $\boldsymbol{P}_{1|0} = \boldsymbol{\Pi}_1$, the measurement and state noise covariances $\boldsymbol{R}_i$ and $\boldsymbol{Q}_i$, as well as the state evolution model $\boldsymbol{F}_i$.

Mathematically, it is very complicated to characterize the fluid-flow dynamics. Hence, as a practical remedy, the state evolution is assumed to be a random walk model by setting $\boldsymbol{F}_i = \boldsymbol{I}$, being completely driven by the process noise $\boldsymbol{u}_i$ [65], which has been previously used in several dynamic tomography applications including solar tomographic imaging of the corona [30, 31], and dynamic cardiac CT reconstruction [33]. The entirely stochastic state evolution model may be sufficient provided that the time interval between the two consecutive frames is relatively small. Otherwise, a frame-by-frame estimation of the motion model may also be possible using techniques such as the optical flow [66, 67].

The state noise covariance matrix $\boldsymbol{Q}_i = \boldsymbol{Q}$ is assumed to be fixed at any time index with no temporal variation, and approximated by computing the error covariance of the state noise estimates given by the first-order difference between two consecutive static reconstructions

$$\hat{\boldsymbol{u}}_i = \hat{\boldsymbol{x}}_{i+1}^S - \hat{\boldsymbol{x}}_i^S. \tag{5.1}$$

Each static reconstruction $\hat{\boldsymbol{x}}_i^S$ is given by the Tikhonov-regularized solution

$$\hat{\boldsymbol{x}}_i^S = (\boldsymbol{H}_{(i-L+1):i}^T \boldsymbol{H}_{(i-L+1):i} + \lambda \boldsymbol{D}^T \boldsymbol{D})^{-1} \boldsymbol{H}_{(i-L+1):i}^T \boldsymbol{y}_{(i-L+1):i}, \tag{5.2}$$

where $\boldsymbol{H}_{(i-L+1):i} = [\boldsymbol{H}_{(i-L+1)}^T, \ldots, \boldsymbol{H}_i^T]^T$, $\boldsymbol{y}_{(i-L+1):i} = [\boldsymbol{y}_{(i-L+1)}^T, \ldots, \boldsymbol{y}_i^T]^T$, and L corresponds to the number of angular views used for static reconstruction. The state noise covariance matrix $\boldsymbol{Q}$ is then approximated by computing the sample covariance of the state noise estimates $\hat{\boldsymbol{u}}_i$:

$$\boldsymbol{Q} \approx \frac{1}{I-2} \sum_{i=1}^{I-1} \left(\hat{\boldsymbol{u}}_i - \frac{1}{I-1} \sum_{i=1}^{I-1} \hat{\boldsymbol{u}}_i \right) \left(\hat{\boldsymbol{u}}_i - \frac{1}{I-1} \sum_{i=1}^{I-1} \hat{\boldsymbol{u}}_i \right)^T, \tag{5.3}$$

where I denotes the final time index.

The measurement noise covariance $\boldsymbol{R}_i = \boldsymbol{R}$ is also assumed to be temporally unchanged and inferred from the measurements collected when there was no flow source present. The initial prior mean $\boldsymbol{\mu}_1 = \hat{\boldsymbol{x}}_1^S$ is the first static reconstruction and the initial state error covariance is $\boldsymbol{\Pi}_1 = \boldsymbol{Q}$.

5.2 The Smoothness Constraint in the Kalman Filter

In order to incorporate Tikhonov regularization into the KF measurement update to enforce smoothness on the KF estimates, the method of pseudo-observation methods can be used to augment the spatial smoothness constraint into the forward model as additional observations [68–70]. The augmented forward model is given by [32]

$$\tilde{\boldsymbol{y}}_i = \tilde{\boldsymbol{H}}_i \boldsymbol{x}_i + \tilde{\boldsymbol{w}}_i \tag{5.4}$$

$$\begin{bmatrix} \boldsymbol{y}_i \\ \boldsymbol{0} \end{bmatrix} = \begin{bmatrix} \boldsymbol{H}_i \\ \boldsymbol{D}_i \end{bmatrix} \boldsymbol{x}_i + \begin{bmatrix} \boldsymbol{w}_i \\ \boldsymbol{v}_i \end{bmatrix}, \tag{5.5}$$

where the augmented measurement noise vector $\boldsymbol{v}_i$ is zero-mean, uncorrelated with the initial state $\boldsymbol{x}_1$ and the state noise $\boldsymbol{u}_i$. The new measurement error covariance for the augmented forward model then becomes

$$\tilde{\boldsymbol{R}}_i = \mathbb{E}\begin{bmatrix}\boldsymbol{w}_i \\ \boldsymbol{v}_i\end{bmatrix}\begin{bmatrix}\boldsymbol{w}_i & \boldsymbol{v}_i\end{bmatrix} = \begin{bmatrix}\boldsymbol{R}_i & \boldsymbol{0} \\ \boldsymbol{0} & \lambda_i^{-1}\boldsymbol{I}\end{bmatrix}. \tag{5.6}$$

If the system is severely underdetermined ($M << N$), such as in our case, where there are only five measurements collected with the whisker array at each time index, the augmented model may increase the computational time as the Kalman gain and measurement matrices get considerably larger in size. Alternatively, it is also possible to use a projection method to enforce the smoothness constraint on the state estimates. The projection methods are generally used to impose linear equality constraints on the posterior estimate $\hat{\boldsymbol{x}}_{i|i}$ by projecting it onto the desired constraint subspace [70–72]. In our case, using the fact that the static estimate $\hat{\boldsymbol{x}}_{i+1}^S$ for the next time $i+1$ is already computed to obtain the approximate state error covariance matrix $\boldsymbol{Q}$, the posterior state estimate $\hat{\boldsymbol{x}}_{i|i}$ can be simply projected onto the Tikhonov-regularized static estimate $\hat{\boldsymbol{x}}_{i+1}^S$, which is already smooth, to be used as the prior estimate $\hat{\boldsymbol{x}}_{i+1|i}$ for the next measurement update at the time index $i+1$. This can be achieved by treating the vector projection operator as a pseudo-evolution matrix with rank 1:

$$\hat{\boldsymbol{F}} = \hat{\boldsymbol{x}}_{i+1}^S \frac{\hat{\boldsymbol{x}}_{i+1}^{S\ T}}{||\hat{\boldsymbol{x}}_{i+1}^S||_2^2}. \tag{5.7}$$

The new time update is then given by

$$\hat{\boldsymbol{x}}_{i+1|i} = \hat{\boldsymbol{F}}_i \hat{\boldsymbol{x}}_{i|i} = f_i \hat{\boldsymbol{x}}^S_{i+1} \tag{5.8}$$

$$\boldsymbol{P}_{i+1|i} = \hat{\boldsymbol{F}}_i \boldsymbol{P}_{i|i} \hat{\boldsymbol{F}}_i^T + \boldsymbol{Q}_i. \tag{5.9}$$

In other words, the corrections based on the measurement vector $\boldsymbol{y}_{i+1}$ during the measurement update at the time index $i+1$ are made on the static smooth estimate $\hat{\boldsymbol{x}}^S_{i+1}$ scaled by f_i, which describes a measure of distance from the KF estimate $\hat{\boldsymbol{x}}_{i|i}$, and takes values depending on the system dynamics.

5.3 Experimental Setup

The measurements at each angular view were collected by averaging the calibrated data over 0.52 seconds for both dynamic in-air and underwater imaging experiments. In order to increase temporal resolution, an intermediate view was generated by using the data during the rotation between the two consecutive views with its angle to be the average of the recorded angles corresponding to the two consecutive stops, which resulted in a frame rate of 1.92 frames/second. The air-flow experiments were performed with the hair dryer at the distances of 19.5 cm, 35.5 cm and 60.5 cm away from the whisker array for 650 seconds, collecting the data for 1250 time instances at each case. On the other hand, the whisker array was located at 28.7 cm and 44.7 cm away from the hose exit for dynamic underwater imaging, performing experiments for 544.5 seconds, which results in a total number of 1050 angular views for each of the two cases. All the experiments were recorded by a handy-cam and a wide-angle HD camera.

The Tikhonov-regularized static reconstructions were computed using a number of consecutive views, $L_{air} = 25$ for in-air and $L_{water} = 15$ for underwater experiments corresponding to the maximum possible angular range swept by the whisker array during the experiments. Therefore, the number of measurements for a static reconstruction was $M = 25 \times 5 = 125$ in air and $M = 15 \times 5 = 75$ for underwater flow experiments. A 13×21 image matrix ($N = 273$) was used for in-air flow experiments, resulting in linear matrix operators, $\boldsymbol{H}^{125\times 273}$ for static and $\boldsymbol{H}_i^{5\times 273}$ for dynamic reconstructions. For underwater flow experiments, the measurement matrices were $\boldsymbol{H}^{75\times 253}$ for static and $\boldsymbol{H}_i^{5\times 253}$ for dynamic imaging, using a 11×23 pixel array ($N = 253$). The initial prior mean $\boldsymbol{\mu}_1 = \hat{\boldsymbol{x}}_1^S$ was computed using the first $L_{air} = 25$ for air and $L_{water} = 15$ for underwater experiments, which resulted in a total number of states, $I_{air} = 1226$ for each of the three air experiments, whereas $I_{water} = 1036$ for the two sets of underwater experiments.

Under the additive linear Gaussian noise signal model, the noise statistics were inferred from the measurements collected when there was no flow source present. The measurement noise covariance matrices were set to be fixed in time as $\boldsymbol{R}_i^{air} = 1.4 \times 10^{-4}\boldsymbol{I}_{5\times 5}$ for air and $\boldsymbol{R}_i^{water} = 6 \times 10^{-3}\boldsymbol{I}_{5\times 5}$ for underwater experiments. The correlations between the whiskers were not taken into account, and the noise variance was assumed to be the same for each whisker. The off-diagonal elements as well as the individual noise variances of the whiskers could be learned by collecting data over a longer period of time, but using the same noise covariance at each time index with equal elements on its diagonal was sufficient in our case.

The same gradient operator $\boldsymbol{D}_i = \boldsymbol{D}$ was used for static and dynamic reconstructions at each time index. The regularization parameter for dynamic

reconstructions was manually set to be $\lambda_i^D = \lambda^D = 5 \times 10^{-7}$ for in-air and $\lambda_i^D = \lambda^D = 2 \times 10^{-7}$ for underwater experiments.

The state noise covariance matrix $\boldsymbol{Q}$ was approximated via the static reconstructions over the entire data set using the regularization parameter $\lambda_i^S = \lambda^S = 3 \times 10^{-9}$ for both in-air and underwater experiments. The approximate state noise covariance matrices learned from the in-air and underwater static reconstructions are shown in Figure 5.1. These matrices may give some insight into the system activity as the pixels with large correlations correspond to the location of the hair dryer for air flow, whereas the the circulating flow characterized by the positive and negative directional flows at opposite sides can be observed in both ends of the approximate state noise covariance matrix for underwater flow.

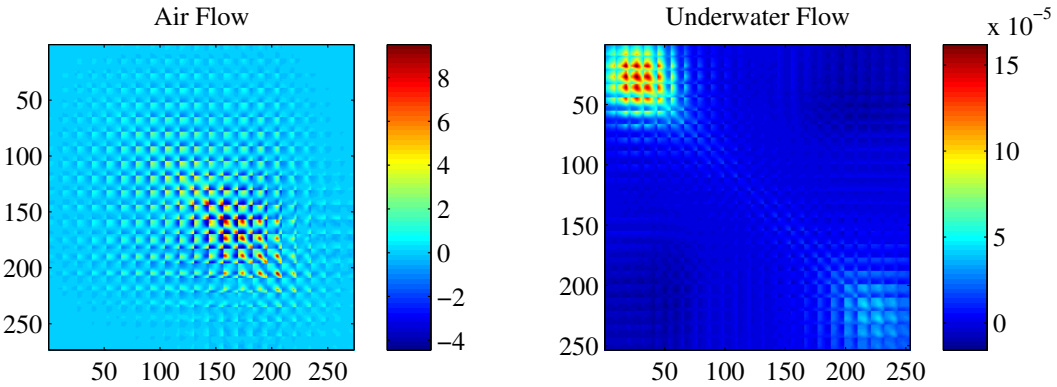

Figure 5.1: The approximate state noise covariance matrix $\boldsymbol{Q}_i = \boldsymbol{Q}$ for air (left) and underwater (right) flow experiments inferred from static reconstructions over the entire data set.

The relative residual error is defined as

$$\boldsymbol{r}_i = \frac{||\boldsymbol{y}_i - \boldsymbol{H}_i \hat{\boldsymbol{x}}_i||_2}{||\boldsymbol{y}_i||_2}, \tag{5.10}$$

indicating the consistency between the physically measured moment data and

the estimated moment via the forward model, whereas the measure of smoothness, which is given by $||\boldsymbol{D}_i\hat{\boldsymbol{x}}_i||_2$, yields quantitative information about the smoothness quality of a velocity-squared distribution reconstruction.

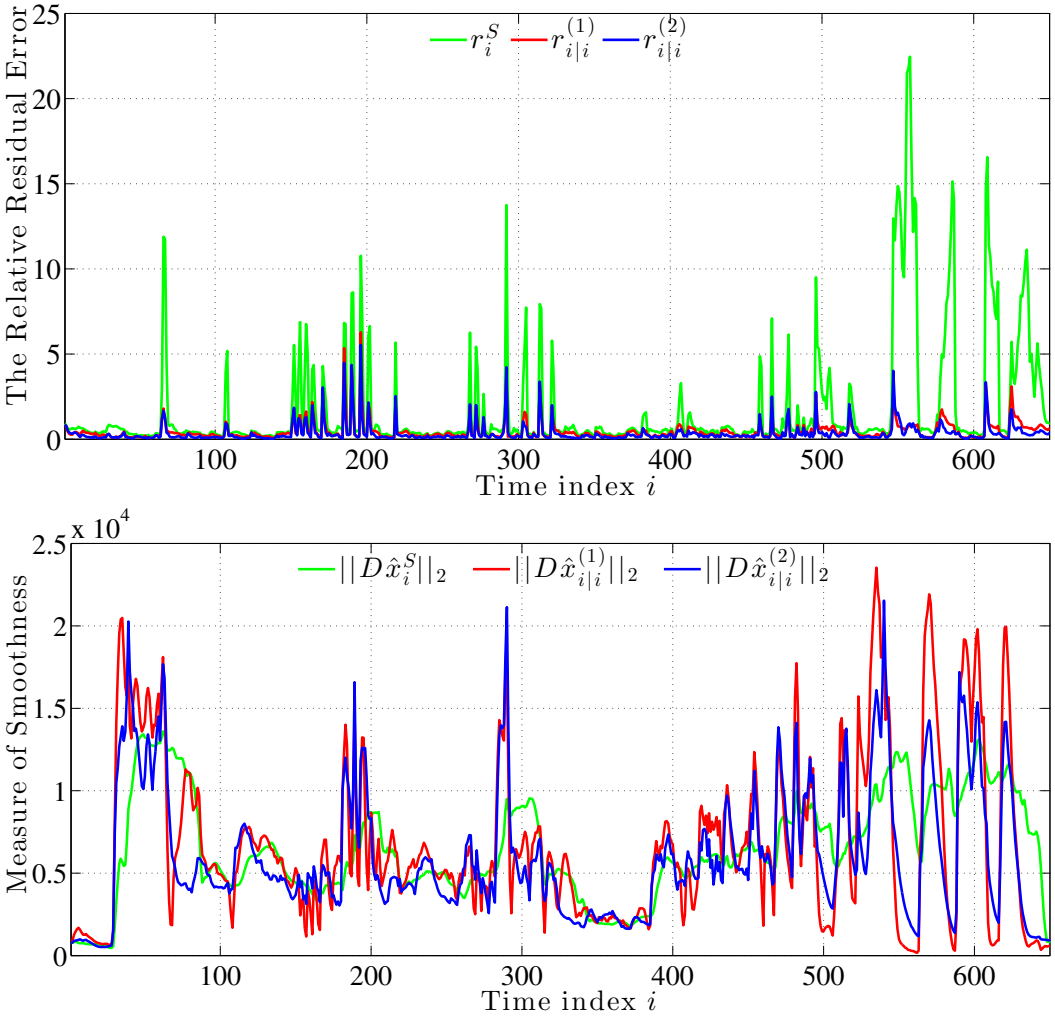

Figure 5.2: In-air flow experiments with the hair dryer located at 35.5 cm away from the whisker array between the states $\boldsymbol{x}_1$ and $\boldsymbol{x}_{650}$: The comparison of the relative residual error (top) and the measure of smoothness (bottom) between the static estimate $\hat{\boldsymbol{x}}_i^S$, the first posterior KF estimate $\hat{\boldsymbol{x}}_{i|i}^{(1)}$ using the vector projection method with the fixed static regularization parameter $\lambda_i^S = \lambda^S = 3 \times 10^{-9}$ and the second posterior KF estimate $\hat{\boldsymbol{x}}_{i|i}^{(2)}$ using the augmented forward model with the fixed dynamic regularization parameter $\lambda_i^D = \lambda^D = 5 \times 10^{-7}$ to enforce smoothness on the estimates.

The relative residual error and the measure of smoothness are used to eval-

uate the performance of the Tikhonov-regularized static reconstructions and the Kalman filter estimates, since there were only camera recordings available as the ground truths rather than the actual physical velocity-squared distributions. Figure 5.2 illustrates an example that compares the relative residual errors and the measure of smoothness between the static estimate $\hat{\boldsymbol{x}}_i^S$, the first posterior KF estimate $\hat{\boldsymbol{x}}_{i|i}^{(1)}$ using the vector projection method and the second posterior KF estimate $\hat{\boldsymbol{x}}_{i|i}^{(2)}$ using the augmented forward model to impose spatial smoothness on the reconstructions. As discussed in [31], a smaller relative residual error does not guarantee a better reconstruction as enforcing spatial smoothness increases the relative residual in general. However, the camera recordings of the experiments evidently indicate that dynamic reconstructions outperform static reconstructions, and generally result in smaller relative residuals than static reconstructions, particularly in the case of abrupt changes in the system evolution as observed as large peaks in the top row of Figure 5.2. On the other hand, the measure of smoothness indicates that the dynamic reconstructions capture the system evolution as the amount of smoothness fluctuates, changing significantly from one state to another, whereas nearly the same smoothness level is preserved between the two consecutive states for static reconstructions. It can be also deduced that significant changes occur in the system when there are large fluctuations in the measure of smoothness for dynamic reconstructions, whereas the system may be considered as nearly stationary when there are only small alterations around the static smoothness level for the posterior KF estimates.

If a comparison is made between the two posterior KF estimates, it can be concluded that they achieve similar amounts of smoothness but further detailed ground truth information is needed to determine which KF estimate

is better than the other. Figure 5.3 illustrates the difference in the level of smoothness between the prior $\hat{\boldsymbol{x}}^{(1)}_{i-1|i} = f_{i-1}\hat{\boldsymbol{x}}^{S}_{i}$ and the posterior $\hat{\boldsymbol{x}}^{(1)}_{i|i}$ KF estimates using the vector projection method to enforce smoothness. The results demonstrate that the corrections made on the prior estimates based on the next available measurements are seen as the small changes in the posterior smoothness level.

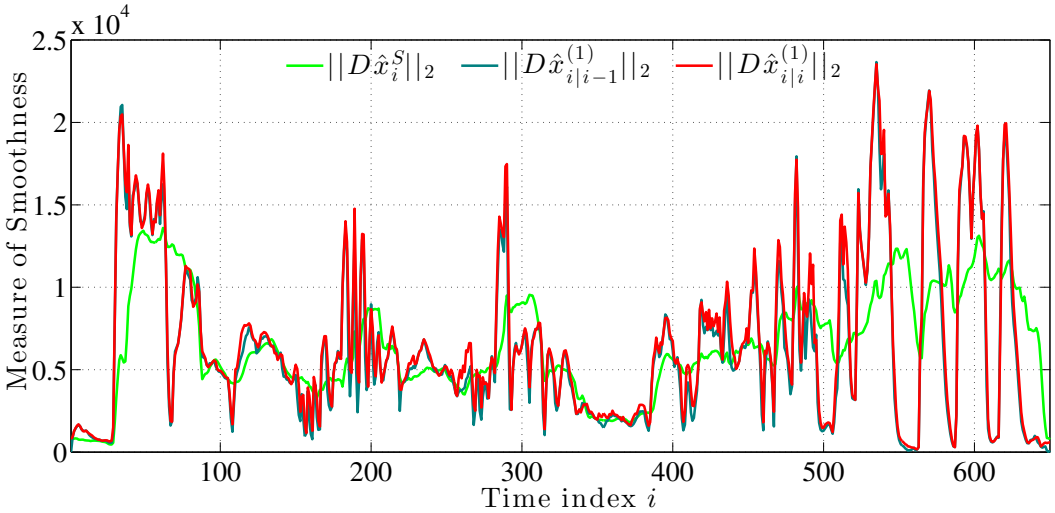

Figure 5.3: The comparison of the measure of smoothness between the static estimate $\hat{\boldsymbol{x}}^{S}_{i}$, the prior KF estimate $\hat{\boldsymbol{x}}^{(1)}_{i|i-1} = f_{i-1}\hat{\boldsymbol{x}}^{S}_{i}$ and the posterior KF estimate $\hat{\boldsymbol{x}}^{(1)}_{i|i}$ using the vector projection method to enforce smoothness on the estimates with the fixed static regularization parameter $\lambda^{S}_{i} = \lambda^{S} = 3 \times 10^{-9}$ for in-air flow experiments with the hair dryer located at 35.5 cm away from the whisker array between the states $\boldsymbol{x}_1$ and $\boldsymbol{x}_{650}$.

The local impulse response for the Kalman filter estimates derived in [31] under the linear-state space model is also computed to compare the two posterior KF estimates in terms of the spatial-temporal resolution, which is given by the following theorem.

Theorem 5.1: Given the simulated measurements $\boldsymbol{y}_{1:i} = [\boldsymbol{y}^{T}_{1}, \boldsymbol{y}^{T}_{2}, \cdots, \boldsymbol{y}^{T}_{i}]^{T}$,

where

$$\boldsymbol{y}_m = \begin{cases} \boldsymbol{H}_k \boldsymbol{e}^j, & m = k \\ \\ \boldsymbol{0}, & \text{otherwise} \end{cases} \tag{5.11}$$

and the initial prior mean $\boldsymbol{\mu}_1 = \boldsymbol{0}$, the KF procedure yields the filtered local impulse response $\boldsymbol{l}_{i|i}^{j,k}$ [31] for the jth parameter of the posterior KF estimate in Eq. (3.23) and the time index k.

Proof: See Section 6.2 in [31].

Due to the spatially sparse nature of the whisker array, not all the pixels are swept by a whisker at a given angular view, producing zero local impulse response through the KF process with $\boldsymbol{\mu}_1 = \boldsymbol{0}$. On the other hand, for the pixels from for which some information is received via the whisker array, there are two possible cases, one in which a pixel is very close to the intersection of the two whiskers from the front and back rows of the whisker array rotating in opposite directions and the other when the pixel is located near a single whisker path. Figure 5.4 illustrates the image representations of the unit vectors $\boldsymbol{e}^{110}$ whose only nonzero value is located at the intersection of two whisker paths and $\boldsymbol{e}^{175}$ taking the value of 1 only at a pixel location along a single whisker path. The corresponding local impulse response functions are given in Figure 5.5 for time index 35 using the same color scale between time indices 35 and 47 within two time steps for the two posterior KF estimates, where the measurement and state noise covariance matrices estimated for the air-flow experiments are used for the KF procedure with $\lambda_i^S = \lambda^S = 3 \times 10^{-9}$ for the first KF posterior estimate to compute the pseudo-evolution matrix at each time index ($\boldsymbol{F}_i \neq \boldsymbol{I}$) and $\lambda_i^D = \lambda^D = 5 \times 10^{-7}$ for the second posterior KF estimate with $\boldsymbol{F}_i = \boldsymbol{I}$.

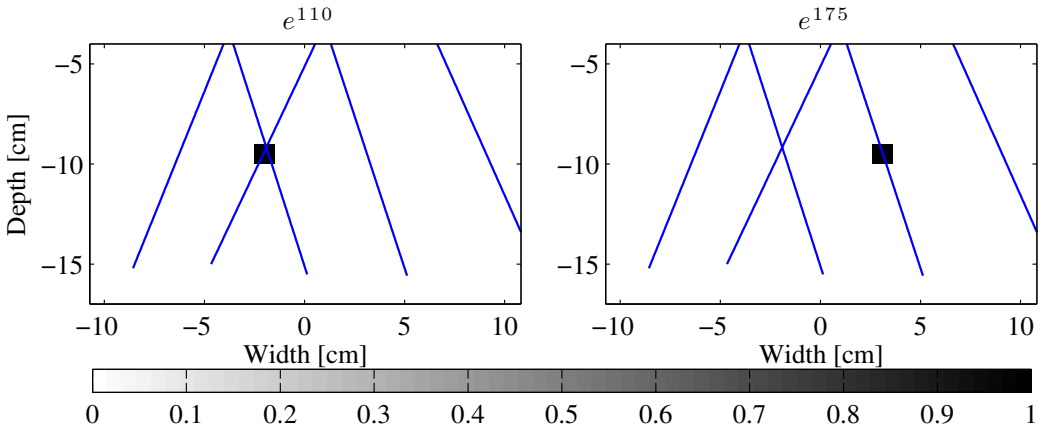

Figure 5.4: The image representation of two unit vectors at time index 35: Left: The unit vector $\boldsymbol{e}^{110}$ with its only nonzero value corresponding to a pixel located at the intersection of two whisker paths. Right: The unit vector $\boldsymbol{e}^{175}$ with its only nonzero value corresponding to a pixel location along a single whisker path.

As expected, the local impulse response functions for the two unit vectors concentrate along the corresponding whisker paths with larger-magnitude pixels for the first case when the two whisker paths intersect at a given angular view. Comparing the temporal resolution between the two cases, the local impulse functions for the unit vector $\boldsymbol{e}^{110}$ decays faster than the single-path case, in which it takes a number of time instances for the nonzero pixel location of the unit vector $\boldsymbol{e}^{175}$ to be swept by another whisker due to the spatial sparseness of the whisker array, whereas the two whisker paths continue to intersect in the next few time frames for the first case, relatively increasing the temporal resolution.

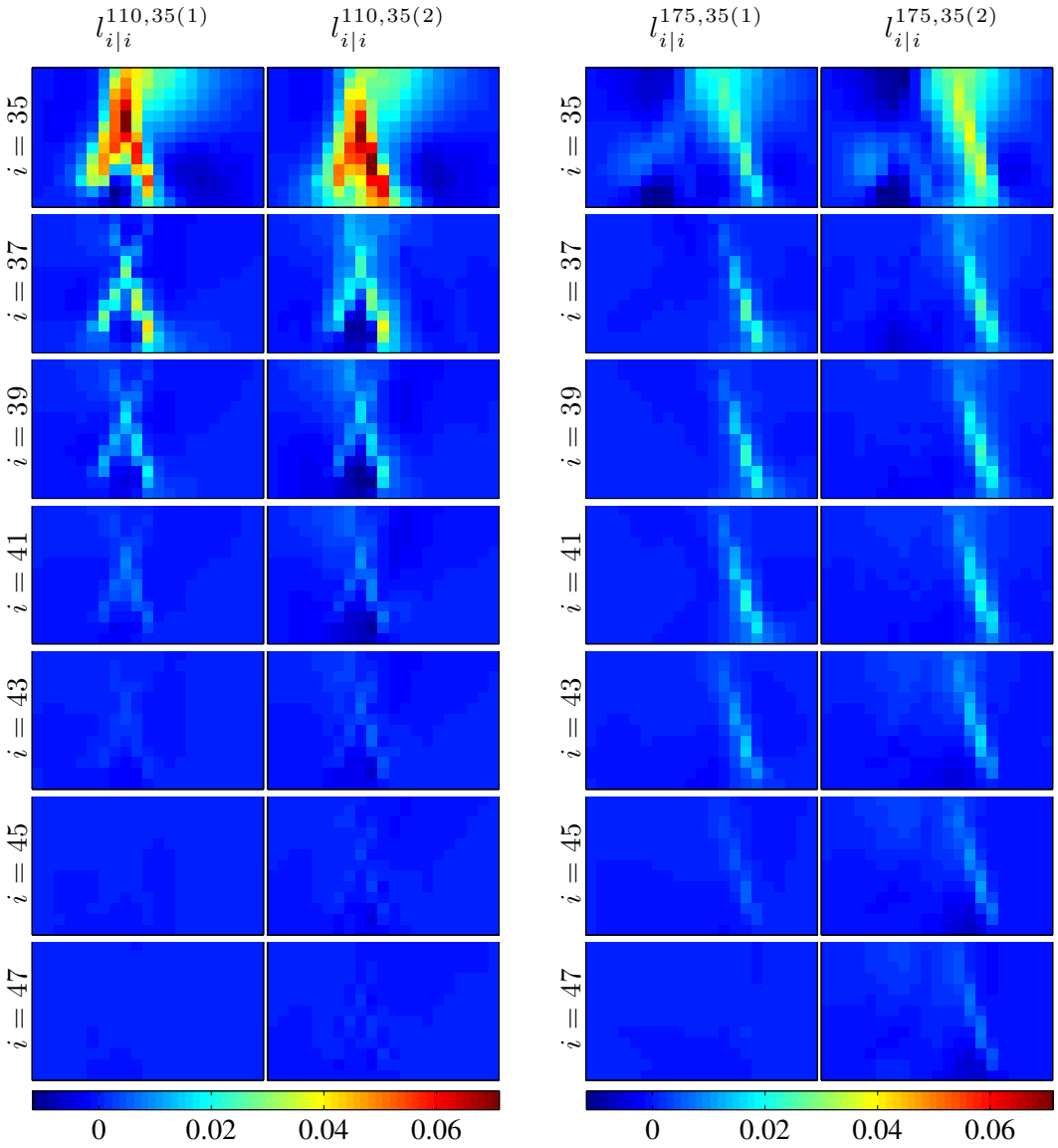

Figure 5.5: The local impulse response for the time index 35 and the unit vectors $\boldsymbol{e}^{110}$ (left) and $\boldsymbol{e}^{175}$ (right) shown in Figure 5.4 between the time indices 33 and 47 within two time steps: $\boldsymbol{l}_{i|i}^{j,k(1)}$ and $\boldsymbol{l}_{i|i}^{j,k(2)}$ correspond to the local impulse response for the posterior KF estimates using the vector projection method ($\boldsymbol{F}_i \neq \boldsymbol{I}$) and the purely random walk model ($\boldsymbol{F}_i = \boldsymbol{I}$), respectively.

The resulting local impulse response functions also suggest that the vector projection method and the random walk model have similar spatial characteristics, and in both cases, the local impulse response functions decay quickly

in time. The only difference between the two KF procedures is that the local impulse response functions for the random walk model is slightly broader than the ones for the vector projection method at time index 35, which can be explained by the fact that the vector projection method estimates are constrained by the static reconstructions. However, as also mentioned above, no conclusive argument can be made about the performance of the two KF procedures without detailed ground truth information, since different choices for the values of the static and dynamic regularization parameters could produce contrasting results.

5.4 Dynamic Tactile Air-Flow Imaging

There are eight cases picked from the three sets of experiments performed using the hair dryer as an air-flow source at the distances of 19.5 cm, 35.5 cm and 60.5 cm away from the whisker array, including the instantaneous capture of the abrupt changes in the system dynamics and the tracking of a moving flow source, and a moving object under steady flow. The static regularization parameter was set to be $\lambda_S = 3 \times 10^{-9}$ at 19.5 cm and 35.5 cm, whereas $\lambda_S = 5 \times 10^{-9}$ was selected for the experiments at 60.5 cm to increase smoothness due to the signal weakening as the hair dryer moves very far away from the whisker array. On the other hand, it was sufficient to use the same dynamic regularization parameter, $\lambda_D = 5 \times 10^{-7}$ in all cases.

5.4.1 The Detection of an Air-Flow Source

The first case involves capturing the system dynamics when the hair dryer is suddenly turned on. Figure 5.6 illustrates the period before and after turning

the hair dryer on described by the states $\boldsymbol{x}_{24}$ through $\boldsymbol{x}_{48}$ with the hair dryer positioned at 19.5 cm away from the whisker array. Figure 5.7 shows the comparison of the corresponding relative residual error and measure of smoothness between the estimates $\hat{\boldsymbol{x}}_i^S$, $\hat{\boldsymbol{x}}_{i|i}^{(1)}$ and $\hat{\boldsymbol{x}}_{i|i}^{(2)}$ for the states $\boldsymbol{x}_{24}$ through $\boldsymbol{x}_{48}$.

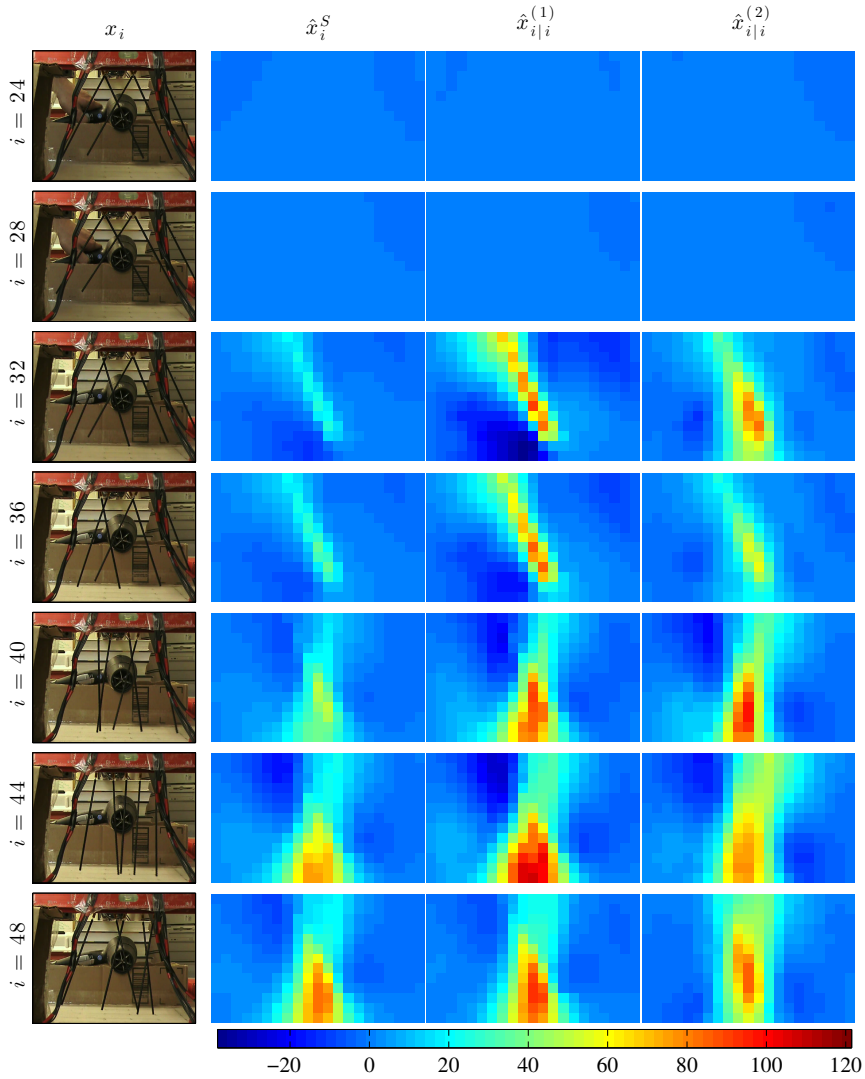

Figure 5.6: The static and dynamic tactile tomographic imaging results for the estimates $\hat{\boldsymbol{x}}_i^S$, $\hat{\boldsymbol{x}}_{i|i}^{(1)}$ and $\hat{\boldsymbol{x}}_{i|i}^{(2)}$ during the period before and after the hair dryer located at 19.5 cm away from the whisker array was turned on for the states $\boldsymbol{x}_{24}$ through $\boldsymbol{x}_{48}$.

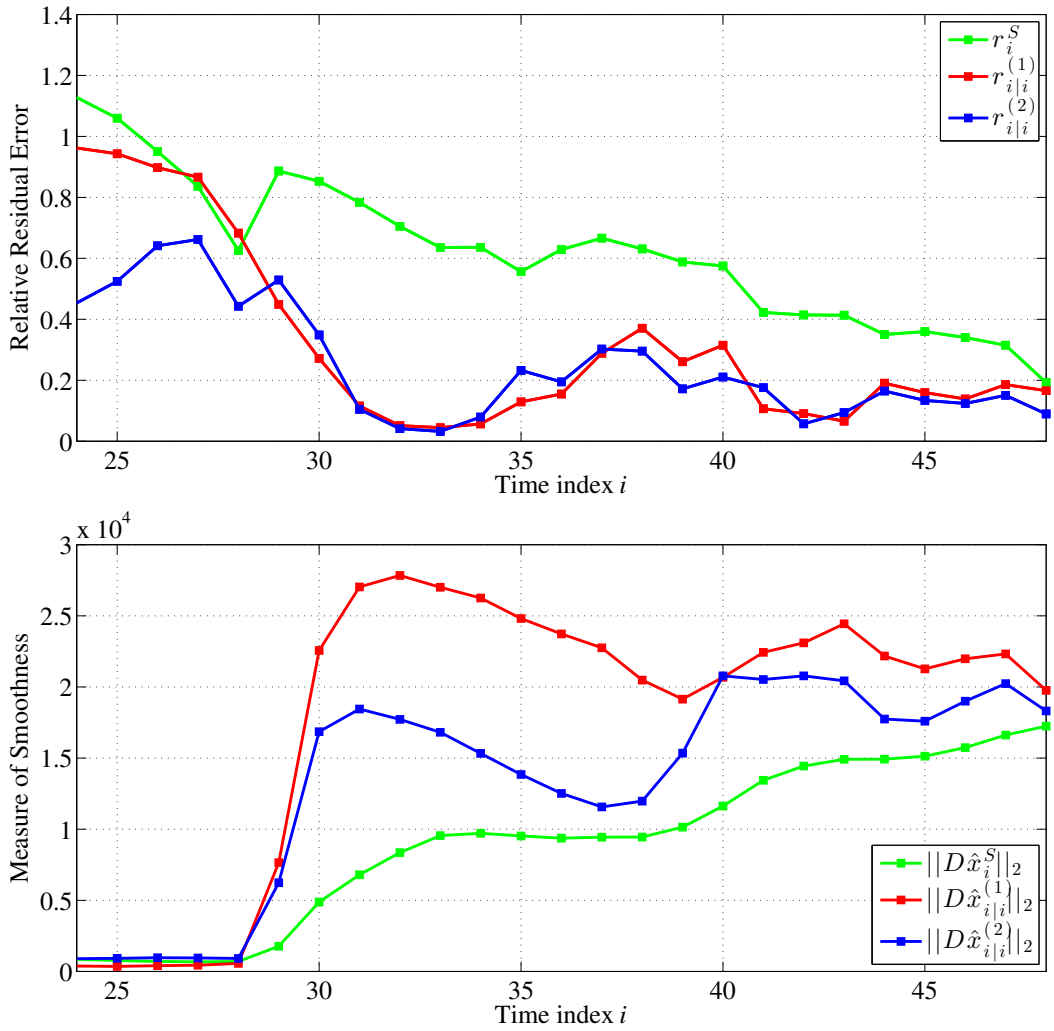

Figure 5.7: The comparison of the relative residual error (top) and the measure of smoothness (bottom) between $\hat{\boldsymbol{x}}_i^S$, $\hat{\boldsymbol{x}}_{i|i}^{(1)}$ and $\hat{\boldsymbol{x}}_{i|i}^{(2)}$ during the period before and after the hair dryer located at 19.5 cm away from the whisker array was turned on for the states $\boldsymbol{x}_{24}$ through $\boldsymbol{x}_{48}$.

It is clearly seen in the resulting reconstructions that the static case gradually captures the state dynamics, whereas the two dynamic reconstructions immediately tune into the abrupt dynamical change. Once the hair dryer was turned on, starting at state $\boldsymbol{x}_{28}$, a decrease in the relative residual error is observed and a quick rise in the measure of smoothness for the dynamic cases, whereas the decrease in the relative residual error and the increase in the

smoothness level are gradually occurring in the static reconstructions, reaching the level of dynamic reconstructions only after 24 frames at state $\boldsymbol{x}_{48}$ as the system becomes more stationary with a fixed, unchanging flow source.

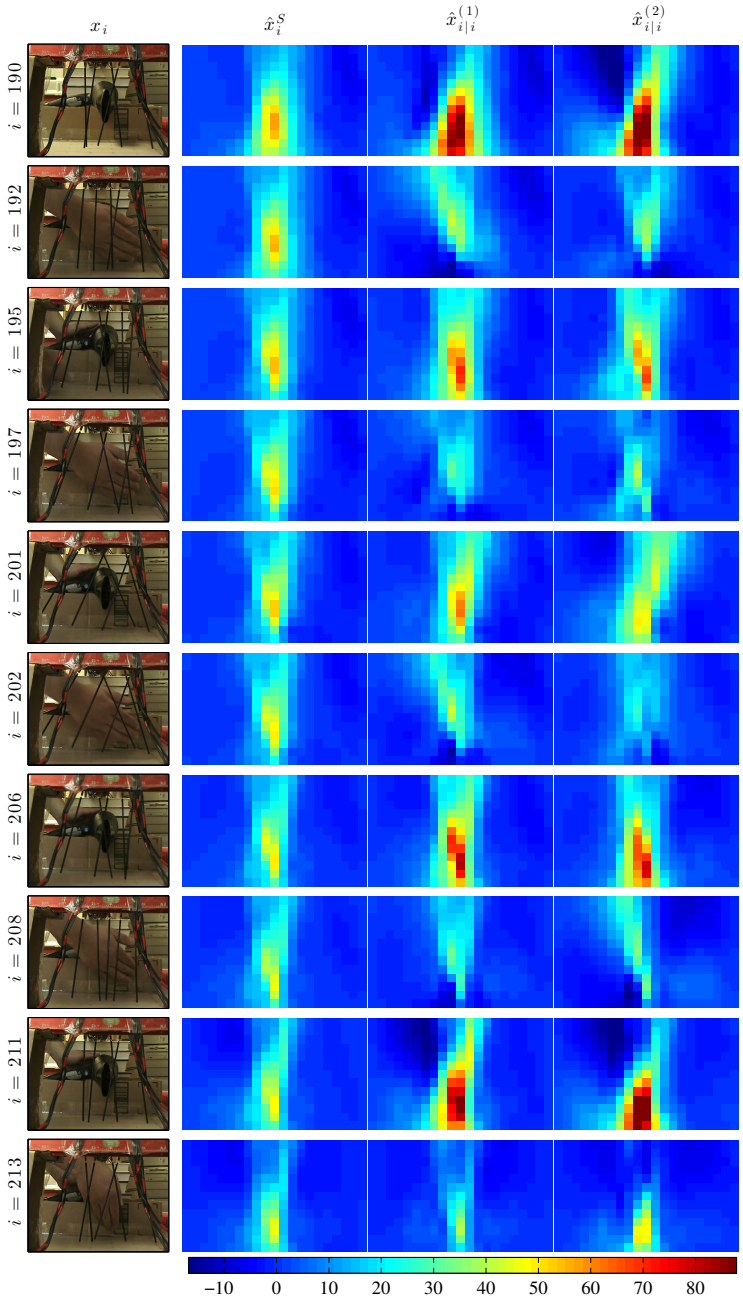

Figure 5.8: The static and dynamic tactile tomographic imaging results for the estimates $\hat{\boldsymbol{x}}_i^S$, $\hat{\boldsymbol{x}}_{i|i}^{(1)}$ and $\hat{\boldsymbol{x}}_{i|i}^{(2)}$ during the event of the frequent blocking and release of the hair dryer positioned at 19.5 cm between the states $\boldsymbol{x}_{190}$ and $\boldsymbol{x}_{213}$.

5.4.2 The Abrupt Block and Release of the Air-Flow Source

The second case examines the detection capability of the dynamic model when the hair dryer located at 19.5 cm was blocked periodically in a very frequent manner, as displayed in Figure 5.8 between the states $\boldsymbol{x}_{190}$ and $\boldsymbol{x}_{213}$. The relative residual error and the measure of smoothness are presented in Figure 5.9 for the estimates $\hat{\boldsymbol{x}}_i^S$, $\hat{\boldsymbol{x}}_{i|i}^{(1)}$ and $\hat{\boldsymbol{x}}_{i|i}^{(2)}$ between the states $\boldsymbol{x}_{190}$ through $\boldsymbol{x}_{213}$.

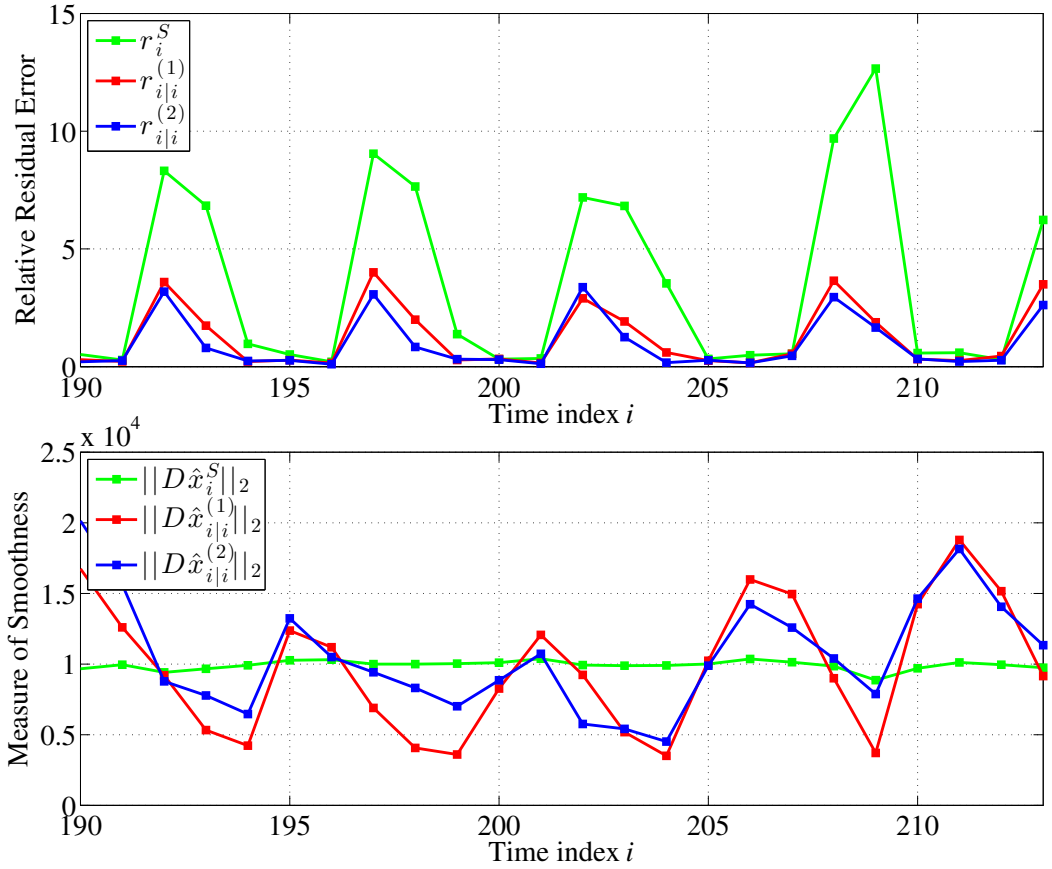

Figure 5.9: The comparison of the relative residual error (top) and the measure of smoothness (bottom) between $\hat{\boldsymbol{x}}_i^S$, $\hat{\boldsymbol{x}}_{i|i}^{(1)}$ and $\hat{\boldsymbol{x}}_{i|i}^{(2)}$ during the event of the frequent blocking and release of the hair dryer positioned at 19.5 cm between the states $\boldsymbol{x}_{190}$ and $\boldsymbol{x}_{213}$.

The tomographic imaging results demonstrate that the static reconstructions completely fail to detect the dynamic "block and release" pattern yielding nearly the same solution at each state, whereas the two dynamic KF estimates keep track of the periodic pattern, which can also be noticed in the relative residual and the measure of smoothness, where the peaks in the residual error match the states during which the hair dryer was blocked, and the peaks for the static case are much larger than the two dynamic KF estimates. On the other hand, the periodic pattern translates into deep notches in the smoothness level for the two dynamic cases, whereas the static smoothness quality stays nearly constant as the static case yields similar reconstructions for almost all the states.

5.4.3 The Tracking of a Moving Flow Source

There are two cases examined to evaluate the performance of the dynamic tactile tomographic imaging in tracking moving flow sources. The first case involves the tracking of the hair dryer initially located at 35.5 cm away from the whisker array with the concentrator attached in the right-tilted position as the hair dryer moves along the region between its initial location and the whisker array. Figure 5.10 demonstrates the static and dynamic tactile tomographic imaging results between the states $\boldsymbol{x}_{450}$ and $\boldsymbol{x}_{458}$. The corresponding relative residual error and the measure of smoothness results are also presented in Figure 5.11.

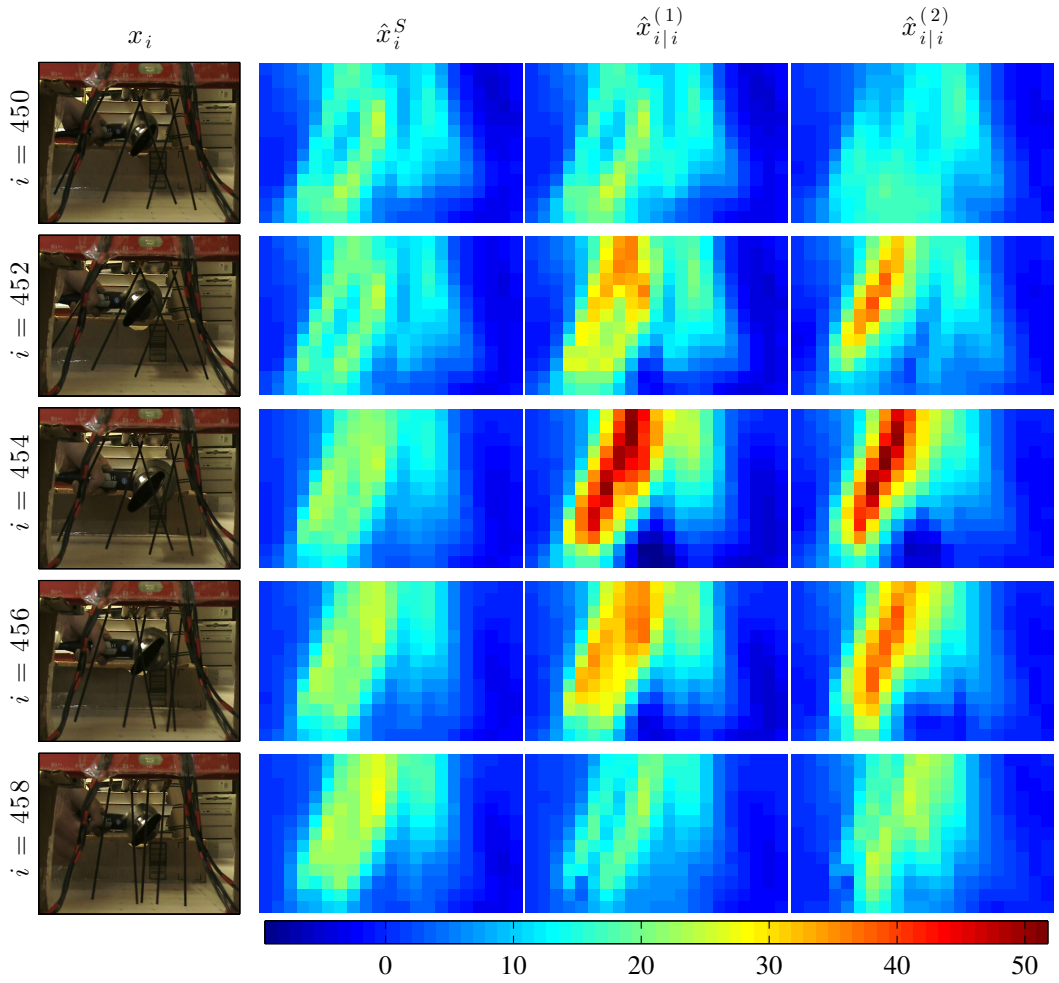

Figure 5.10: The static and dynamic tactile tomographic imaging results for the estimates $\hat{\boldsymbol{x}}_i^S$, $\hat{\boldsymbol{x}}_{i|i}^{(1)}$ and $\hat{\boldsymbol{x}}_{i|i}^{(2)}$ during the event of the hair dryer with the right-tilted concentrator initially positioned at 35.5 cm moving along the region between its original position and the whisker array between the states $\boldsymbol{x}_{450}$ and $\boldsymbol{x}_{458}$.

The imaging results illustrate that as the hair dryer approaches the whisker array, the magnitude of the right-tilted flow pattern gets strengthened and then begins to attenuate with the hair dryer moving back toward its initial position. This pattern can be observed as a gradual increase in the measure of smoothness for the dynamic reconstructions during the movement toward the whisker array followed by a gradual decrease as the whisker moves back to

its original position. The static reconstructions suggest once again that they tend to keep the same amount of smoothness, completely failing to capture the system dynamics. Furthermore, the relative residual error results demonstrate a rare case that a smaller residual for the static reconstruction at the state $\boldsymbol{x}_{456}$ does not imply a better reconstruction than the posterior KF estimate $\hat{\boldsymbol{x}}^{(1)}_{456|456}$ as seen in the resulting reconstructed images.

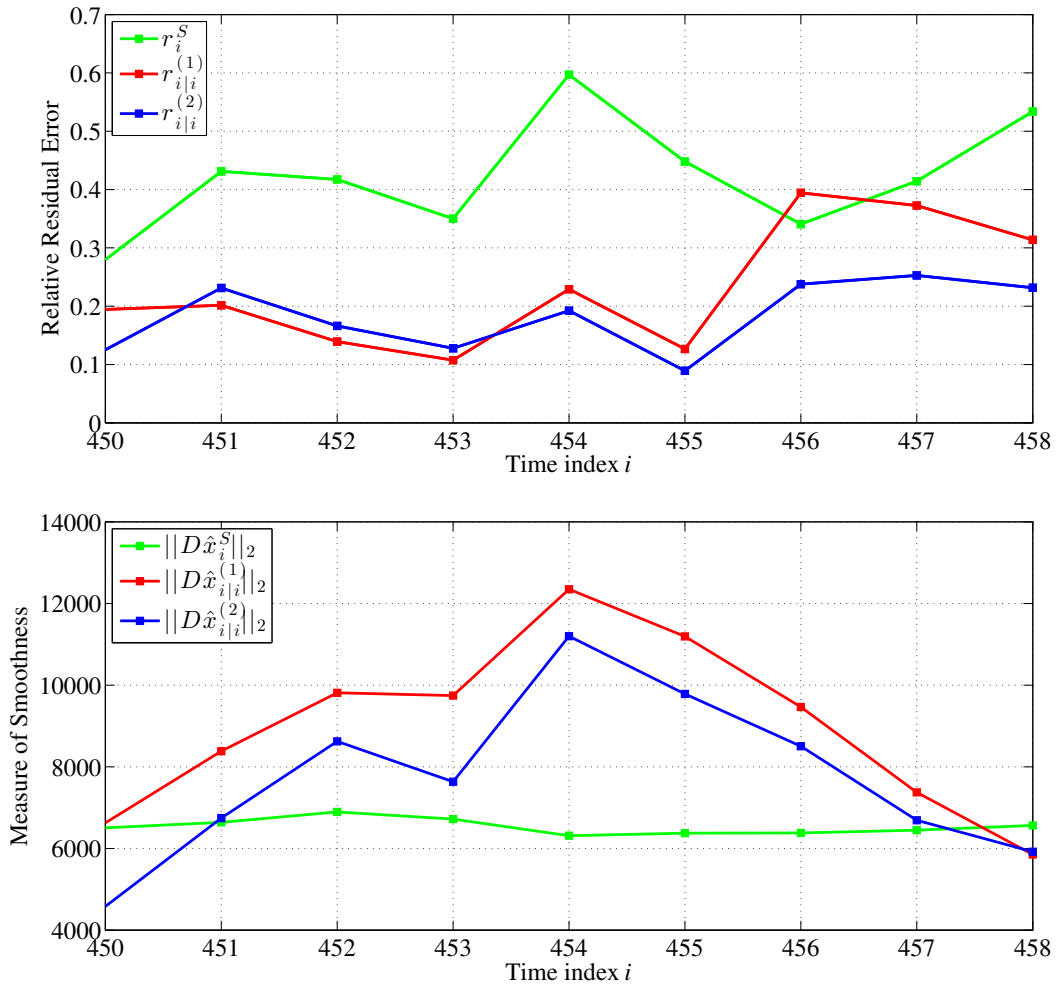

Figure 5.11: The comparison of the relative residual error (top) and the measure of smoothness (bottom) between $\hat{\boldsymbol{x}}_i^S$, $\hat{\boldsymbol{x}}_{i|i}^{(1)}$ and $\hat{\boldsymbol{x}}_{i|i}^{(2)}$ during the event of the hair dryer with the right-tilted concentrator initially positioned at 35.5 cm moving along the region between its original position and the whisker array between the states $\boldsymbol{x}_{450}$ and $\boldsymbol{x}_{458}$.

The second case investigates the tracking capability of the static and dynamic tactile tomography models for the hair dryer passing before the whisker array from right to left. Figure 5.12 displays the tactile tomographic imaging results between the states $\boldsymbol{x}_{508}$ and $\boldsymbol{x}_{518}$. The results for the relative residual error and the measure of smoothness are also given in Figure 5.13.

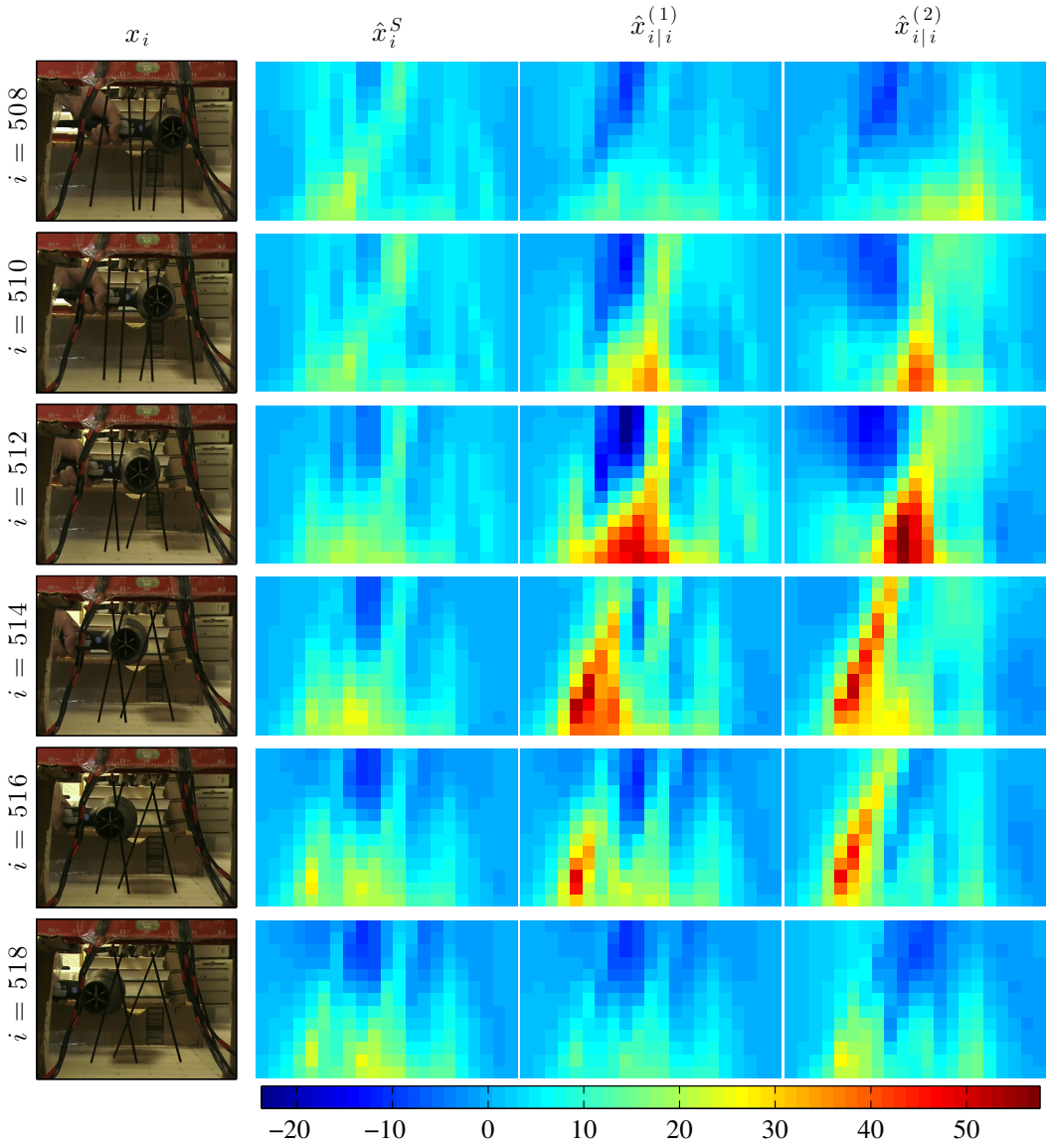

Figure 5.12: The dynamic tactile tomographic imaging results for the estimates $\hat{\boldsymbol{x}}_i^S$, $\hat{\boldsymbol{x}}_{i|i}^{(1)}$ and $\hat{\boldsymbol{x}}_{i|i}^{(2)}$ during the event of the hair dryer passing before the whisker array from right to left between the states $\boldsymbol{x}_{508}$ and $\boldsymbol{x}_{518}$.

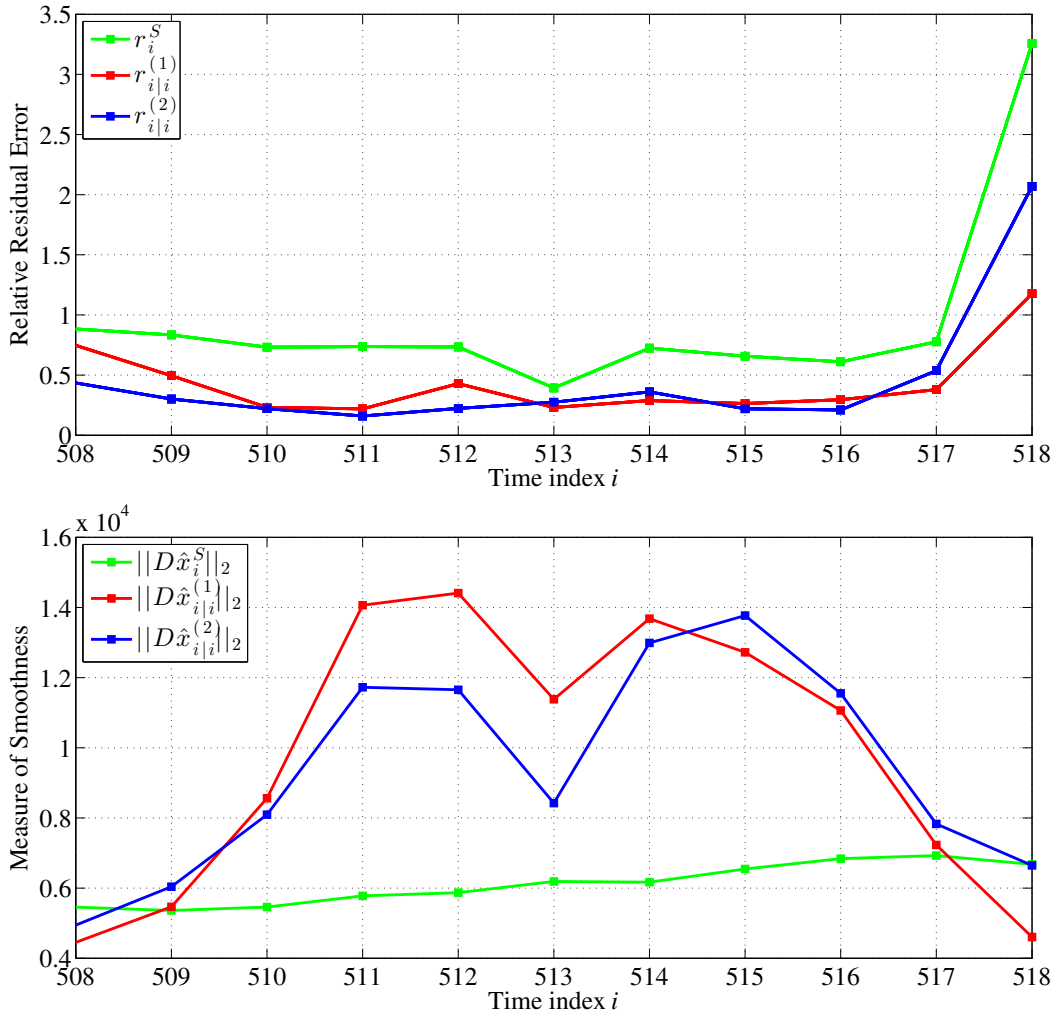

Figure 5.13: The comparison of the relative residual error (top) and the measure of smoothness (bottom) between the estimates $\hat{\boldsymbol{x}}_i^S$, $\hat{\boldsymbol{x}}_{i|i}^{(1)}$ and $\hat{\boldsymbol{x}}_{i|i}^{(2)}$ during the event of the hair dryer passing right before the whisker array from right to left between the states $\boldsymbol{x}_{508}$ and $\boldsymbol{x}_{518}$.

The first observation based on all the resulting images is that the overall reconstruction quality is not as good as the previous cases due to the hair dryer moving too closely to the whisker array, that is spatially very sparse. Therefore, in most of the cases, all the three models fail to capture the round shape of the flow pattern generated by the hair dryer due to the spatial sparseness of the whisker array and also possibly the hair dryer moving too fast to

capture the system evolution for the whisker array. However, it is still possible to keep track of the right-to-left movement of the hair dryer in the dynamic reconstructions as it starts at the location right to the first whisker in the array and then moves in a leftward direction captured by the whisker array between the states $\boldsymbol{x}_{510}$ and $\boldsymbol{x}_{516}$, and eventually becomes out of sight beginning at the state $\boldsymbol{x}_{518}$. This moving pattern can also be noticed in the smoothness level of the dynamic reconstructions as a continuos rise followed by a gradual decrease as the hair dryer moves out of the area, which in turn is observed as a sudden increase in the relative residual at the final state $\boldsymbol{x}_{518}$. Once again, nothing can be inferred from the static reconstructions, except the potential presence of a flow source.

5.4.4 The Tracking of a Moving Object

The last four cases investigate the ability of the static and dynamic tactile tomographic model to track moving objects under a fixed flow source.

The first case is the tracking of a rectangular-shaped red box passing between the whisker array and the hair dryer located at 19.5 cm as shown in Figure 5.14. The relative residual error and the measure of smoothness results are also presented in Figure 5.15. As expected, when the red box begins to gradually block the hair dryer, the images in the dynamic reconstructions gradually diminish to nearly all-zero images, and then come back with the release of the hair dryer.

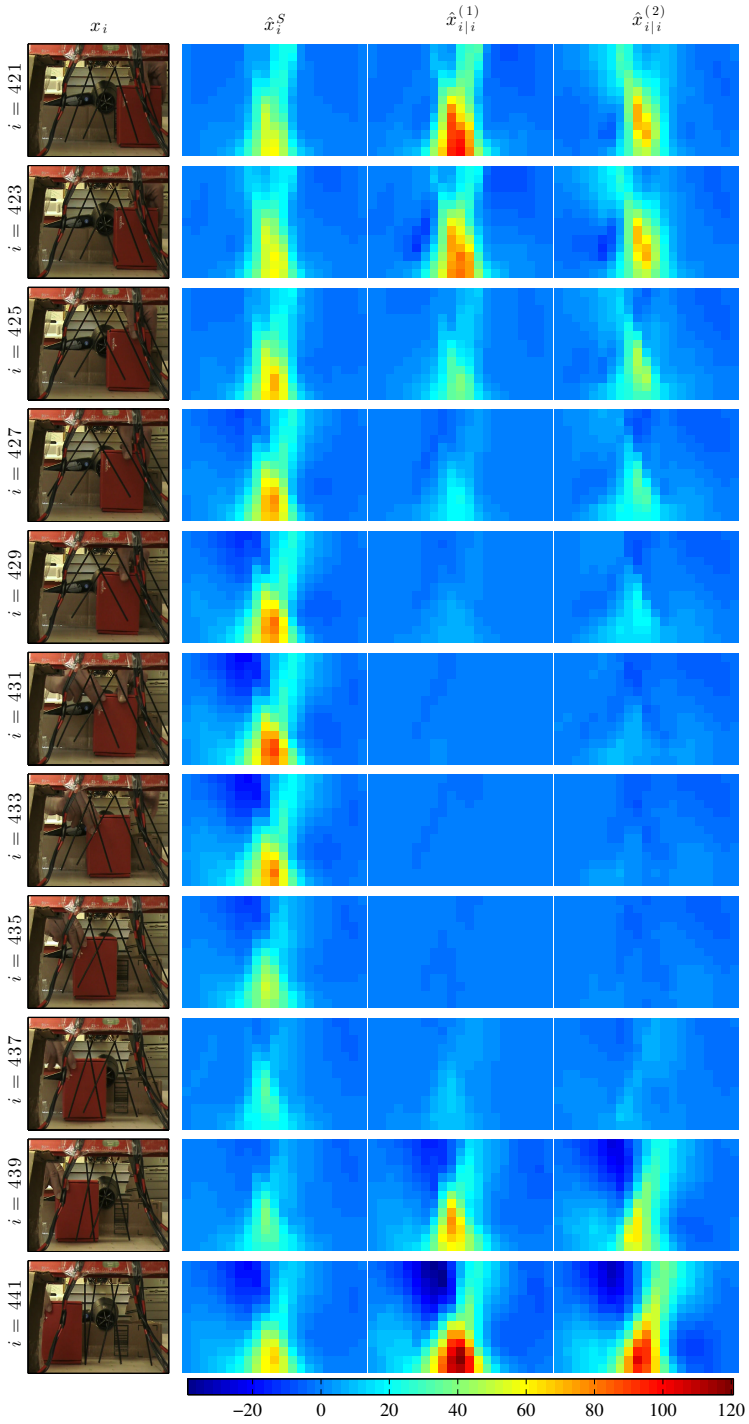

Figure 5.14: The dynamic tactile tomographic imaging results for the estimates $\hat{\boldsymbol{x}}_i^S$, $\hat{\boldsymbol{x}}_{i|i}^{(1)}$ and $\hat{\boldsymbol{x}}_{i|i}^{(2)}$ during the event of the rectangular-shaped red box passing between the whisker array and the hair dryer positioned at 19.5 cm between the states $\boldsymbol{x}_{421}$ and $\boldsymbol{x}_{441}$.

The entire event is also noticeable in the relative residual error for the static reconstruction, as it gradually increases until the blocking is complete and reduces as the red box gradually releases the hair dryer, which in turn is observed as the long deep notch in the smoothness level of the two dynamic reconstructions. The delay in the response of the static estimates to the dynamic evolution is also clearly seen in the static smoothness level.

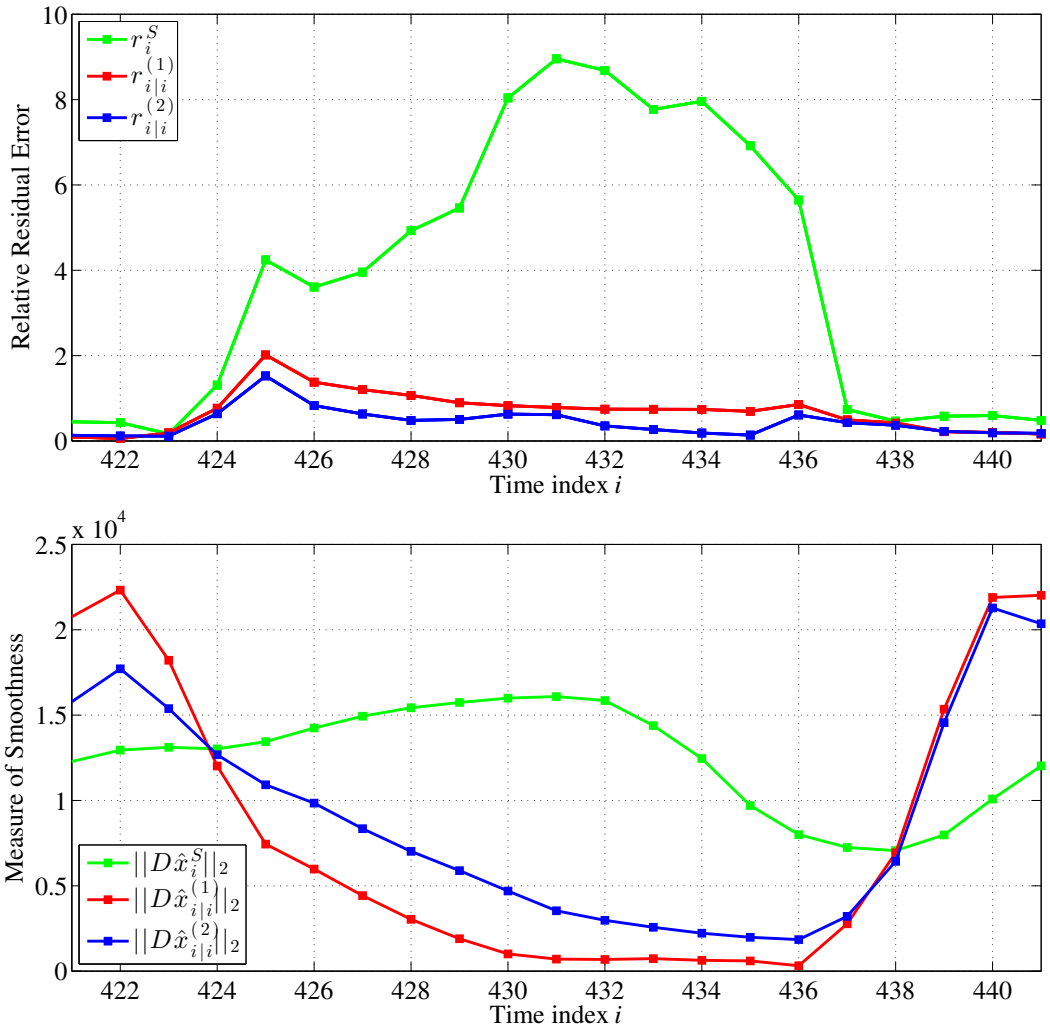

Figure 5.15: The comparison of the relative residual error (top) and the measure of smoothness (bottom) between the estimates $\hat{\boldsymbol{x}}_i^S$, $\hat{\boldsymbol{x}}_{i|i}^{(1)}$ and $\hat{\boldsymbol{x}}_{i|i}^{(2)}$ during the event of the rectangular-shaped red box passing between the whisker array and the hair dryer positioned at 19.5 cm between the states $\boldsymbol{x}_{421}$ and $\boldsymbol{x}_{441}$.

Another situation of interest is the detection of a moving object before the actual touch, which is analyzed in the next two cases. The first object tracking example is when a rectangular-shaped bottle initially blocking the hair dryer located at 60.5 cm slowly approaches the whisker array and then moves back to its initial position right in front of the hair dryer. Figure 5.16 displays the static and dynamic imaging results between the states $\boldsymbol{x}_{470}$ and $\boldsymbol{x}_{506}$. The corresponding relative residual error and the measure of smoothness results are also presented in Figure 5.17. As clearly seen in the resulting images, after the bottle leaves its original position, the velocity-squared distribution estimated through the whisker array slowly gets strengthened with the bottle getting closer to the whisker array, since the streamlines become denser in front of the moving object. On the contrary, as the bottle begins to move back to its initial position, the velocity-squared distribution gradually fades away. In the final states, the bottle leaves the scene, as observed in the final images detecting the round shape of the flow generated by the hair dryer. It is also apparent that the two KF estimation techniques yield quite different results, since the first KF estimate $\hat{\boldsymbol{x}}_{i|i}^{(1)}$ is significantly constrained by the static estimates in this case, whereas the second KF estimate $\hat{\boldsymbol{x}}_{i|i}^{(2)}$ generated using the augmented forward model is not.

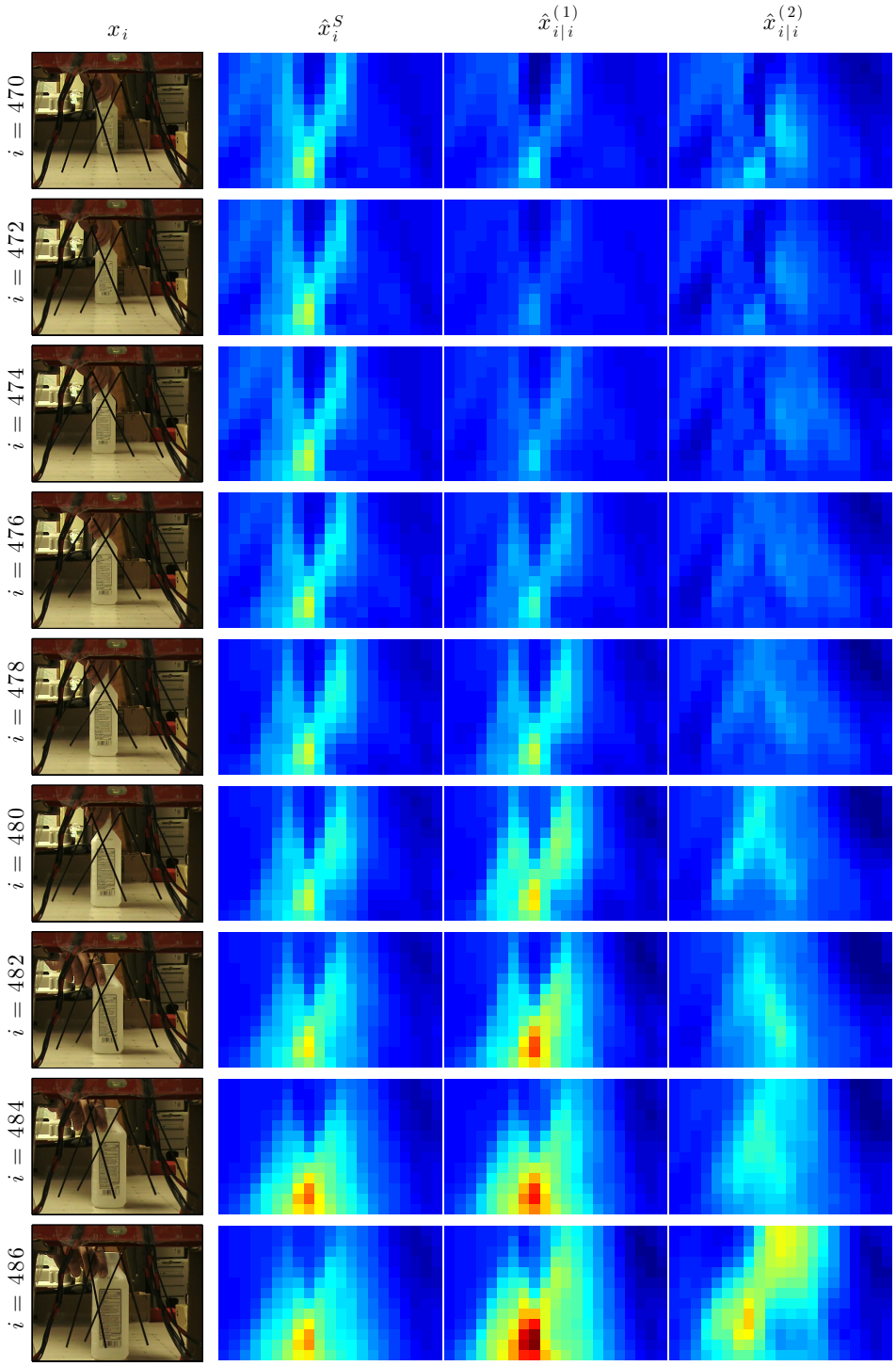

Figure 5.16: The dynamic tactile tomographic imaging results for the estimates $\hat{\boldsymbol{x}}_i^S$, $\hat{\boldsymbol{x}}_{i|i}^{(1)}$ and $\hat{\boldsymbol{x}}_{i|i}^{(2)}$ during the event of the rectangular-shaped bottle moving toward the whisker array and then back to the hair dryer positioned at 60.5 cm between the states $\boldsymbol{x}_{470}$ and $\boldsymbol{x}_{506}$.

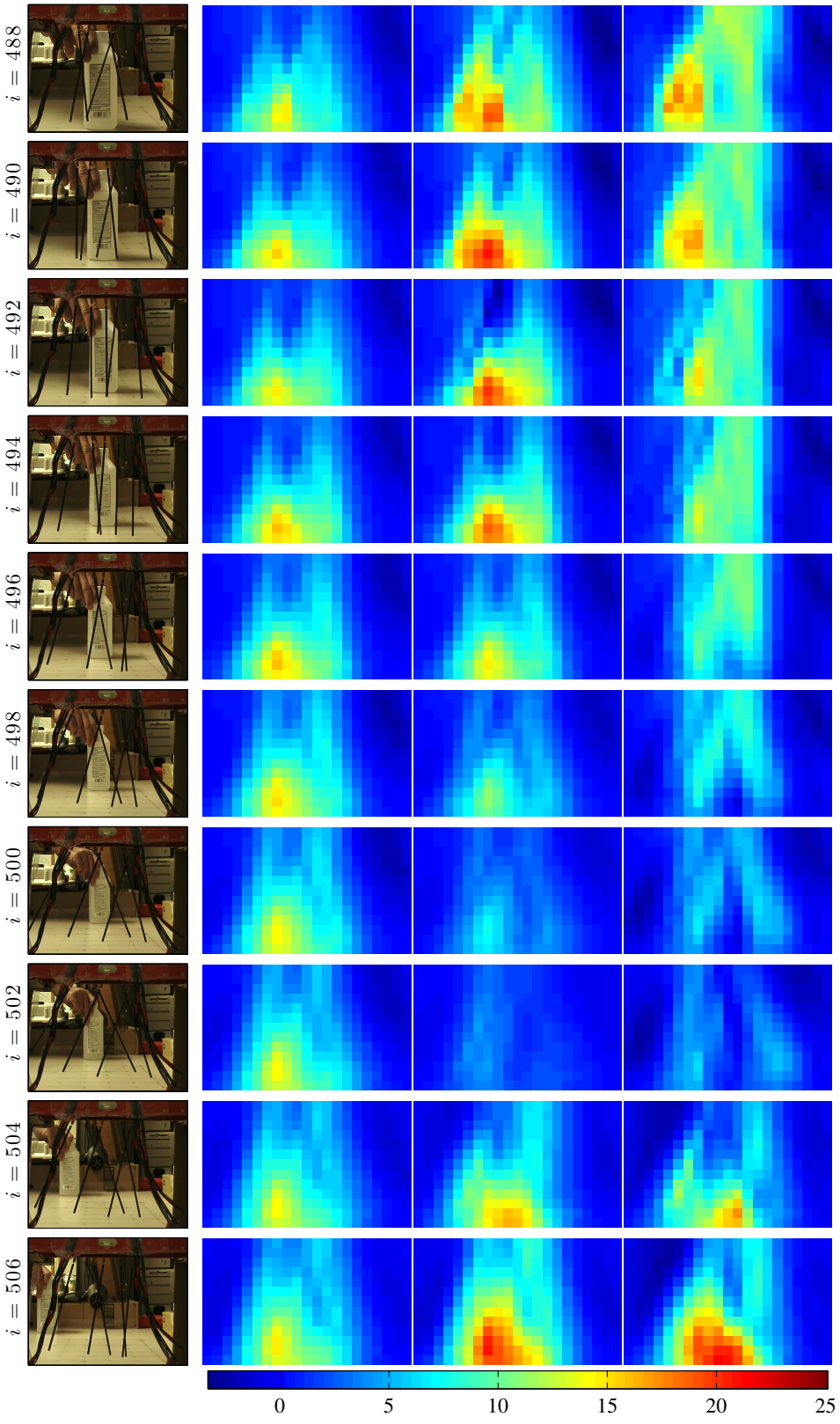

Figure 5.16 (cont.).

The flow pattern generated by the moving bottle can also be traced along the static residual error, as the peaks correspond to the complete blocking of the hair dryer and the gradual rise and decrease between the two peaks indicate the moving pattern of the rectangular-shaped bottle. The same observation can be made by analyzing the oscillatory behavior in the smoothness level of the two dynamic reconstructions.

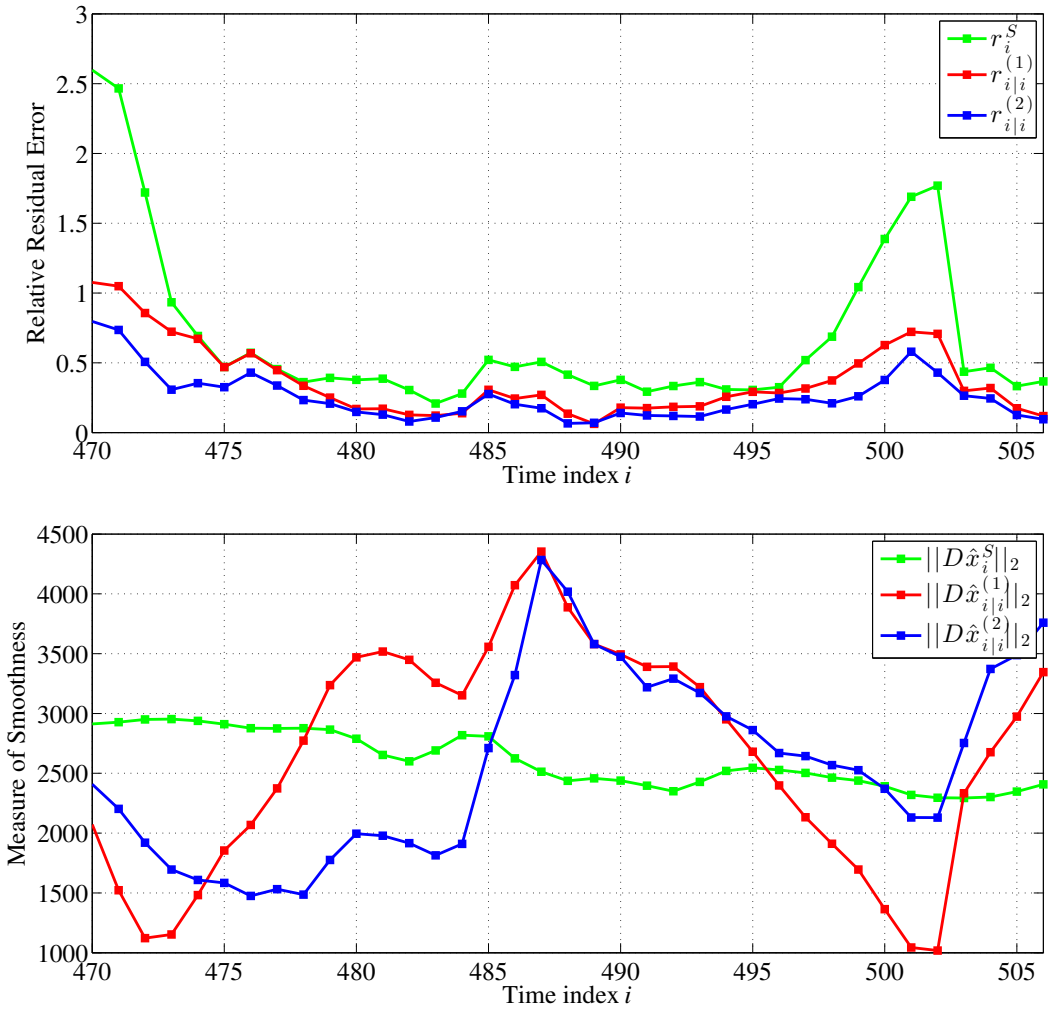

Figure 5.17: The comparison of the relative residual error (top) and the measure of smoothness (bottom) between the estimates $\hat{\boldsymbol{x}}_i^S$, $\hat{\boldsymbol{x}}_{i|i}^{(1)}$ and $\hat{\boldsymbol{x}}_{i|i}^{(2)}$ during the event of the rectangular-shaped bottle moving toward the whisker array and then back to the hair dryer positioned at 60.5 cm the states $\boldsymbol{x}_{470}$ and $\boldsymbol{x}_{506}$.

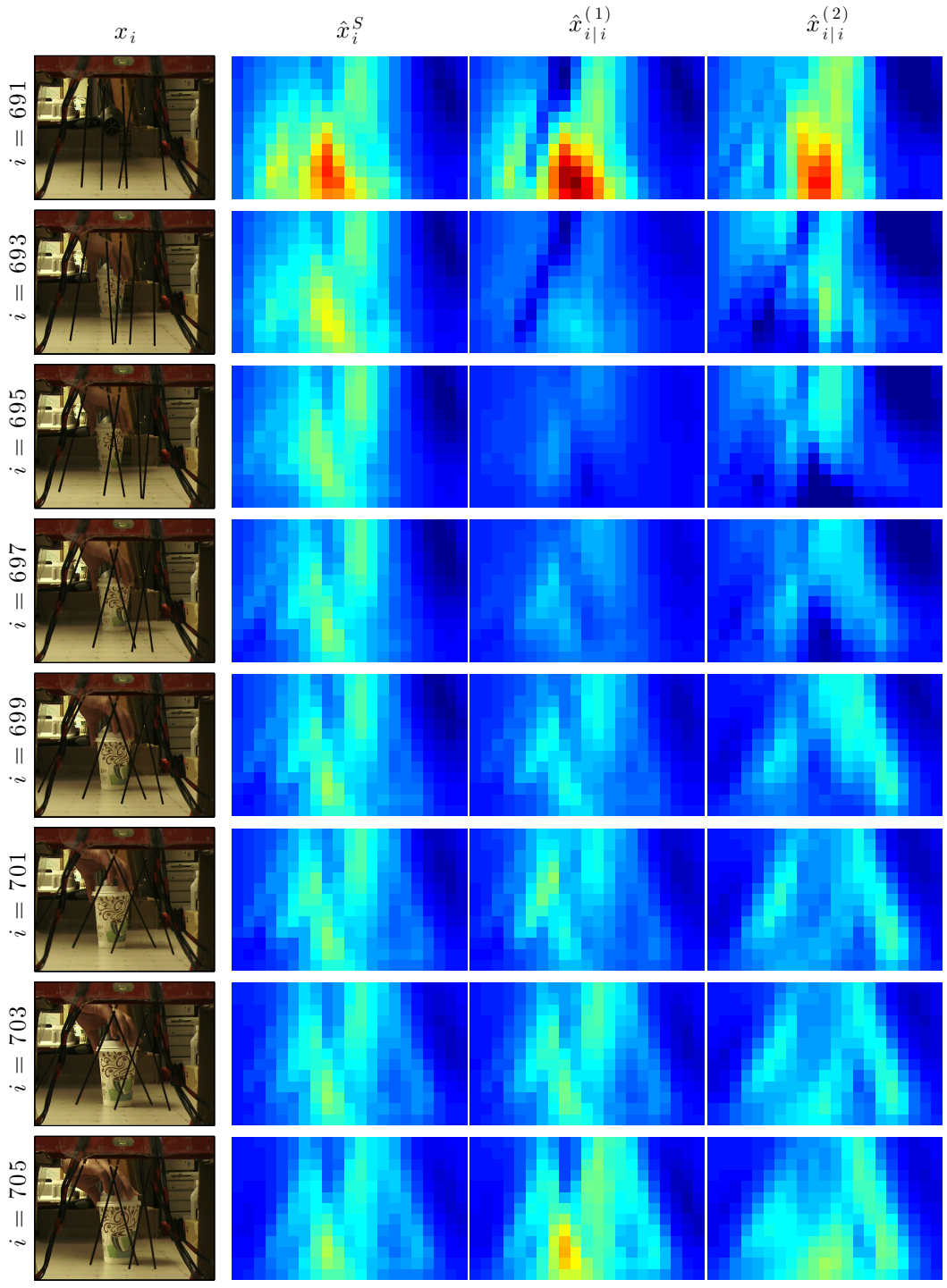

Figure 5.18: The dynamic tactile tomographic imaging results for the estimates $\hat{\boldsymbol{x}}_i^S$, $\hat{\boldsymbol{x}}_{i|i}^{(1)}$ and $\hat{\boldsymbol{x}}_{i|i}^{(2)}$ during the event of the paper coffee cup moving away from the hair dryer positioned at 60.5 cm toward the whisker array and then leaving the coverage area after getting very close to the whisker array between the states $\boldsymbol{x}_{691}$ and $\boldsymbol{x}_{719}$.

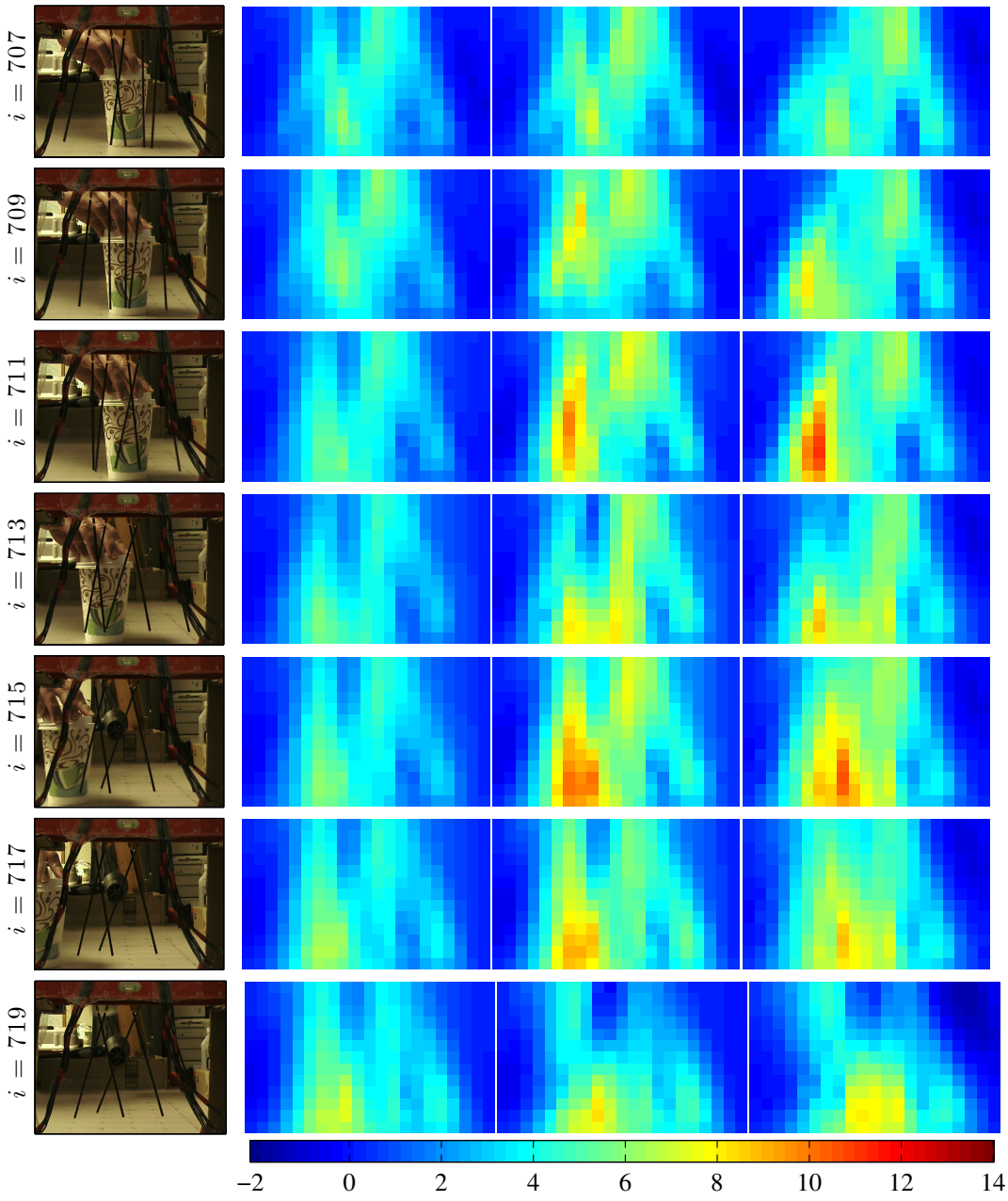

Figure 5.18 (cont.).

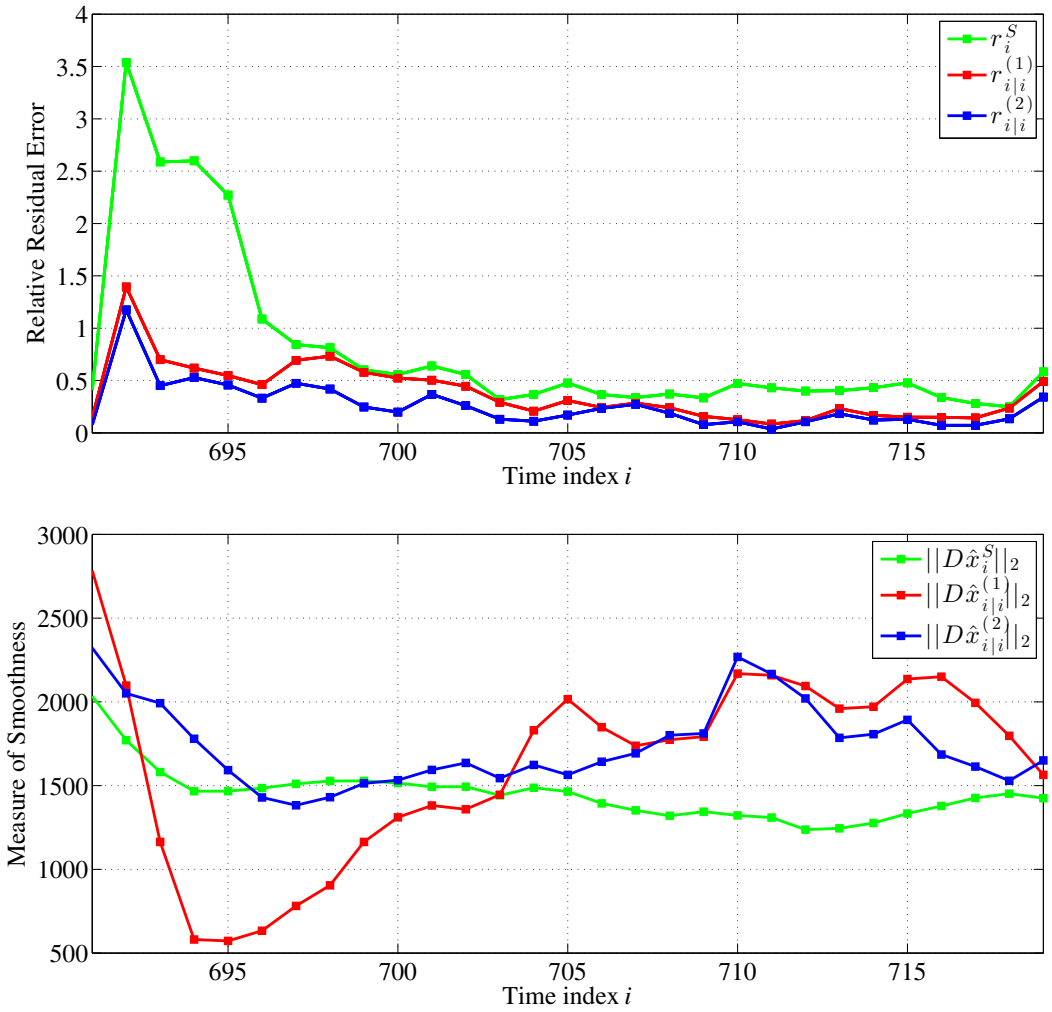

Figure 5.19: The comparison of the relative residual error (top) and the measure of smoothness (bottom) between the estimates $\hat{\boldsymbol{x}}_i^S$, $\hat{\boldsymbol{x}}_{i|i}^{(1)}$ and $\hat{\boldsymbol{x}}_{i|i}^{(2)}$ during the event of the paper coffee cup moving away from the hair dryer positioned at 60.5 cm toward the whisker array and then leaving the coverage area after getting very close to the whisker array between the states $\boldsymbol{x}_{691}$ and $\boldsymbol{x}_{719}$.

The second case involves the paper coffee cup abruptly blocking the hair dryer positioned at 60.5 cm, moving toward the whisker array, and leaving the scene after getting very close to the whisker array. The static and dynamic imaging results are presented in Figure 5.18 along with the resulting relative residual error and the measure of smoothness in Figure 5.19. Similar to the

first case, the presence of the paper cup becomes much more noticeable as it gets closer to the whisker array in the dynamic reconstructions.

The sudden jump in the static relative residual error corresponds to the abrupt block of the hair dryer by the paper cup, whereas the deep notch and the gradual increase in the smoothness level of the dynamic reconstructions describe the movement of the paper cup toward the whisker array. However, in all three cases, it is not possible to distinguish between the presence of an object close to the whisker array and a flow source, possibly due to the detected signal being very weak, since the hair dryer was located quite far from the whisker array.

The final case is the tracking of an object randomly moving between the air-flow source and the whisker array as shown in Figure 5.20 for the moving plastic water bottle with the hair dryer as the flow source fixed at 35.5 cm. The corresponding relative error residuals and the measure of smoothness are given in Figure 5.21. In this case, the plastic water bottle zigzags while approaching the whisker array blocking the hair dryer at times, as detected by the dynamic reconstructions. The large relative residual errors in the static reconstructions once again denote the abrupt blocking, and the oscillations in the dynamic smoothness level correspond to the dynamic behavior of the moving plastic water bottle.

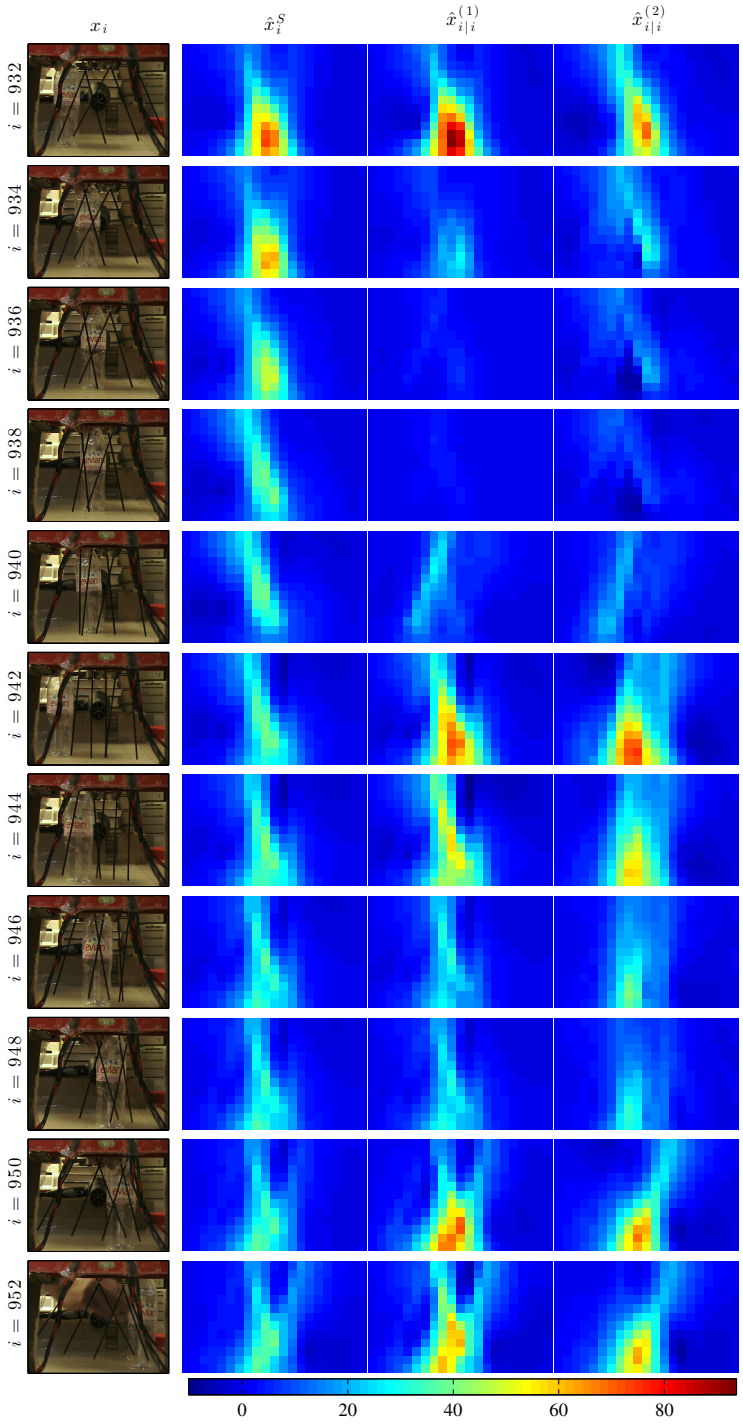

Figure 5.20: The dynamic tactile tomographic imaging results for the estimates $\hat{\boldsymbol{x}}_i^S$, $\hat{\boldsymbol{x}}_{i|i}^{(1)}$ and $\hat{\boldsymbol{x}}_{i|i}^{(2)}$ during the event of the plastic water bottle zigzagging between the whisker array and the hair dryer located at 35.5 cm and while approaching the whisker array between the states $\boldsymbol{x}_{932}$ and $\boldsymbol{x}_{952}$.

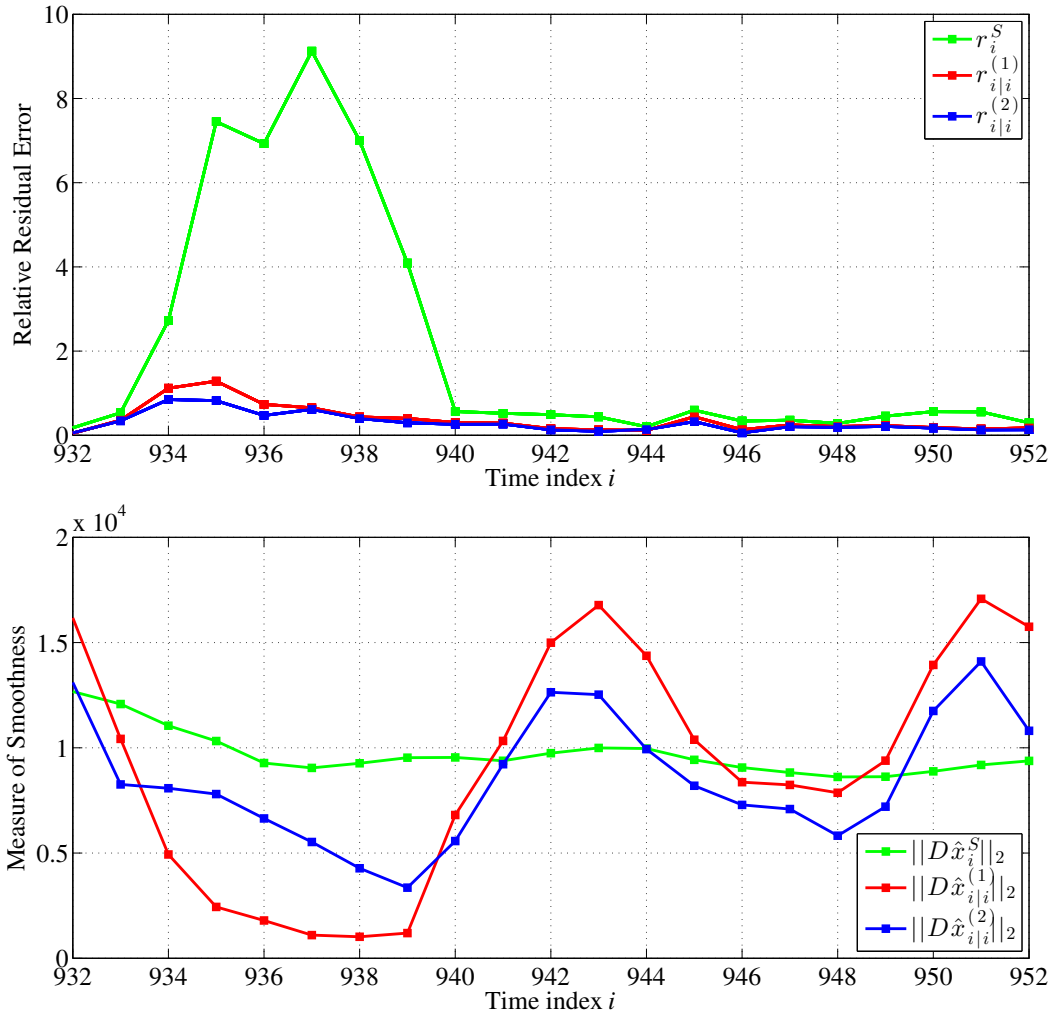

Figure 5.21: The comparison of the relative residual error (top) and the measure of smoothness (bottom) between the estimates $\hat{\boldsymbol{x}}_i^S$, $\hat{\boldsymbol{x}}_{i|i}^{(1)}$ and $\hat{\boldsymbol{x}}_{i|i}^{(2)}$ during the event of the plastic water bottle zigzagging between the whisker array and the hair dryer located at 35.5 cm and while approaching the whisker array between the states $\boldsymbol{x}_{932}$ and $\boldsymbol{x}_{952}$.

5.5 Dynamic Tactile Underwater Flow Imaging

There are four cases selected from the two sets of underwater experiments performed at the distances of 28.7 cm and 44.7 cm away from the whisker ar-

ray, such as the detection of a time-varying flow-source direction and velocity, and the tracking a moving object under turbulent flow. The static regularization parameter was set to be $\lambda_S = 3 \times 10^{-9}$ and the dynamic regularization parameter $\lambda_D = 2 \times 10^{-7}$ for both of the two sets of experiments.

5.5.1 The Detection of the Time-Varying Flow-Source Velocity

The first case considered in underwater experiments is the detection of the fixed flow source with its velocity significantly changing in time, ranging from laminar to turbulent flow. Figure 5.22 illustrates the imaging results produced by the measured data collected by the whisker array at 28.7 cm away from the hose exit, regarding the circulating flow generated by the water pump at time-varying flow rates between the states $\boldsymbol{x}_{31}$ and $\boldsymbol{x}_{82}$. Figure 5.23 shows the comparison of the corresponding relative residual error and measure of smoothness between the estimates $\hat{\boldsymbol{x}}_i^S$, $\hat{\boldsymbol{x}}_{i|i}^{(1)}$ and $\hat{\boldsymbol{x}}_{i|i}^{(2)}$ for the states $\boldsymbol{x}_{31}$ through $\boldsymbol{x}_{82}$.

The flow pattern can be described as the water pump starting to operate at a very low flow rate and then gradually increasing the flow speed until the circulating flow becomes very turbulent around the state $\boldsymbol{x}_{55}$. After that point, the flow rate is reduced until there was no significant flow around the state $\boldsymbol{x}_{70}$. As a final examination, the flow rate is suddenly increased and then immediately reduced between the states $\boldsymbol{x}_{70}$ and $\boldsymbol{x}_{82}$. The dynamic reconstruction results indicate that the dynamic KF estimates successfully captures the system evolution in all the situations. On the other hand, the static reconstructions also yield somewhat satisfactory results during which the flow rate is increased quite slowly, whereas when the flow rate varies rapidly, the static

case fails to follow the dynamically changing flow pattern as it is noticeable in the static relative residual error, in which the residual suddenly increases as the flow rate goes down near zero around the state $\boldsymbol{x}_{70}$. On the contrary, the variations in the flow rate can be observed as the oscillations in the dynamic smoothness levels, evidently showing that the dynamic reconstructions are able to keep track of the dynamic changes in flow speed.

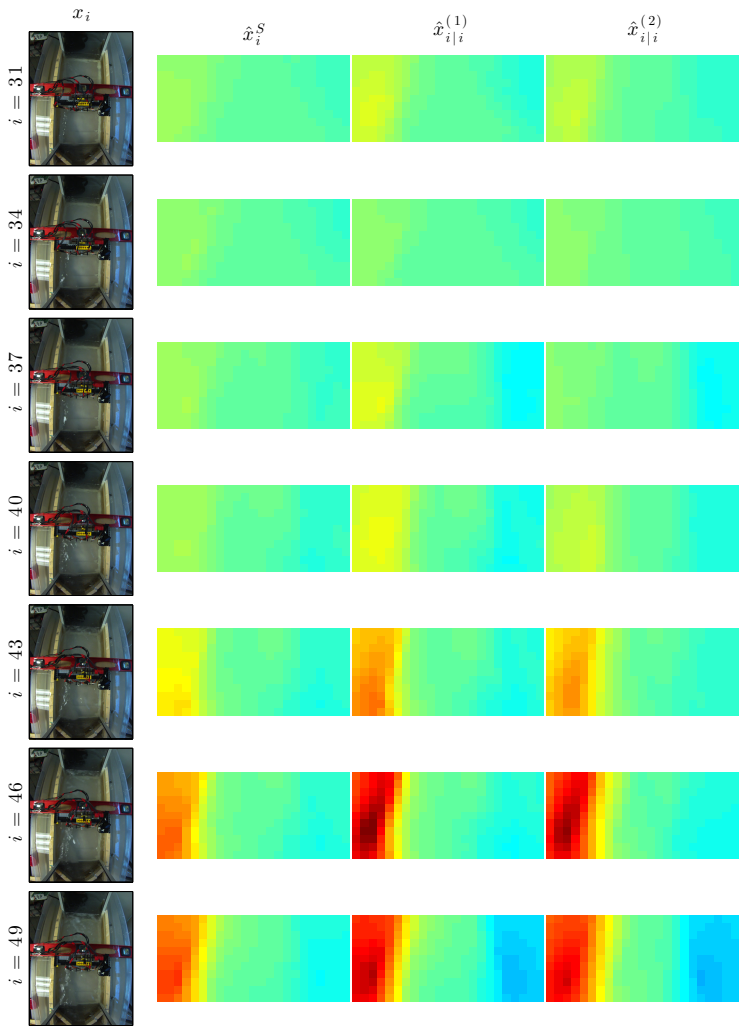

Figure 5.22: The dynamic tactile tomographic imaging results for the estimates $\hat{\boldsymbol{x}}_i^S$, $\hat{\boldsymbol{x}}_{i|i}^{(1)}$ and $\hat{\boldsymbol{x}}_{i|i}^{(2)}$ during which the rate of the water flow generated by the pump varies in time ranging from laminar to turbulent flow between the states $\boldsymbol{x}_{31}$ and $\boldsymbol{x}_{82}$: The whisker array is positioned at 28.7 cm away from the hose exit.

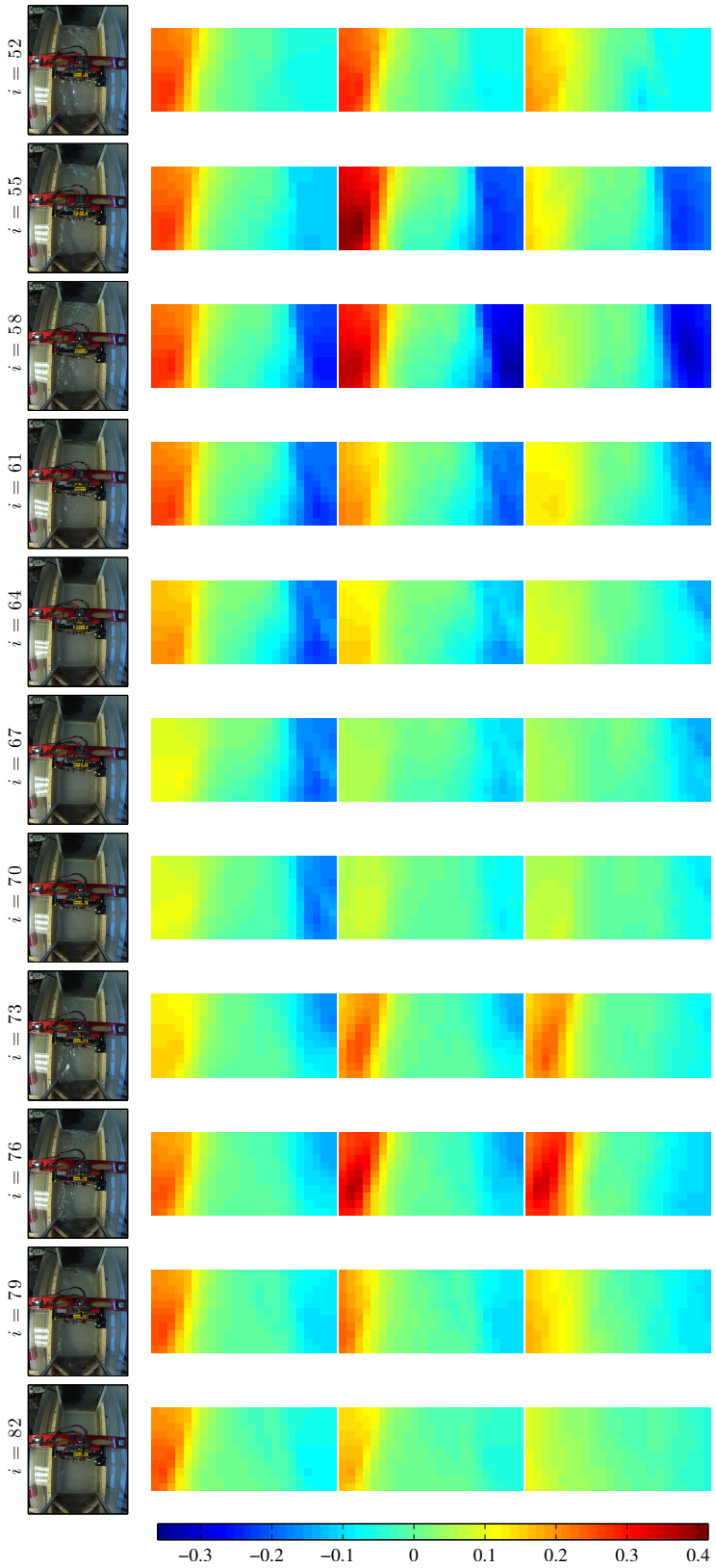

Figure 5.22 (cont.).

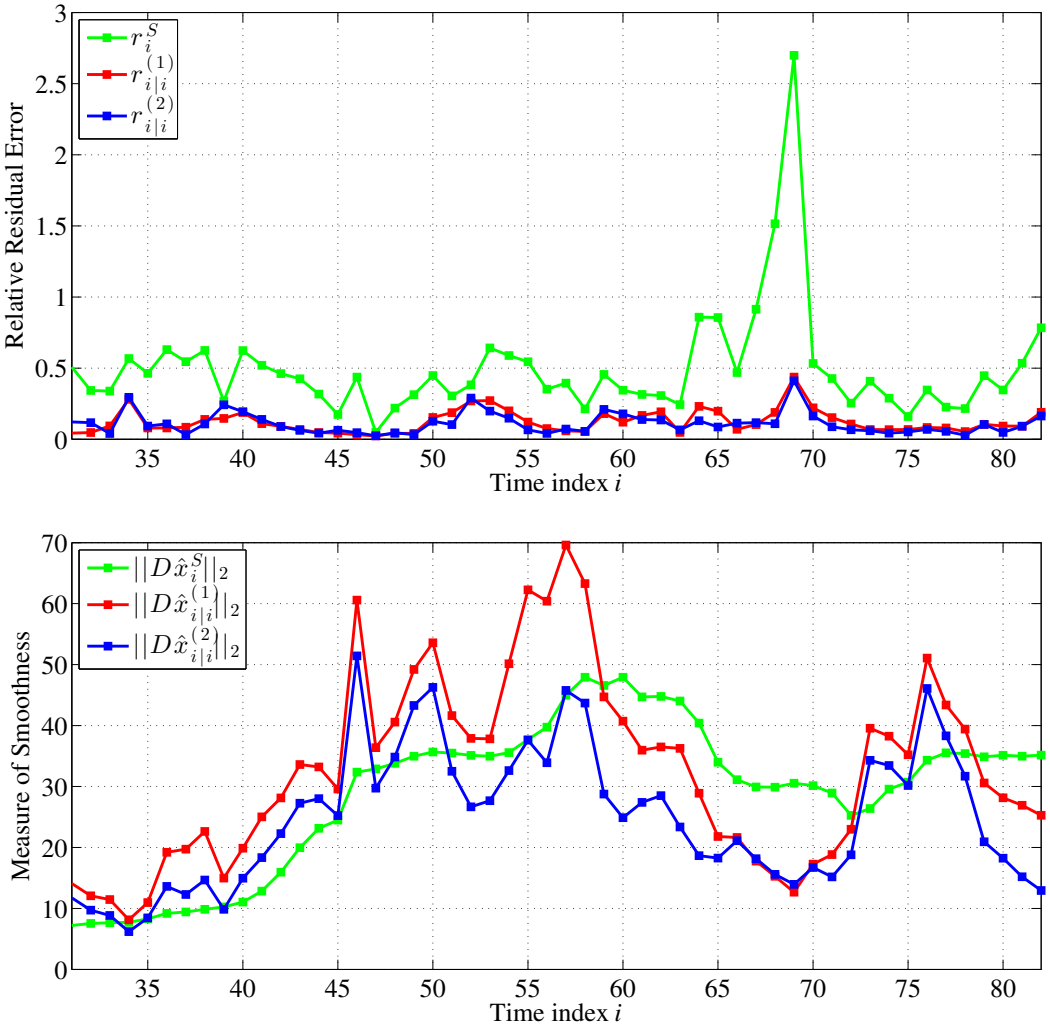

Figure 5.23: The comparison of the relative residual error (top) and the measure of smoothness (bottom) between the estimates $\hat{\boldsymbol{x}}_i^S$, $\hat{\boldsymbol{x}}_{i|i}^{(1)}$ and $\hat{\boldsymbol{x}}_{i|i}^{(2)}$ during which the rate of the water flow generated by the pump varies in time ranging from laminar to turbulent flow between the states $\boldsymbol{x}_{31}$ and $\boldsymbol{x}_{82}$: The whisker array is positioned at 28.7 cm away from the hose exit.

5.5.2 The Tracking of a Time-Varying Flow-Source Direction

The second case investigates the ability to capture the turbulent flow dynamics when the flow-source direction changes over time. Figure 5.24 displays the static and dynamic tactile tomographic imaging results based on the measure-

ments collected by the whisker array positioned at 44.7 cm from the hose exit during which the direction of the water flow generated by the pump varies over time between the states $\boldsymbol{x}_{586}$ and $\boldsymbol{x}_{610}$. The resulting relative residual error and the measure of smoothness are presented in Figure 5.25.

In the beginning, the flow rate gradually increases as seen in the first couple of frames, and then the flow starts to change direction, resulting in a very low-rate flow sensed by the whisker array as seen in the dynamic reconstructions between the states $\boldsymbol{x}_{598}$ and $\boldsymbol{x}_{604}$, since it takes some time for the turbulent flow to reach the whiskers while changing direction, as the rotational flow right before the whiskers is clearly observable between the image frames $\boldsymbol{x}_{598}$ and $\boldsymbol{x}_{604}$. Beginning with the state $\boldsymbol{x}_{605}$, the circulating flow switches directions as the positive flow is seen near the right wooden wall. In the final state $\boldsymbol{x}_{610}$, the positive flow diminishes as the hose exit is almost blocked by the wooden stick used to change the flow pattern.

The incapability of the static reconstructions in capturing the system dynamics is also indicated by the relative residual error results, in which the peak at the state $\boldsymbol{x}_{597}$ corresponds to the time when the flow direction begins to change, and it takes until the final state $\boldsymbol{x}_{610}$ to finally catch up with the current flow pattern. By comparison, the directional changes in the flow pattern can be traced through the dynamic smoothness levels as seen in Figure 5.25, where the peak at $\boldsymbol{x}_{607}$ matches the time when the positive flow is completely rotated toward the right wooden wall before the partial blocking of the hose by the wooden stick.

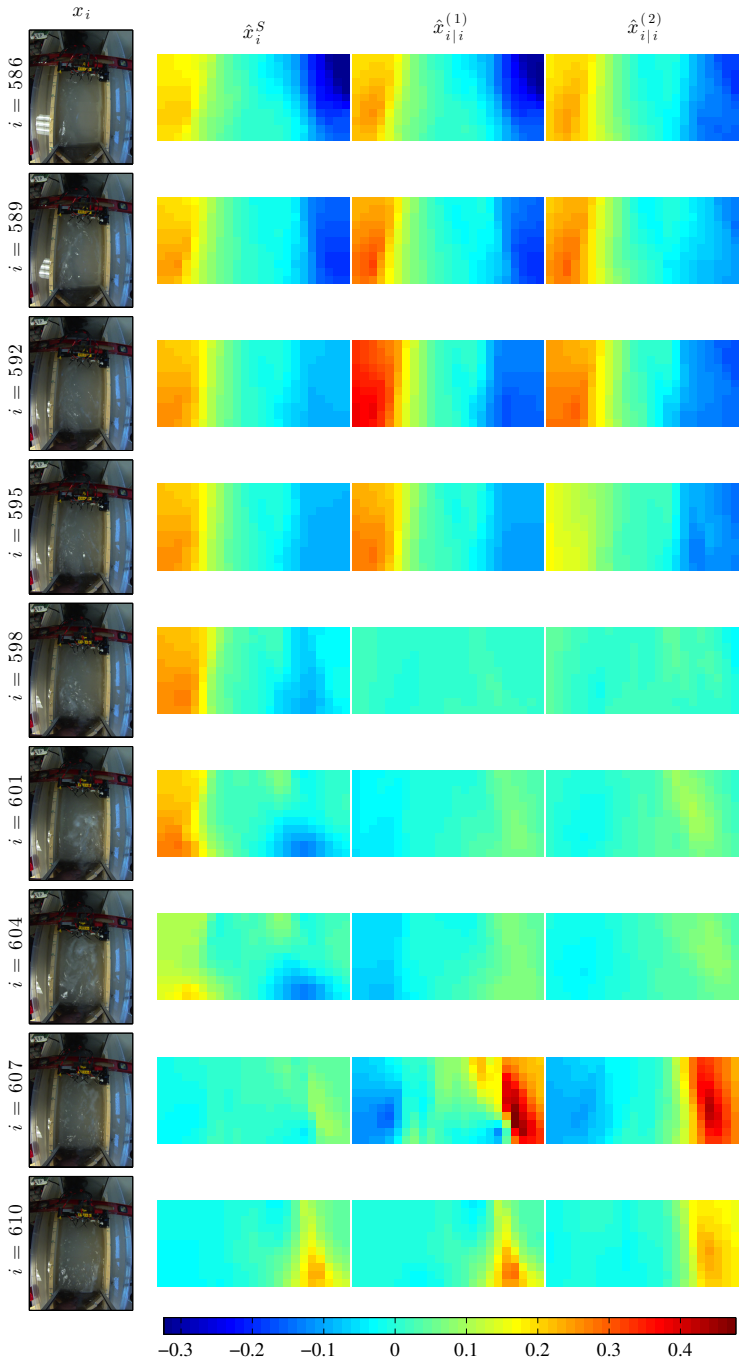

Figure 5.24: The dynamic tactile tomographic imaging results for the estimates $\hat{\boldsymbol{x}}_i^S$, $\hat{\boldsymbol{x}}_{i|i}^{(1)}$ and $\hat{\boldsymbol{x}}_{i|i}^{(2)}$ during which the direction of the water flow generated by the pump changes with time between the states $\boldsymbol{x}_{586}$ and $\boldsymbol{x}_{610}$: The whisker array is positioned at 44.7 cm away from the hose exit.

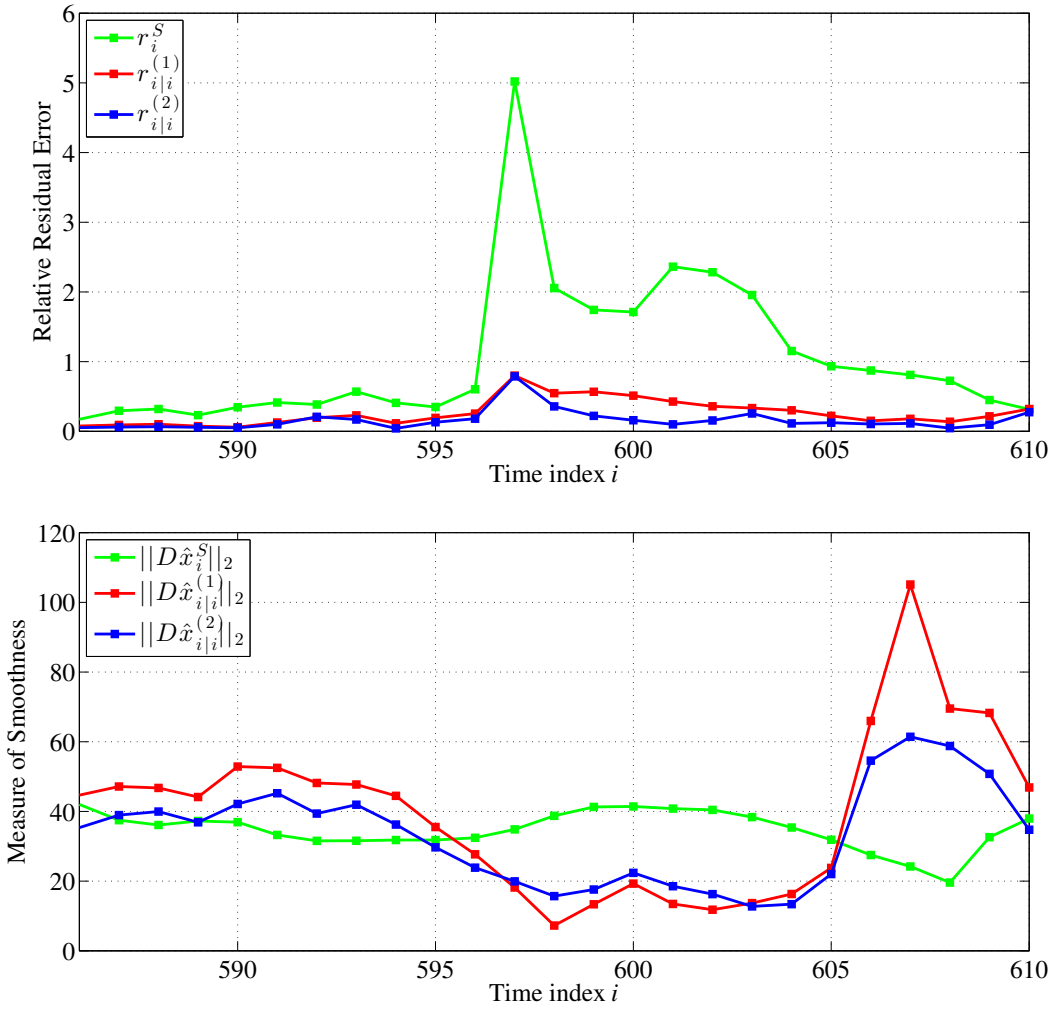

Figure 5.25: The comparison of the relative residual error (top) and the measure of smoothness (bottom) between the estimates $\hat{\boldsymbol{x}}_i^S$, $\hat{\boldsymbol{x}}_{i|i}^{(1)}$ and $\hat{\boldsymbol{x}}_{i|i}^{(2)}$ during which the direction of the water flow generated by the pump changes with time: The whisker array is positioned at 44.7 cm away from the hose exit.

5.5.3 The Tracking of a Moving Object under Turbulent Flow

The next two cases involve the tracking of moving objects under turbulent flow conditions. The first case is the analysis of the changes in the cross-sectional velocity-squared distribution when a rectangular wooden plate moves away

from the whisker array positioned at 44.7 cm and approaches the screen before the hose exit as shown in Figure 5.26 between the states $\boldsymbol{x}_{259}$ and $\boldsymbol{x}_{283}$. The relative residual error and the measure of smoothness results are also given in Figure 5.27.

As seen from the dynamic reconstructions and as well as in the image frames from the camera recordings, the flow strength is significantly reduced when the wooden block is situated before the whisker array when compared with the static reconstructions still carrying information from previous states. As the wooden plate starts to move away from the whisker array, the flow direction near the left wall tends to turn backward first and then turns back to its positive direction again, which can be observed in the dynamic reconstructions with differences in the magnitude as a result of the reliance of the first KF estimate $\hat{\boldsymbol{x}}_{i|i}^{(1)}$ on the static reconstructions. One should also notice that the wooden plate is big enough to virtually block the flow behind it, causing the negative flow to almost completely diminish as the weak positive flow near both the left and right walls generated by the blocking is clearly visible in all of three cases beginning from the state $\boldsymbol{x}_{268}$.

The peak at the state $\boldsymbol{x}_{261}$ in the static relative residual error results also reveals the time instant when the flow starts to be blocked by the wooden plate. The differences in the dynamic reconstructions are also quantitatively reflected in the measure of smoothness. The overall results indicate that it is harder to track a moving object under the turbulent flow conditions.

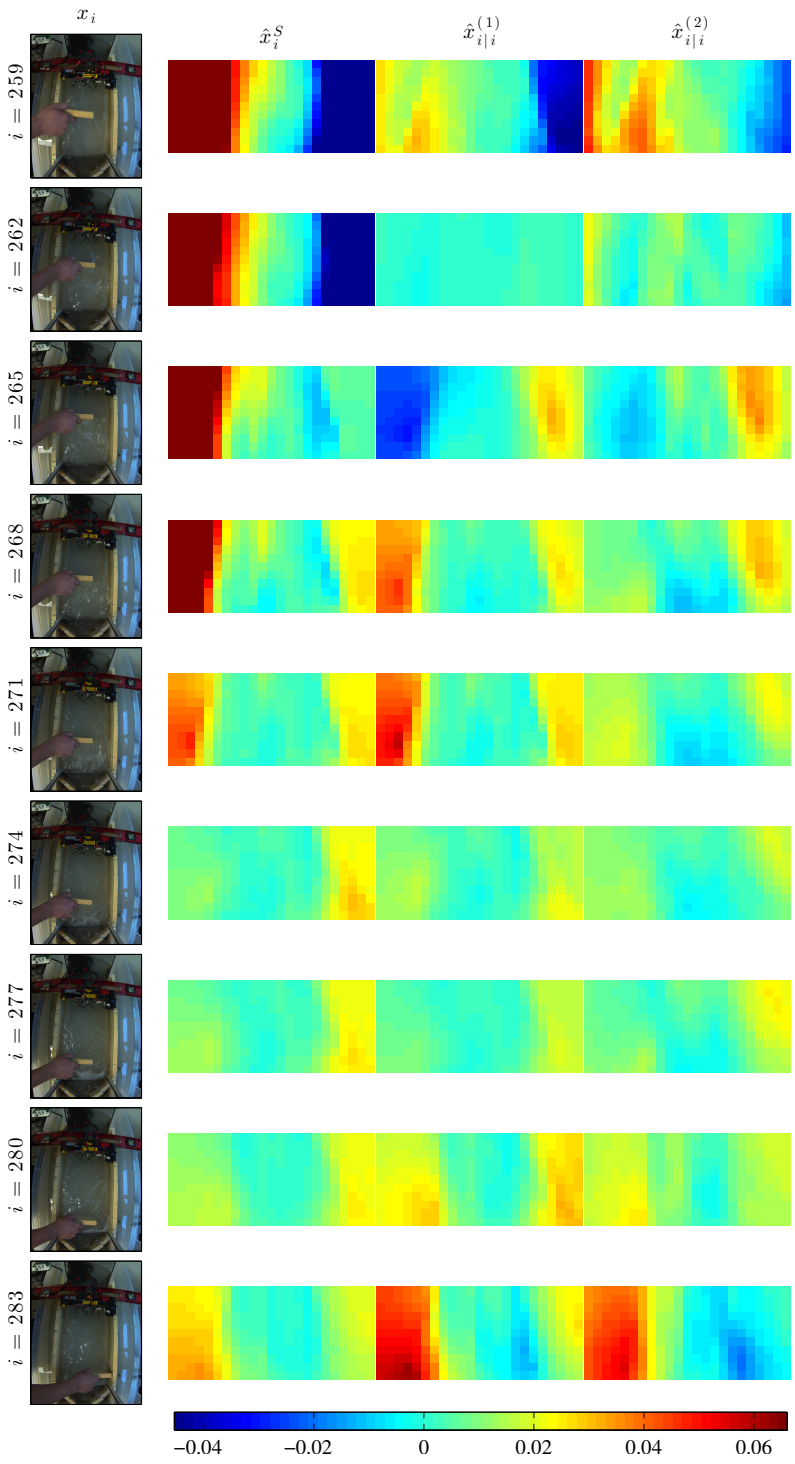

Figure 5.26: The dynamic tactile tomographic imaging results for the estimates $\hat{\boldsymbol{x}}_i^S$, $\hat{\boldsymbol{x}}_{i|i}^{(1)}$ and $\hat{\boldsymbol{x}}_{i|i}^{(2)}$ during which the rectangular wooden plate moves away from the whisker array located at 44.7 cm toward the hose exit between the states $\boldsymbol{x}_{259}$ and $\boldsymbol{x}_{283}$.

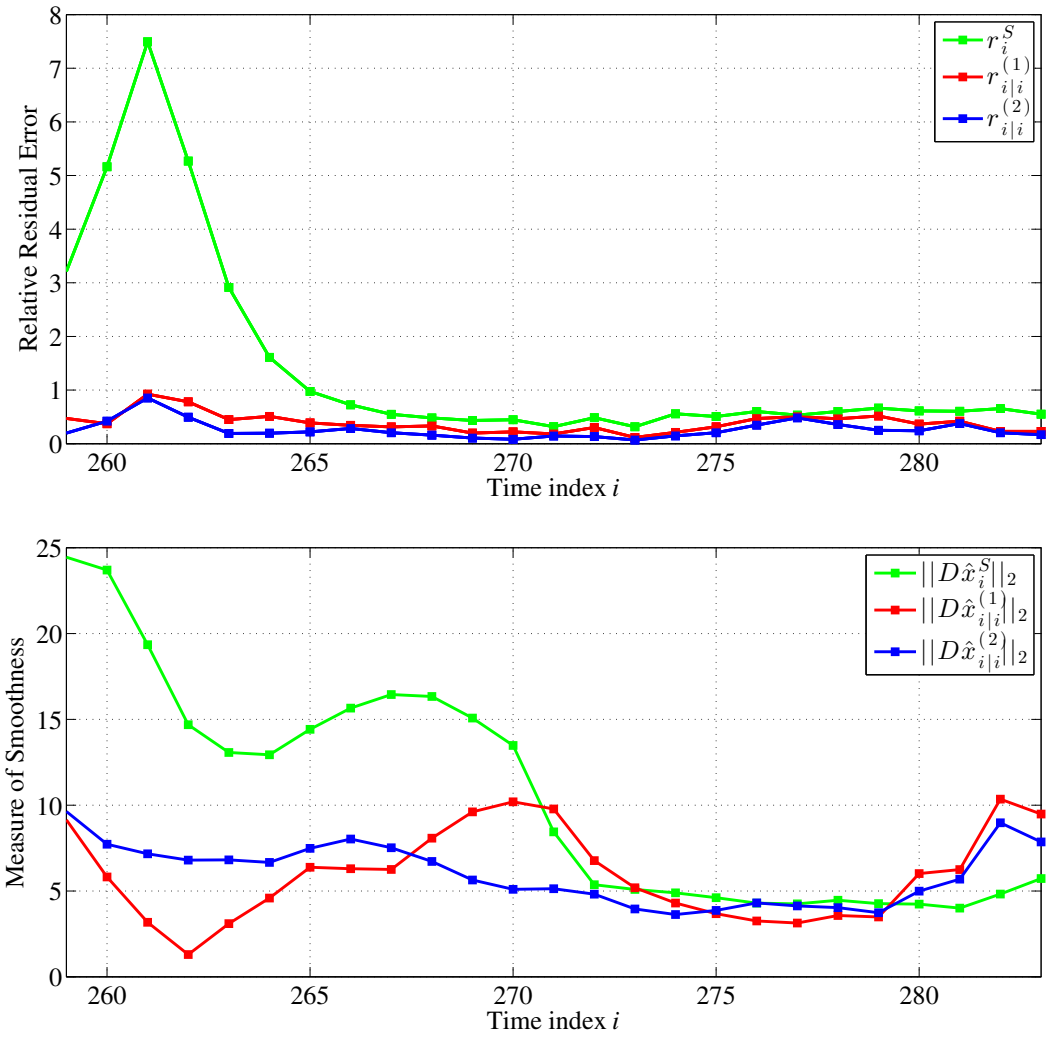

Figure 5.27: The comparison of the relative residual error (top) and the measure of smoothness (bottom) between the estimates $\hat{\boldsymbol{x}}_i^S$, $\hat{\boldsymbol{x}}_{i|i}^{(1)}$ and $\hat{\boldsymbol{x}}_{i|i}^{(2)}$ during which the rectangular wooden plate moves away from the whisker array located at 44.7 cm toward the hose exit between the states $\boldsymbol{x}_{259}$ and $\boldsymbol{x}_{283}$.

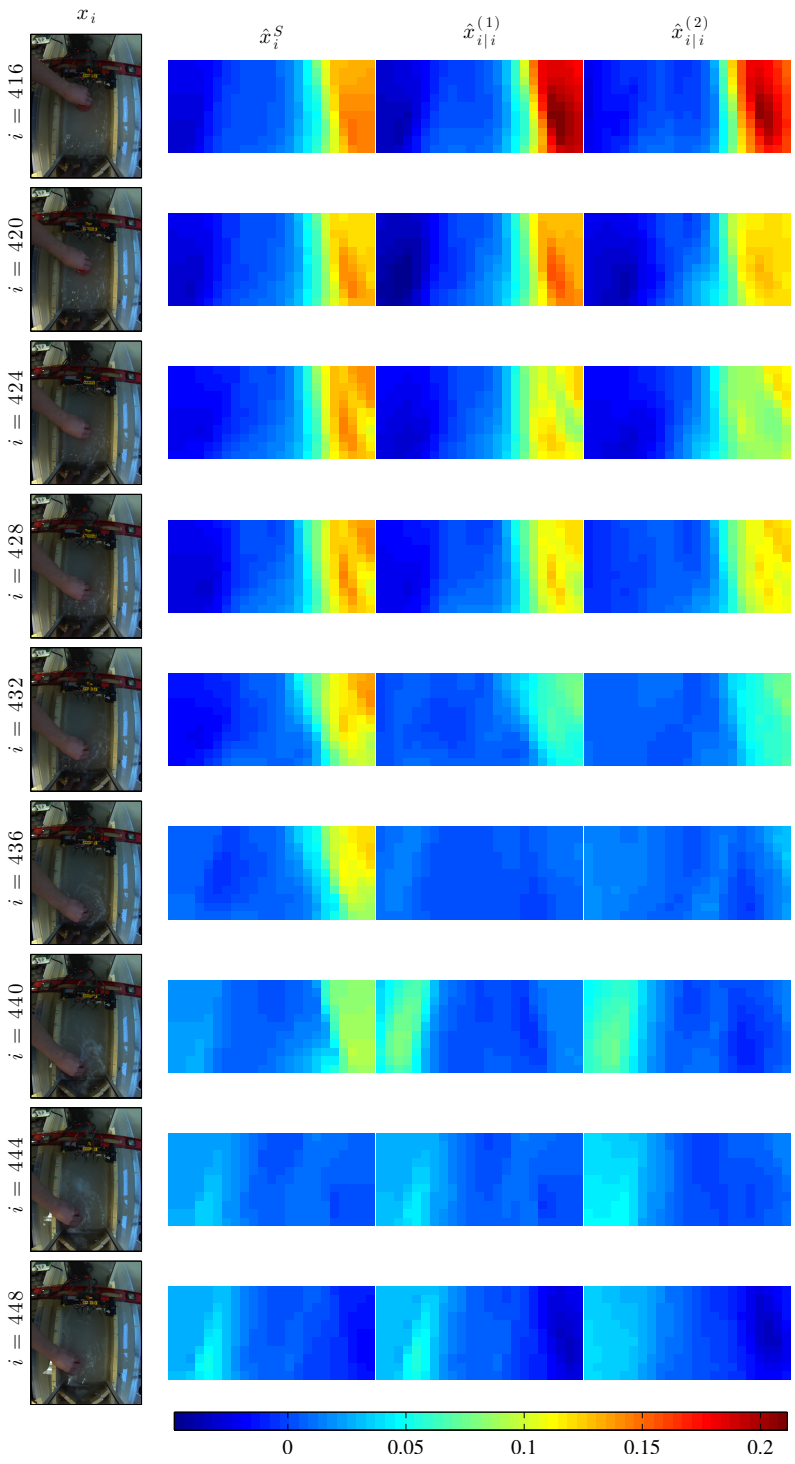

Figure 5.28: The dynamic tactile tomographic imaging results for the estimates $\hat{\boldsymbol{x}}_i^S$, $\hat{\boldsymbol{x}}_{i|i}^{(1)}$ and $\hat{\boldsymbol{x}}_{i|i}^{(2)}$ during which the plastic cup moves away from the whisker array positioned at 44.7 cm toward the hose exit between the states $\boldsymbol{x}_{416}$ and $\boldsymbol{x}_{448}$.

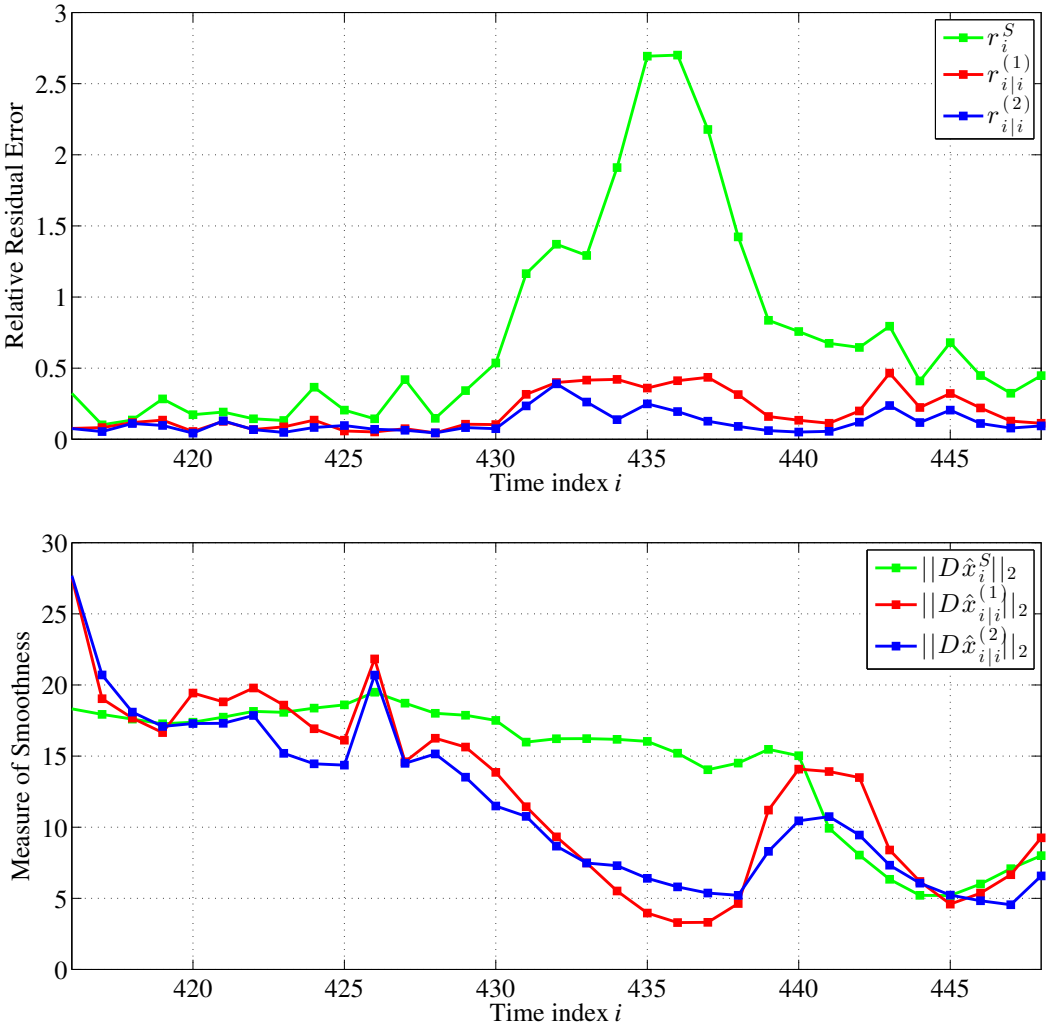

Figure 5.29: The comparison of the relative residual error (top) and the measure of smoothness (bottom) between the estimates $\hat{\boldsymbol{x}}_i^S$, $\hat{\boldsymbol{x}}_{i|i}^{(1)}$ and $\hat{\boldsymbol{x}}_{i|i}^{(2)}$ during which the plastic cup moves away from the whisker array positioned at 44.7 cm toward the hose exit between the states $\boldsymbol{x}_{416}$ and $\boldsymbol{x}_{448}$.

The second case is the tracking of a plastic cup moving in a similar fashion to the first case as it leaves its original position in front of the whisker array positioned at 44.7 cm away from the hose exit and gets closer to the screen before the hose exit over time. The static and dynamic tactile tomographic imaging results are presented in Figure 5.28 along with the resulting relative residual error and measure of smoothness shown in Figure 5.29 between the

states $\boldsymbol{x}_{416}$ and $\boldsymbol{x}_{448}$.

In this case, as the plastic cup moves away from the whisker array, it begins to weaken the positive flow near the right wooden wall sensed by the whisker array because of getting closer to the hose exit, similar to the case in air flow imaging experiments. After the complete blocking of the flow by the plastic cup around the state $\boldsymbol{x}_{436}$ as seen in the dynamic estimates and the peak in the static relative residual error, the flow travels around the plastic cup and changes direction toward the left wall as seen in the states $\boldsymbol{x}_{440}$ through $\boldsymbol{x}_{448}$, which is also partially blocked as the plastic cup gets really close to the screen before the hose exit. This flow pattern can also be observed in the dynamic smoothness level as a small oscillatory behavior after the state $\boldsymbol{x}_{436}$ until the dynamic smoothness level slowly decreases as expected.

CHAPTER 6

Conclusions

This dissertation has developed a new advanced array signal processing solution for the imaging of surroundings with robotic whiskers, by adapting the well-established tomographic imaging technique to the tactile perception mechanism widely used by vibrissal sensing animals. The experimental results demonstrate that the tomographic imaging concept can be successfully applied to extract 2-D nearby object features including shape, size and location, and map out the cross-sectional fluid-flow velocity-squared distribution, indicating that this is a very feasible model for bio-inspired systems using arrays of vibrissal sensors for the reconstruction of surroundings.

The random walk dynamic model used for the tactile flow tomography may not be sufficient when the time period between the two successive frames during the sequential estimation becomes relatively large. Therefore, ongoing research efforts include using methods such as the optical flow [66, 67] in order to learn the state-evolution matrix through the frame-by-frame estimation of the motion model. In addition, the vector projection method used to enforce smoothness with reduced computational complexity can be replaced by more advanced physical constraints using a linear equality constrained state estimation model to achieve better-quality dynamic reconstructions [68–72].

In this dissertation, the state dimension was relatively small for the dynamic fluid-flow tomography. However, the computational cost of the Kalman

filter significantly increases with the state dimension, since the state error covariance matrix grows considerably larger in size with the state dimension. Several techniques exist to reduce the computational cost of the classical KF for high-dimension state estimation, including the ensemble Kalman filter (EnKF) [32, 73], and dimension-reduction methods [70, 74]. Integrating some of these solutions into the dynamic fluid-flow tomography can increase the computational efficiency of our model, and hence will enable high-resolution flow imaging with robotic whiskers.

Future studies also include the development of a fully integrated 3-D tactile tomographic imaging technique that is capable of simultaneous object recognition and fluid-flow imaging. The experimental results suggest that the future 3-D extension of our model in space may serve as a new bio-inspired tactile sensing technology for many robotic applications including object feature extraction, navigation, object tracking, obstacle avoidance, simultaneous localization and environmental mapping.

REFERENCES

[1] M. Brecht, B. Preilowski, and M. Merzenich, "Functional architecture of the mystacial vibrissae," *Behav Brain Res*, vol. 84, pp. 81–97, 1997.

[2] M. L. Andermann, J. Ritt, M. A. Neimark, and C. I. Moore, "Neural correlates of vibrissa resonance: Band-pass and somatotopic representation of high-frequency stimuli," *Neuron*, vol. 42, pp. 451–463, 2004.

[3] G. Dehnhardt, B. Mauck, and H. Bleckmann, "Seal whiskers detect water movements," *Nature*, vol. 394, pp. 235–236, July 16 1998.

[4] F. Anjum, H. Turni, P. G. H. Mulder, J. V. D. Burg, and M. Brecht, "Tactile guidance of prey capture in etruscan shrews," in *Proc. Nat. Acad. Sci. USA*, vol. 103, Oct. 31 2006, pp. 16 544–16 549.

[5] T. J. Prescott, M. J. Pearson, B. Mitchinson, J. C. W. Sullivan, and A. G. Pipe, "Whisking with robots: From rat vibrissae to biomimetic technology for active touch," *IEEE Robotics and Automation Magazine*, vol. 16, no. 3, pp. 42–50, 2009.

[6] T. Tsujimura and T. Yabuta, "A tactile sensing method for employing force/torque information through insensitive probes," in *Robotics and Automation, 1992. Proceedings, 1992 IEEE International Conference on*, 1992, pp. 1315–1320 vol. 2.

[7] M. Kaneko, N. Kanayama, and T. Tsuji, "Active antenna for contact sensing," *Robotics and Automation, IEEE Transactions on*, vol. 14, no. 2, pp. 278–291, 1998.

[8] N. Ueno, M. Svinin, and M. Kaneko, "Dynamic contact sensing by flexible beam," *Mechatronics, IEEE/ASME Transactions on*, vol. 3, no. 4, pp. 254–264, 1998.

[9] D. Kim and R. Möller, "Biomimetic whiskers for shape recognition," *Robot. Auton. Syst.*, vol. 55, no. 3, pp. 229–243, Mar. 2007.

[10] T. N. Clements and C. D. Rahn, "Three-dimensional contact imaging with an actuated whisker," *IEEE Transactions on Robotics*, vol. 22, no. 4, pp. 844–848, 2006.

[11] M. Lungarella, V. V. Hafner, R. Pfeifer, and H. Yokoi, "Artificial whisker sensors in robotics," in *Proceedings of the IEEE/RSJ International Conference on Intelligent Robots and Systems*, 2002, pp. 2931–2936.

[12] M. Fend, S. Bovet, H. Yokoi, and R. Pfeifer, "An active artificial whisker array for texture discrimination," in *Proceedings of the 2003 IEEE/RSJ Intl. Conference on Intelligent Robots and Systems*, Las Vegas, Nevada, October 2003, pp. 1044–1049.

[13] R. A. Russell and J. A. Wijaya, "Object location and recognition using whisker sensors," in *Australasian Conference on Robotics and Automation*, 2003, pp. 761–768.

[14] G. Scholz and C. Rahn, "Profile sensing with an actuated whisker," *Robotics and Automation, IEEE Transactions on*, vol. 20, no. 1, pp. 124–127, 2004.

[15] J. H. Solomon and M. J. Z. Hartmann, "Artificial whiskers suitable for array implementation: Accounting for lateral slip and surface friction," *IEEE Transactions on Robotics*, vol. 24, no. 5, pp. 1157–1167, October 2008.

[16] J. H. Solomon and M. J. Z. Hartmann, "Extracting object contours with the sweep of a robotic whisker using torque information," *The International Journal of Robotics Research*, vol. 29, no. 9, pp. 1233–1245, August 2010.

[17] J. H. Solomon and M. Hartmann, "Biomechanics: Robotic whiskers used to sense features," *Nature*, vol. 443, no. 7111, p. 525, 2006.

[18] M. J. Pearson, A. G. Pipe, C. Melhuish, B. Mitchinson, and T. J. Prescott, "Whiskerbot: A robotic active touch system modeled on the rat whisker sensory system," *Adaptive Behavior*, vol. 15, no. 3, pp. 223–240, 2007.

[19] M. J. Pearson, B. Mitchinson, J. Welsby, T. Pipe, and T. J. Prescott, "Scratchbot: Active tactile sensing in a whiskered mobile robot," *Lecture Notes in Computer Science (including subseries Lecture Notes in Artificial Intelligence and Lecture Notes in Bioinformatics)*, vol. 6226 LNAI, pp. 93–103, 2010.

[20] C. W. Fox, M. H. Evans, N. F. Lepora, M. Pearson, A. Ham, and T. J. Prescott, "Crunchbot: A mobile whiskered robot platform," *Lecture Notes in Computer Science (including subseries Lecture Notes in Artificial Intelligence and Lecture Notes in Bioinformatics)*, vol. 6856 LNAI, pp. 102–113, 2011.

[21] B. Mitchinson, J. Sullivan, M. Pearson, A. Pipe, and T. Prescott, "Perception of simple stimuli using sparse data from a tactile whisker array," in *Biomimetic and Biohybrid Systems*, ser. Lecture Notes in Computer Science, N. Lepora, A. Mura, H. Krapp, P. Verschure, and T. Prescott, Eds. Springer Berlin Heidelberg, 2013, vol. 8064, pp. 179–190.

[22] J. A. Birdwell, J. H. Solomon, M. Thajchayapong, M. A. Taylor, M. Cheely, R. B. Towal, J. Conradt, and M. J. Z. Hartmann, "Biomechanical models for radial distance determination by the rat vibrissal system," *Journal of Neurophysiology*, vol. 98, no. 4, pp. 2439–2455, 2007.

[23] C. Tuna, J. H. Solomon, D. L. Jones, and M. J. Z. Hartmann, "Object shape recognition with artificial whiskers using tomographic reconstruction," in *ICASSP, IEEE International Conference on Acoustics, Speech and Signal Processing - Proceedings*, 2012, pp. 2537–2540.

[24] D. J. Tritton, *Physical Fluid Dynamics*, 2nd ed. New York: Oxford University Press, 1988.

[25] J. Roy R. Craig, *Mechanics of Materials*, 2nd ed. New York: Wiley, 2000.

[26] Y.-C. Ho and R. Lee, "A Bayesian approach to problems in stochastic estimation and control," *Automatic Control, IEEE Transactions on*, vol. 9, no. 4, pp. 333–339, 1964.

[27] M. Arulampalam, S. Maskell, N. Gordon, and T. Clapp, "A tutorial on particle filters for online nonlinear/non-Gaussian Bayesian tracking," *Signal Processing, IEEE Transactions on*, vol. 50, no. 2, pp. 174–188, 2002.

[28] R. E. Kalman, "A new approach to linear filtering and prediction problems," *Transactions of the ASME Journal of Basic Engineering*, vol. 82, no. 1, pp. 35–45, 1960.

[29] B. D. O. Anderson and J. B. Moore, *Optimal Filtering*. Englewood Cliffs, NJ: Prentice-Hall, 2005.

[30] M. Butala, F. Kamalabadi, R. Frazin, and Y. Chen, "Dynamic tomographic imaging of the solar corona," *Selected Topics in Signal Processing, IEEE Journal of*, vol. 2, no. 5, pp. 755–766, 2008.

[31] M. D. Butala, "A state-space approach to dynamic tomography," Ph.D. dissertation, University of Illinois at Urbana-Champaign, Urbana, IL, 2010.

[32] M. Butala, R. Frazin, Y. Chen, and F. Kamalabadi, "Tomographic imaging of dynamic objects with the ensemble Kalman filter," *Image Processing, IEEE Transactions on*, vol. 18, no. 7, pp. 1573–1587, July 2009.

[33] A. George, M. Butala, R. Frazin, F. Kamalabadi, and Y. Bresler, "Time-resolved cardiac CT reconstruction using the ensemble Kalman filter," in *Biomedical Imaging: From Nano to Macro, 2008. ISBI 2008. 5th IEEE International Symposium on*, 2008, pp. 1489–1492.

[34] M. Vauhkonen, P. Karjalainen, and J. Kaipio, "A Kalman filter approach to track fast impedance changes in electrical impedance tomography," *Biomedical Engineering, IEEE Transactions on*, vol. 45, no. 4, pp. 486–493, 1998.

[35] A. Seppänen, M. Vauhkonen, P. J. Vauhkonen, E. Somersalo, and J. P. Kaipio, "State estimation with fluid dynamical evolution models in process tomography – An application to impedance tomography," *Inverse Problems*, vol. 17, no. 3, p. 467, 2001.

[36] V. Kolehmainen, S. Prince, S. R. Arridge, and J. P. Kaipio, "State-estimation approach to the nonstationary optical tomography problem," *J. Opt. Soc. Am. A*, vol. 20, no. 5, pp. 876–889, May 2003.

[37] F. Natterer, *The Mathematics of Computerized Tomography*. New York, NY: John Wiley and Sons, 1986.

[38] G. Ólafsson and E. T. Quinto (Eds.), *The Radon Transform, Inverse Problems, and Tomography – Proceedings of Symposia in Applied Mathematics, Volume 63*. Providence, RI: AMS, 2006.

[39] R. E. Blahut, *Theory of Remote Image Formation*. Cambridge, UK: Cambridge University Press, 2004.

[40] J. Hsieh, *Computed Tomography: Principles, Design, Artifacts, and Recent Advances*. Bellingham, WA: SPIE-The International Society for Optical Engineering, 2003.

[41] B. C. Levy, *Principles of Signal Detection and Parameter Estimation*. New York, NY: Springer, 2008.

[42] A. M. Bruckstein, D. L. Dohono, and M. Elad, "From sparse solutions of systems of equations to sparse modeling of signals and images," *SIAM Review*, vol. 51, no. 1, 34-81 2009.

[43] E. J. Candès, J. Romberg, and T. Tao, "Robust uncertainty principles: Exact signal reconstruction from highly incomplete robust uncertainty principles: Exact signal frequency information," *IEEE Transactions on Information Theory*, vol. 52, no. 2, pp. 489–509, 2006.

[44] E. J. Candès, J. K. Romberg, and T. Tao, "Stable signal recovery from incomplete and inaccurate measurements," *Communications on Pure and Applied Mathematics*, vol. 59, no. 8, pp. 1207–1223, 2006.

[45] H. Liao and G. Sapiro, "Sparse representations for limited data tomography," in *Biomedical Imaging: From Nano to Macro, 2008. ISBI 2008. 5th IEEE International Symposium on*, May 2008, pp. 1375–1378.

[46] L. I. Rudin, S. Osher, and E. Fatemi, "Nonlinear total variation based noise removal algorithms," *Physica D: Nonlinear Phenomena*, vol. 60, no. 1-4, pp. 259–268, 1992.

[47] A. Delaney and Y. Bresler, "A fast and accurate fourier algorithm for iterative parallel-beam tomography," *Image Processing, IEEE Transactions on*, vol. 5, no. 5, pp. 740–753, May 1996.

[48] E. J. Candès and J. Romberg. (2005, Oct.). L1-magic. [Online]. Available: http://users.ece.gatech.edu/~justin/l1magic/

[49] Y. Shi, W. Karl, and D. Castanon, "Dynamic tomography using curve evolution with spatial-temporal regularization," in *Image Processing. 2002. Proceedings. 2002 International Conference on*, vol. 2, 2002, pp. II–629–II–632 vol. 2.

[50] Y. Shi, W. Clem Karl, and D. Castanon, "Dynamic object-based tomographic reconstruction," in *Signals, Systems and Computers, 2002. Conference Record of the Thirty-Sixth Asilomar Conference on*, vol. 1, Nov. 2002, pp. 906–910 vol. 1.

[51] P. K. Kundu and I. M. Cohen, *Fluid Mechanics*, 3rd ed. London, UK: Elsevier, 2004.

[52] C. W. Groetsch, *Inverse Problems in the Mathematical Sciences*. Braunschweig/Wiesbaden, Germany: Vieweg, 1993.

[53] F. Kamalabadi, "Multidimensional image reconstruction in astronomy," *IEEE Signal Processing Magazine*, vol. 27, no. 1, pp. 86–96, 2010.

[54] J. E. Peterson, B. N. P. Paulsson, and T. V. McEvilly, "Applications of algebraic reconstruction techniques to crosshole seismic data (USA, Sweden)." *Geophysics*, vol. 50, no. 10, pp. 1566–1580, 1985.

[55] N. Rawlinson, S. Pozgay, and S. Fishwick, "Seismic tomography: A window into deep earth," *Physics of the Earth and Planetary Interiors*, vol. 178, no. 3-4, pp. 101–135, 2010.

[56] S. M. Kay, *Fundamentals of Statistical Signal Processing: Estimation Theory*. Upper Saddle River, NJ: Prentice-Hall, 1993.

[57] W. C. Karl, "Regularization in image restoration and reconstruction," in *Handbook of Image and Video Processing*, A. Bovik, Ed. San Diego: Academic, 2000, pp. 141–160.

[58] A. Tikhonov, "Solution of incorrectly formulated problems and the regularization method," in *Soviet Math. Doklady*, vol. 4, 1963, pp. 1035–1038.

[59] D. M. Strong and T. F. Chan, "Edge-preserving and scale-dependent properties of total variation regularization," in *Inverse Problems*, 2000, pp. 165–187.

[60] U. Amato and W. Hughes, "Maximum entropy regularization of Fredholm integral equations of the first kind," *Inverse Problems*, vol. 7, pp. 793–808, Dec. 1991.

[61] T. Kailath, A. H. Sayed, and B. Hassibi, *Linear Estimation*. Upper Saddle River, NJ: Prentice Hall, 2000.

[62] G. H. Golub, M. Heath, and G. Wahba, "Generalized cross-validation as a method for choosing a ridge parameter," *Technometrics*, vol. 21, pp. 215–223, 1979.

[63] A. Bovik, *Handbook of Image and Video Processing*, 2nd ed. Burlington, MA: Academic, 2005.

[64] J. Fessler and W. Rogers, "Spatial resolution properties of penalized-likelihood image reconstruction: Space-invariant tomographs," *Image Processing, IEEE Transactions on*, vol. 5, no. 9, pp. 1346–1358, 1996.

[65] Y. Zhang, A. Ghodrati, and D. H. Brooks, "An analytical comparison of three spatio-temporal regularization methods for dynamic linear inverse problems in a common statistical framework," *Inverse Problems*, vol. 21, no. 1, p. 357, 2005.

[66] J. Barron, D. Fleet, and S. Beauchemin, "Performance of optical flow techniques," *International Journal of Computer Vision*, vol. 12, no. 1, pp. 43–77, 1994.

[67] T. Gautama and M. Van Hulle, "A phase-based approach to the estimation of the optical flow field using spatial filtering," *Neural Networks, IEEE Transactions on*, vol. 13, no. 5, pp. 1127–1136, 2002.

[68] W. Wen and H. Durrant-Whyte, "Model-based multi-sensor data fusion," in *Robotics and Automation, 1992. Proceedings, 1992 IEEE International Conference on*, 1992, pp. 1720–1726 vol. 2.

[69] H. E. Doran, "Constraining Kalman filter and smoothing estimates to satisfy time-varying restrictions," *The Review of Economics and Statistics*, vol. 74, no. 3, pp. pp. 568–572, 1992.

[70] R. Hewett, M. Heath, M. Butala, and F. Kamalabadi, "A robust null space method for linear equality constrained state estimation," *Signal Processing, IEEE Transactions on*, vol. 58, no. 8, pp. 3961–3971, 2010.

[71] D. Simon and T. L. Chia, "Kalman filtering with state equality constraints," *Aerospace and Electronic Systems, IEEE Transactions on*, vol. 38, no. 1, pp. 128–136, 2002.

[72] N. Gupta, "Kalman filtering in the presence of state space equality constraints," in *Control Conference, 2007. CCC 2007. Chinese*, 2007, pp. 107–113.

[73] G. Burgers, P. Jan van Leeuwen, and G. Evensen, "Analysis scheme in the ensemble Kalman filter," *Monthly Weather Review*, vol. 126, no. 6, pp. 1719–1724, 1998.

[74] R. Baraniuk, V. Cevher, and M. Wakin, "Low-dimensional models for dimensionality reduction and signal recovery: A geometric perspective," *Proceedings of the IEEE*, vol. 98, no. 6, pp. 959–971, 2010.